INNOVATIVE APPROACHES IN THE DEVELOPMENT OF ELECTROCHEMICAL BIOSENSORS FOR VIRUS AND VIROID DETECTION

Alnilan Cristina Barros Lobato

Doctoral Dissertation
Jožef Stefan International Postgraduate School
Ljubljana, Slovenia

Supervisor: Dr. Nikola Tasić, Department of Analytical Chemistry, National Institute of Chemistry, Ljubljana, Slovenia

Evaluation Board:
Prof. Dr. Marina Dermastia, Chair, Jožef Stefan International Postgraduate School and National Institute of Biology, Ljubljana, Slovenia
Prof. Dr. Mitja Kolar, Member, Faculty of Chemistry and Chemical Technology, University of Ljubljana, Ljubljana, Slovenia
Dr. Milan Žunić, Member, Institute for Multidisciplinary Research, University of Belgrade, Belgrade, Serbia

MEDNARODNA PODIPLOMSKA ŠOLA JOŽEFA STEFANA
JOŽEF STEFAN INTERNATIONAL POSTGRADUATE SCHOOL



Alnilan Cristina Barros Lobato

INNOVATIVE APPROACHES IN THE DEVELOPMENT OF ELECTROCHEMICAL BIOSENSORS FOR VIRUS AND VIROID DETECTION

Doctoral Dissertation

INOVATIVNI PRISTOPI PRI RAZVOJU ELEKTROKEMIJSKIH BIOSENZORJEV ZA DETEKCIJO VIRUSOV IN VIROIDOV

Doktorska disertacija

Supervisor: Dr. Nikola Tasić

Ljubljana, Slovenia, June 2025

"Let the past hold on to itself and let the present move forward into the future."
– Douglas Adams

Acknowledgments

This PhD was my personal journey, but I am only human; as such, I need community, support, and care from others, and there are many people I would like to acknowledge.

First and foremost, I want to thank my parents, Benedito and Isabel, and my brother, Állan; without their unlimited support, care, and love, I wouldn't have become the person I am today. I love you three immensely.

I also want to acknowledge the rest of my family, particularly Bianca and Justina, who have always believed in me.

I want to thank the friends I made in Slovenia: Antea, Ivan, Layrton, Victor, Katja, Meryem, Martin, Katy, Jelena, and Mitja. You are all essential to my well-being. I can't picture my life here without you, and wherever I go next, I'll keep you in my heart.

I want to acknowledge the friends I've made throughout different stages of my life and that I always think fondly of, despite the distance: Camila, Lou, Danton, Luís, Gabi, Amanda S., Patricia, Larissa R., Lívia, Kath, Em, Peggy-Sue, Trycia, Carlos, Anderson, Luyssa, Marcos, Rafael, Rui, Amanda D., Luciana, Natasha, Fabio, Kelly, Larissa A., Henrique, and Jaque. All of you have supported me in countless ways and at different times, helping me appreciate life amidst the chaos.

I want to thank my mentor, Dr. Nikola Tasić, for always being there for me and for all the guidance, teachings, and support you gave me. Since the day we met many years ago, I have learned so much from you, and I'll always be thankful for your influence in my life.

I want to thank Dr. Samo B. Hočevar for welcoming me to the Department of Analytical Chemistry of the National Institute of Chemistry. Special thanks to Dr. Tea Romih for the opportunity to work here and the support I received in my first few months. I am grateful to all my colleagues' kind assistance and collaboration, especially Nina. Furthermore, I want to acknowledge all our work partners from the Biotechnical Faculty of the University of Ljubljana, the Slovenian Institute of Hop Research and Brewing, and the Institute of Biophysics of the Czech Academy of Sciences.

I want to thank the Jožef Stefan International Postgraduate School community for their support throughout my journey. From the very first day, the dean, professors, secretaries, and fellow students welcomed me with open arms. I'm truly grateful and hope to continue participating in this fantastic community.

Additionally, I want to thank the members of the committee: Dr. Marina Dermastia, Dr. Mitja Kolar, and Dr. Milan Žunić. Thank you for taking the time and effort to evaluate and improve my work.

Finally, my Ph.D. work was financially supported by the Slovenian Research Agency (research Program P1-0034 and Research Project J1-3017) and the Slovenian Research Agency's Young Researchers Programme (grant agreement no. 56119).

I'll always be grateful to have crossed paths with everyone mentioned above. As Douglas Adams wrote in the book Mostly Harmless, "We live in strange times. We also live in strange places: each in a universe of our own. The people with whom we populate our universes are the shadows of whole other universes intersecting with our own."

Thank you for being part of my universe.

Abstract

Viruses and viroids are a major threat to both animals and plants. While viruses contain a nucleic acid genome (DNA or RNA) enclosed in a protein coat, viroids consist of a small, circular RNA without a protein coat. In particular, viroids only infect plants and their destructive nature can lead to severe agroeconomic losses. In contrast, viruses infect animals, plants and bacteria and are primarily responsible for global pandemics and associated human fatalities.

Viruses and viroids are usually detected using conventional molecular biology techniques. Although these methods are reliable, they require sophisticated laboratory infrastructure. Alternatively, electrochemical biosensors, such as immunosensors targeting antigens, and genosensors targeting nucleic acids, offer the potential for rapid, sensitive, and selective on-site detection. In this doctoral dissertation, innovative strategies for the development and optimization of sensitive and selective electrochemical immunosensors for the detection of the SARS-CoV-2 spike protein and the electrochemical genosensor for the detection of the *Citrus bark cracking viroid* (CBCVd) are presented. These devices are based on the affinity approach and measure the specific interactions between the biological recognition element immobilized on the supporting electrode and the target antigen or nucleic acid in the investigated samples using electrochemical impedance spectroscopy.

The first immunosensor presented in this dissertation is based on gelatin-modified disposable electrodes for the preferentially oriented immobilization of anti-SARS-CoV-2 antibodies, which act as biological recognition elements. The second immunosensor relies on the signal amplification through abundant antibody binding via MXene surface groups and carefully chosen chemistry leading to refined electrochemical communication between antibody-containing upper sensing layer and the underlying supporting electrode. The sensor showed excellent selectivity against structurally similar coronaviruses.

Finally, the choice of the CBCVd as an analyte was governed by the immense public demand due to the large economic losses caused by this viroid in Slovenia, Germany and the Czech Republic. A $Ti_3C_2T_x$ MXene-streptavidin-agarose composite was used for stable immobilization of a biotinylated single-stranded DNA capture probe as a biological recognition element. The impedimetric genosensor showed potential for early diagnosis of plant disease, due to its excellent analytical performance in total RNA samples extracted from infected and non-infected hop plants.

The presented approaches highlight the importance of functional (nano)materials in biosensors, proper immobilization of biological recognition elements and fast and unambiguous electrochemical signaling. The results are very promising and show significant potential for translation into robust point-of-care diagnostic tools for human and plant pathogens outside of the laboratory.

Povzetek

Virusi in viroidi so velika grožnja tako živalim kot rastlinam. Medtem ko virusi vsebujejo genom nukleinske kisline (DNK ali RNK), obdan v beljakovinsko ovojnico, so viroidi sestavljeni iz majhne, krožne RNK brez beljakovinske ovojnice. Viroidi okužijo samo rastline in njihova uničujoča narava lahko povzroči hude agroekonomske izgube. Nasprotno pa virusi okužijo živali, rastline in bakterije ter so v prvi vrsti odgovorni za svetovne pandemije in z njimi povezane človeške smrti.

Viruse in viroide običajno zaznavamo s konvencionalnimi tehnikami molekularne biologije. Čeprav so te metode zanesljive, zahtevajo sofisticirano laboratorijsko infrastrukturo. Druga možnost je, da elektrokemijski biosenzorji, kot so imunosenzorji za tarčno zaznavanje antigenov in genosenzorji za tarčno zaznavanje nukleinskih kislin, ponujajo potencial za hitro, občutljivo in selektivno odkrivanje na kraju potrebe. V tej doktorski disertaciji so predstavljene inovativne strategije za razvoj in optimizacijo občutljivih in selektivnih elektrokemijskih imunosenzorjev za detekcijo bodičastega proteina SARS-CoV-2 in elektrokemijskega genosenzorja za detekcijo viroida razpokanosti skorje agrumov (CBCVd). Te naprave temeljijo na afinitetnem pristopu in merijo specifične interakcije med biološkim prepoznavnim elementom, imobiliziranim na podporni elektrodi, in ciljnim antigenom ali nukleinsko kislino v preiskovanih vzorcih z uporabo elektrokemijske impedančne spektroskopije.

Prvi imunosenzor, predstavljen v tej disertaciji, temelji na z želatino modificiranih elektrodah za enkratno uporabo s pravilno usmerjeno imobilizacijo protiteles proti SARS-CoV-2, ki delujejo kot biološko prepoznavni elementi. Drugi imunosenzor temelji na ojačanju signala z vezavo protiteles na površinske skupine MXena in skrbno izbrano kemijo, ki vodi do rafinirane elektrokemijske komunikacije med zgornjo zaznavno plastjo s protitelesi in spodnjo podporno elektrodo. Senzor je pokazal izjemno selektivnost za analit v prisotnosti strukturno podobnih koronavirusov.

Nazadnje je k izbiri CBCVd kot analita vplivalo ogromno javno povpraševanje zaradi velikih gospodarskih izgub, ki jih je ta viroid povzročil v Sloveniji, Nemčiji in na Češkem. Kompozit $Ti_3C_2T_x$ MXene-streptavidin-agaroza je bil uporabljen za stabilno imobilizacijo biotinilirane sonde za zajemanje enoverižne DNK kot biološko-prepoznavnega elementa. Impedimetrični genosenzor je pokazal potencial za zgodnjo diagnozo rastlinskih bolezni zaradi svoje odlične analitske učinkovitosti v vzorcih celokupne RNK, ekstrahirane iz okuženih in neokuženih rastlin hmelja.

Predstavljeni pristopi poudarjajo pomen funkcionalnih (nano)materialov v biosenzorjih, pravilne imobilizacije elementov biološkega prepoznavanja ter hitrega in nedvoumnega elektrokemijskega signaliziranja. Rezultati so zelo obetavni in kažejo velik potencial za pretvorbo v robustna diagnostična orodja na kraju potrebe za človeške in rastlinske patogene zunaj laboratorija.

Contents

List of Figures **xv**

Abbreviations **xvii**

1 Introduction **1**
1.1 Relevance of Pathogenic Viruses and Viroids 1
1.2 Electroanalytical Methods 2
1.2.1 Electrochemical techniques for biosensing 3
1.2.2 Supporting electrodes and electrolytes 7
1.3 Electrochemical Biosensors 8
1.3.1 Types of biosensors 9
1.3.1.1 Electrochemical immunosensors 9
1.3.1.2 Electrochemical genosensors 11
1.3.2 Electrochemical biosensor design and development 13
1.3.2.1 Surface modification 13
1.3.2.2 Immobilization of the biological recognition element 15
1.3.2.3 Electrochemical detection and biosensor validation 17

2 Goals and hypotheses **19**

3 Scientific Publications **21**
3.1 Manuscript 1: "Development of a simple gelatin-based sensing platform for the sensitive label-free impedimetric detection of SARS-CoV-2" 22
3.2 Manuscript 2: "Study of V_2CT_x-MXene Based Immunosensor for Sensitive Label-Free Impedimetric Detection of SARS-CoV-2 Spike Protein" 30
3.3 Manuscript 3: "Label-free and sensitive detection of *Citrus Bark Cracking Viroid* in hop using $Ti_3C_2T_x$ MXene-modified genosensor" 43

4 Conclusions **53**
4.1 Principal Advancements and Scientific Contributions 53
4.2 Experimental Insights and Hypothesis Validation 53
4.3 Study Limitations and Technical Challenges 56
4.4 Opportunities for Development and Innovation 57
4.5 Final Remarks 58

Appendix A Supporting Information **59**

References **83**

Bibliography **93**

Biography **97**

List of Figures

Figure 1.1: Schematic representation of (A) an electrochemical cell setup and (B) the corresponding electrical circuit diagram. 2
Figure 1.2: Impedance spectra in the form of (A) Nyquist plot and (B) Bode plot. 3
Figure 1.3: (A) Impedance spectra showing a simplified Randles equivalent circuit for an electrochemical system. (B) Examples of Nyquist plot curves and their equivalent circuits. Adapted from Magar, Hassan, and Mulchandani 2021 [22]. 4
Figure 1.4: Schematic diagrams of the most common electrochemical techniques used in biosensing, including (A) chronoamperometry, (B) chronopotentiometry, (C) linear sweep voltammetry, (D) cyclic voltammetry, (E) square-wave voltammetry, (F) differential pulse voltammetry. Based on the images from the PSTrace 5.9 software manual [23]. 5
Figure 1.5: Schematic of an electrochemical biosensor, including choice of the supporting electrode (solid conventional or disposable electrodes), sensor architecture with possible biorecognition elements, and generated electrochemical signals through CV, pulse voltammetric technique, chronoamperometry, or EIS (from top to bottom) 8
Figure 1.6: (A) Structure of a monoclonal IgG antibody, highlighting the two heavy chains and two light chains, with the antigen-binding fragments (Fab) and the crystallizable fragment (Fc) clearly labeled, (B) schematic representation of the SARS-CoV-2 virus, illustrating the spike proteins (antigens), envelope, membrane proteins, and RNA genome. 9
Figure 1.7: Schematic representation of (A) label-free, (B) sandwich, and (C) competitive electrochemical immunosensors. 10
Figure 1.8: A sandwich-type electrochemical genosensor 12
Figure 1.9: A label-free electrochemical genosensor. 12
Figure 1.10: State-of-the-art nanomaterials used in electrochemical biosensing for signal enhancement purposes: (A) carbon nanotubes, (B) graphene, and (C) $M_4X_3T_x$, M_3X_2Tx, M_2XTx MXenes (from top to bottom), adapted from Hong et al [84]. 14

Abbreviations

2D	... Two-dimensional
3D	... Three-dimensional
ANF	... Artificial nasopharyngeal fluid
BSA	... Bovine serum albumin
CBCVd	... *Citrus bark cracking viroid*
CCCVd	... *Coconut cadang-cadang viroid*
CE	... Counter electrode
CNTs	... Carbon nanotubes
COVID-19	... Coronavirus disease 2019
CV	... Cyclic voltammetry
DNA	... Deoxyribonucleic acid
EDC	... 1-ethyl-3-(3-dimethylaminopropyl) carbodiimide
EIS	... Electrochemical impedance spectroscopy
ELISA	... Enzyme-linked immunosorbent assay
FTO	... Fluorine-doped tin oxide
ITO	... Indium tin oxide
MWCNTs	... Multi-walled carbon nanotubes
NHS	... N-hydroxysuccinimide
PBS	... Phosphate-buffered saline
PCR	... Polymerase chain reaction
PEC	... Photoelectrochemical
RE	... Reference electrode
RNA	... Ribonucleic acid
SARS-CoV-2	... Severe acute respiratory syndrome coronavirus 2
ssDNA	... Single-stranded DNA
SELEX	... Systematic evolution of ligands by exponential enrichment
SPCE	... Screen-printed carbon electrode
SPE	... Screen-printed electrode
SWCNTs	... Single-walled carbon nanotubes
SWV	... Square-wave voltammetry
WE	... Working electrode

Chapter 1

Introduction

1.1 Relevance of Pathogenic Viruses and Viroids

Viruses are small infectious agents consisting of a nucleic acid genome (i.e. DNA or RNA) enveloped in a protein capsid [1]. They are obligate intracellular parasites, meaning they can only replicate inside a host cell. Viruses can infect a wide range of hosts and rely heavily on the host's cellular machinery to reproduce and propagate [2]. In recent years, the coronavirus pandemic has brought global attention to the dangers of viral infections, which have caused millions of deaths worldwide [3]. The emergence of potentially transmissible and vaccine-resistant strains of severe acute respiratory syndrome coronavirus 2 (SARS-CoV-2) continues complicating efforts to develop effective prevention and treatment strategies [4]. Unfortunately, this is not the first pandemic caused by a virus and is unlikely to be the last. Therefore, there is a need to detect viruses and viral infections quickly and efficiently.

Viroids, though publicly less known, pose a high threat to agriculture. They are small, non-encapsulated circular RNA pathogens that can infect various plant crops [5]. Unlike viruses, viroids don't have a protein shell and don't carry any genes for making proteins. Still, they're able to replicate inside plant cells, using mechanisms scientists are still working on to fully understand [6]. Viroids can remain unnoticed in their original host but cause severe damage in new hosts, leading to increased transmission, low crop yields, and significant economic losses [7]. One such viroid is the *Citrus bark cracking viroid* (CBCVd), which was first found in citrus in 1988 and classified as a mild pathogen for these plants [8]. However, in 2007, it was discovered in hop (*Humulus lupulus L.*), an important crop for the beer and pharmaceutical industries, and was classified as an aggressive pathogen, resulting in the complete eradication of over 300 ha of fields [9]. Because symptoms can take years to appear, and no cure exists, the only current solution is to destroy infected plants, making CBCVd a serious threat to hop growers around the world [10].

The emergence of such pathogens underlines the need to detect them quickly and accurately. Such pathogens can be detected using gold-standard methods such as polymerase chain reaction (PCR) and enzyme-linked immunosorbent assay (ELISA) [11]. Although these methods have great analytical competence, they are laborious, expensive, and time-consuming [12]. For this reason, simpler and more time-efficient methods for the detection of viruses have been and are still being developed, with electrochemical biosensors playing a special role in this scenario [13].

1.2 Electroanalytical Methods

Electrochemistry is the branch of chemistry concerned with the interaction of electrical and chemical effects [14]. Key applications of electrochemistry include corrosion studies, batteries, fuel cells, electroplating, electrophoresis, corrosion, sensors, etc. Importantly, electrochemistry is a valuable tool in analytical chemistry, as it enables the measurement of electrical properties such as current, potential or charge, which are generated in response to the relevant chemical reactions related to the investigated analyte. Electrochemical measurements occur at the electrode-solution interface and are classified based on the type of electrical signal used. The two main types are **potentiometric**, which measures the electrode potential without drawing current, and **potentiostatic**, which controls the electrode potential while measuring the resulting current.

Both methods require at least two electrodes: the working electrode (WE), which responds to the analyte, and the reference electrode (RE), which maintains a stable potential. For potentiostatic techniques, a three-electrode cell configuration is more commonly used (Figure 1.1), consisting of a WE, a RE, and a counter (or auxiliary) electrode (CE). In this setup, current flows between the WE and CE, while the potential is measured against the RE [14], [15]. Additionally, electrochemical cells can be classified as electrolytic, where electricity is consumed, or galvanic, where electrical energy is generated [16].

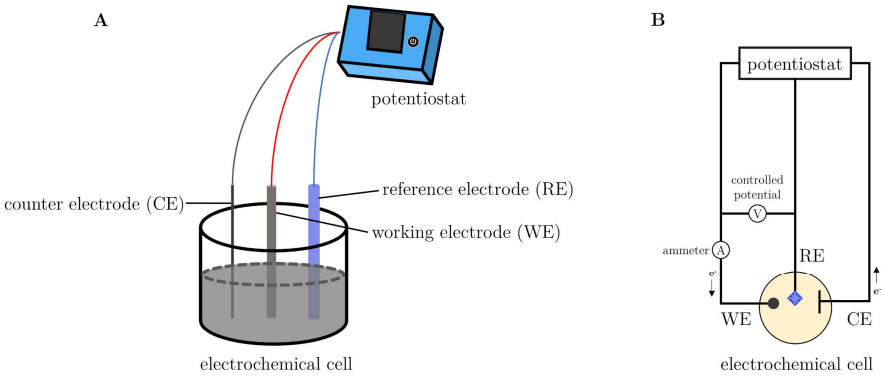


Figure 1.1: Schematic representation of (A) an electrochemical cell setup and (B) the corresponding electrical circuit diagram.

Potentiometric methods operate under static conditions with no current flow, determining a sample's composition by measuring the potential developed across a membrane. In contrast, potentiostatic (controlled-potential) techniques focus on charge-transfer processes at the electrode-solution interface. The latter involves dynamic conditions, where the electrode potential drives an electron-transfer reaction, and the resulting current is measured. These techniques can detect any electroactive species, which are capable of oxidation or reduction. Electrochemically inactive compounds can be detected with the assistance of a redox probe or through a derivatization reaction [14], [16].

Two types of processes occur at the electrode surface: faradaic and non-faradaic. **Faradaic processes** involve reactions where charge is transferred across the electrode-solution interface, related to oxidation or reduction, and these reactions follow Faraday's law (i.e., the amount of chemical reaction caused by current flow is proportional to the amount of electricity passed). **Non-faradaic processes** are electrochemical phenomena

that do not involve electron transfer or redox reactions at the electrode surface. Instead, they refer to the rearrangement of charges and ions at the electrode–electrolyte interface. In contrast to Faradaic processes, non-faradaic reactions are reversible and do not alter the chemical composition of the analyte. They are especially valuable in label-free sensing, sensitive detection without the consumption of the target species[14].

1.2.1 Electrochemical techniques for biosensing

Electrochemical impedance spectroscopy (EIS) is a powerful and versatile technique used to investigate the behavior of various electrochemical systems. It works by applying a small-amplitude of alternating current (AC) voltage (or current) across a wide range of frequencies to a system at equilibrium or in a steady state. The resulting current (or voltage) response is then recorded. When the system behaves in a linear and time-invariant manner, the relationship between the input and output signals can be described using a transfer function. This function represents the system's impedance across different frequencies and reveals important information about the underlying physical and chemical processes happening in the system [17].

Impedance (Z) itself is a complex quantity that combines both resistance and reactance. It reflects how much the system opposes the flow of electric current. In the context of electrochemical biosensors, changes in impedance are often caused by interactions occurring at the surface of the WE, such as the binding of biomolecules or changes in charge transfer kinetics. These interactions alter properties like capacitance and electron transfer resistance [18].EIS can be performed in two modes: faradaic and non-faradaic, depending on whether redox reactions occur at the electrode surface [19]. In faradaic EIS, impedance changes result from electron transfer reactions involving redox-active species. In non-faradaic EIS, no redox reactions occur; instead, impedance changes arise from alterations in the electrical double-layer, such as those caused by biomolecule adsorption at the electrode interface [20].EIS data is typically represented using either Nyquist or Bode plots. A typical Nyquist plot encountered in faradaic electrochemical biosensing (Figure 1.2A) shows the imaginary part of impedance (Z'') plotted against the real part (Z'), with each point corresponding to a specific frequency. The shape of the plot is interpreted using an equivalent electrical circuit model, such as the Randles circuit (Figure 1.3A), to identify and quantify the contributions of different ongoing physicochemical processes [21].

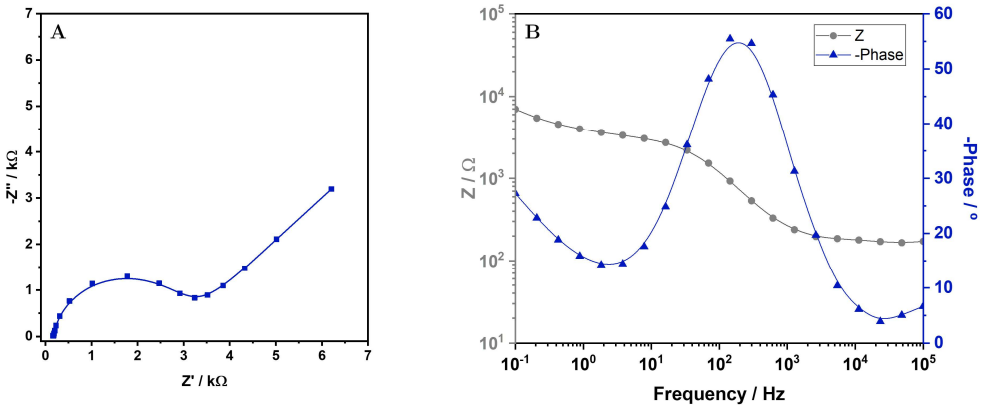


Figure 1.2: Impedance spectra in the form of (A) Nyquist plot and (B) Bode plot.

Bode plots (Figure 1.2B), on the other hand, display the magnitude of the impedance and the phase angle as functions of frequency; Bode plots are especially useful when

interpreting frequency-dependent responses [22]. Main contribution in the depicted spectra comes from the charge transfer resistance (R_{ct}), characterized by the semicircle in the Nyquist plot, and a phase peak in the Bode plot. The semicircle originates at the charge transfer resistance value, corresponding to the solution resistance (R_s). Furthermore, at lower frequencies, the diffusion of molecules (e.g., redox-active species) can limit the current flow. This introduces a component known as Warburg impedance (Z_w), which increases as the frequency decreases. In a Nyquist plot, diffusion is typically characterized by a 45° line extending from the charge transfer semicircle, indicating ion diffusion limitations at low frequencies.

A major strength of EIS lies in its ability to simultaneously record and differentiate between several interfacial and bulk processes in a single measurement. As mentioned, these processes can be modeled using an equivalent electrical circuit, consisting of wide selection of specific circuit elements, including resistors, capacitors, constant phase elements (CPE), diffusion-related elements, etc. [17]. Because ideal capacitive behavior is rarely observed due to surface roughness or non-homogeneity, a constant phase element *CPE* is often used to more accurately model the double-layer behavior [21], [22].

The shape and features of the impedimetric spectra guide the selection and fitting of the equivalent circuit model (Figure 1.3A). Since the impedance response depends heavily on the working electrode material, surface modification, and electrolyte composition, different sensor designs may produce distinctly shaped plots (Figure 1.3B).

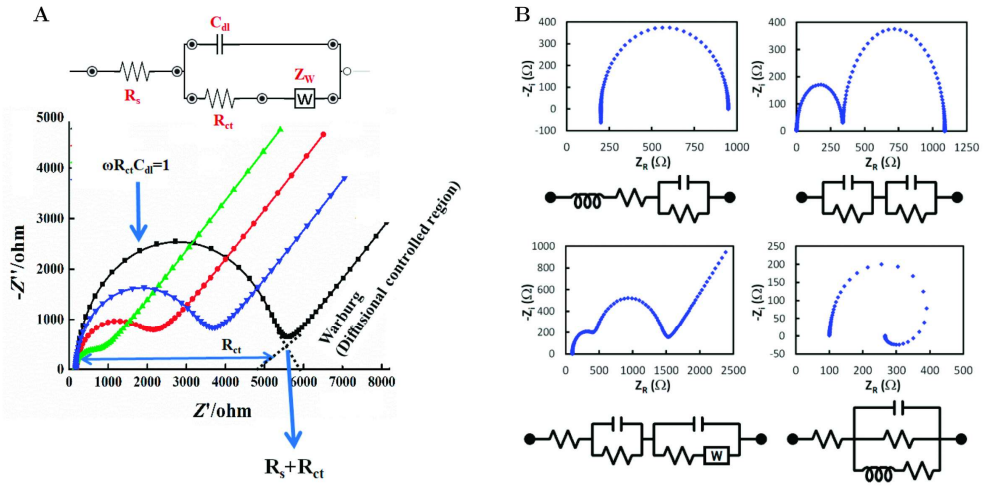


Figure 1.3: (A) Impedance spectra showing a simplified Randles equivalent circuit for an electrochemical system. (B) Examples of Nyquist plot curves and their equivalent circuits. Adapted from Magar, Hassan, and Mulchandani 2021 [22].

Due to its sensitivity, non-destructive nature, and ability to operate without labels or secondary reagents, EIS is widely employed in the development of electrochemical biosensors. A label refers to a molecule or material attached to the target analyte to facilitate its detection. Labels can enhance the sensitivity and specificity of the sensor by producing a measurable signal when the target analyte is present. Common labels include fluorescent dyes, enzymes, nanoparticles, and electroactive compounds. Therefore, EIS enables direct, real-time monitoring of biomolecular recognition events (e.g. antigen-antibody interactions or nucleic acid hybridization) which makes it particularly valuable for sensitive and specific analysis [22].

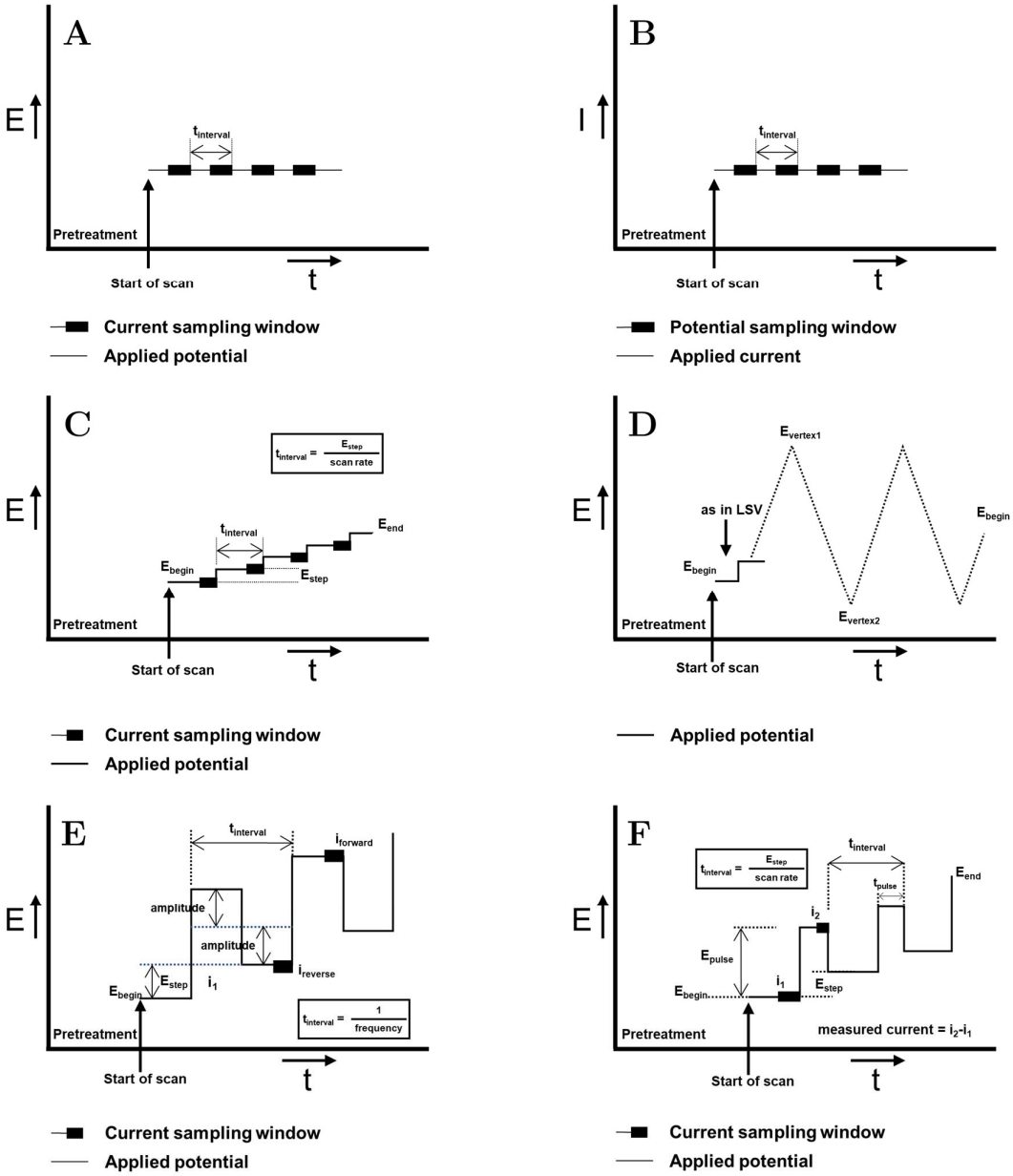


Figure 1.4: Schematic diagrams of the most common electrochemical techniques used in biosensing, including (A) chronoamperometry, (B) chronopotentiometry, (C) linear sweep voltammetry, (D) cyclic voltammetry, (E) square-wave voltammetry, (F) differential pulse voltammetry. Based on the images from the PSTrace 5.9 software manual [23].

Potentiometry is based on the measurement of a potential difference that develops at the WE interface due to the accumulation of ions. This potential is established between the WE and the RE and varies according to the ion concentration in solution, following the Nernst equation [24]. As previously stated, potentiometric methods operate under near-zero current conditions, ensuring that the measured potential reflects the equilibrium state of the system [19]. Potentiometric biosensors primarily utilize membrane-based WEs

composed of selectively permeable ion-conducting materials, which facilitate the selective recognition of specific ions or biomolecules. The most common types of potentiometric electrodes include ion-selective electrodes (ISEs), which are designed to detect specific ions in solution, and ion-sensitive field-effect transistors (ISFETs), which integrate semiconductor technology for enhanced miniaturization and signal processing. These sensors are widely used in biomedical, environmental, and industrial applications due to their high selectivity, stability, and low power consumption [19]. **Chronopotentiometry** works by measuring the potential as a function of time in response to a constant or square-wave current [25], and represents the most common potentiometry-based electroanalytical technique.

Conductometry measures the electrical conductivity of a solution between two parallel electrodes, where conductivity is determined by the total concentration of dissolved ions in the analyte solution. In a conductometric biosensor, the interaction between the biological recognition element and the target analyte leads to changes in the ionic composition of the solution, altering its conductivity or current flow. This change results from the production or consumption of charged species during the biochemical reaction [26]. However, conductometric techniques require a significant alteration in the total ionic strength of the solution to ensure reliable measurements. If the change in ion concentration is too small relative to the background electrolyte, variations in ionic strength may introduce interference and measurement inconsistencies. As a result, conductometry generally has lower sensitivity compared to other electrochemical techniques, such as amperometry and potentiometry, which can offer more selective and precise detection [26].

Amperometry is a technique that measures the steady-state current generated by the oxidation or reduction of a species at a fixed potential between the WE and the RE. As the excitation potential starts the electron transfer function, the current is a direct measure of the electron transfer rate, therefore it is directly proportional to the analyte concentration [27]. In **chronoamperometry**, the current is recorded as a function of time after a square-wave potential is applied to the WE. Alterations in the current arise from the expansion or reduction of the diffusion layer at the electrode [25].

Voltammetry is a controlled-potential technique that encompasses various methods for electrochemical analysis. In voltammetric techniques, a time-dependent potential is applied to an electrochemical cell between the WE and the RE, and the resulting current is measured between the WE and the CE [15]. The potential is scanned within a defined window, and the corresponding current response, generated by electron transfer events between an electroactive species and the WE, is recorded. These electron transfer events produce a current signal, often characterized by a peak value proportional to the concentration of the analyte. Several voltammetric techniques have been developed with the intention of improving the selectivity and sensitivity of the measurements. Cyclic voltammetry (CV), differential pulse voltammetry (DPV) and square-wave voltammetry (SWV) are amongst the most commonly used.

Cyclic voltammetry (CV) is one of the most widely used electrochemical techniques, providing valuable insight into the oxidation and reduction processes of molecular species. It is also essential for studying electron transfer-initiated chemical reactions, such as catalysis [25], [28]. In CV, the potential is swept between two set values (V_1 and V_2) at a fixed rate. Once the potential reaches V_2, the scan reverses, sweeping back to V_1. The scan rate ($v = V_2 - V_1/t_2 - t_1$) is a crucial parameter, as it controls how fast the applied potential is scanned and that can affect the diffusion layer and the observed current peak [28]. The resulting data is plotted as current vs. voltage, generating a voltammogram that reveals key electrochemical properties of the system.

Differential pulse voltammetry (DPV) involves applying short pulses superimposed on a linearly increasing potential to the working electrode. The current is

sampled twice: before the pulse is applied and at the end of each pulse, and the difference between these values is calculated. The resulting current differences are plotted against the applied potential, generating a voltammogram with current peaks whose magnitude is directly proportional to the concentration of the analyte. DPV is widely used for trace analysis due to its enhanced sensitivity and resolution compared to conventional voltammetric techniques [16].

Square-wave voltammetry (SWV) is a high-amplitude differential technique and a specialized form of DPV. In SWV, a symmetrical square-wave signal is superimposed on a staircase potential and applied to the working electrode. The current is measured twice per cycle: once at the end of the forward pulse and once at the end of the reverse pulse; and the difference between these measurements is plotted against the base staircase potential. This technique is one of the fastest and most sensitive pulse voltammetry methods, making it highly effective for trace analysis and electrochemical biosensing [16].

1.2.2 Supporting electrodes and electrolytes

Two main classes of the supporting electrodes are mostly used in electrochemical biosensing, i.e., **disposable** and **solid conventional electrodes**. Disposable electrodes are designed for on-site, real-time analysis on portable potentiostats, while solid conventional electrodes are typically used in laboratory settings, offering higher precision for the systematic analytical, as well as fundamental electrochemical studies.

Gold electrodes are commonly considered as benchmark for sensing applications, due to the existence of thiol-Au-based chemical protocols which facilitate immobilization of the biological recognition elements on the electrode surface in addition to the excellent conductive properties and biocompatibility of gold itself [29], [30].

Carbon-based electrodes have been intensively investigated and utilized in biosensing due to their versatility and operational range, as well as high conductivity. The most exploited carbon electrodes in electrochemical biosensing are the glassy carbon electrode (GCE), graphite electrodes, and carbon paste electrodes [31], [32]. In recent years, many other types of electrodes emerged, including paper-based electrodes, aluminium-based electrodes, fluorine-doped tin oxide (FTO) or indium tin oxide (ITO) glass electrodes,3D-printed nanocarbon electrodes, pencil graphite electrodes, magneto-actuated graphite-epoxy composite electrodes, etc. [33], [34], [35], [36].

Screen-printed electrodes (SPEs) are miniaturized devices consisting of a chemically inert ceramic (alumina) or plastic substrate on which three electrodes (WE, RE and CE) are screen-printed from pastes containing particular functional materials. The electrochemical reactions take place at the WE, while RE and CE close the circuit, as in conventional electrochemical cell. The WE of an SPE usually consists of carbon-based materials (screen-printed carbon electrode, SPCE), gold (screen-printed gold electrode, SPAuE), silver, platinum, copper, bismuth-based materials, nickel-based structures, or conducting polymer-based layers [37].

The choice of electrolyte in electrochemical biosensing depends on biocompatibility, electrochemical performance and compatibility with the utilized redox probes, if the sensor operates in the faradaic mode. Electrolytes such as phosphate-buffered saline (PBS), potassium chloride (KCl), sodium chloride (NaCl), acetate buffers, Tris-HCl buffers, or ionic liquids, are commonly used because they are biocompatible and provide a stable ionic environment for antibody-antigen or DNA hybridization reactions, as well as the appropriate ionic strength for the subsequent electrochemical measurements.

In the faradaic operating mode, the electrolyte is usually accompanied by the redox probe, such as methylene blue [38], hexacyanoferrate(II)/(III) [39], hexaammineruthenium(II)/(III) [40], ferrocene and its derivates, hydroquinone or

benzoquinone, etc. Finally, a new class of SPEs with the integrated redox system have emerged, combining the advantages of SPEs, such as low cost and ease of functionalization, with the enhanced sensitivity provided by the embedded redox-active species, such as hexacyanoferrate(II)/(III), or ferrocene [41].

1.3 Electrochemical Biosensors

Electrochemical biosensors are devices comprising the biological recognition element immobilized on the supporting electrode that specifically reacts with the target (Figure 1.5) [42]. The detection mechanism of electrochemical biosensors originates either through biocatalytic interaction or affinity interaction. Catalytic biosensors use biomolecules to generate electroactive species, while the affinity sensors are based on the selective binding interaction between the biological recognition element and the target analyte [42], [43].

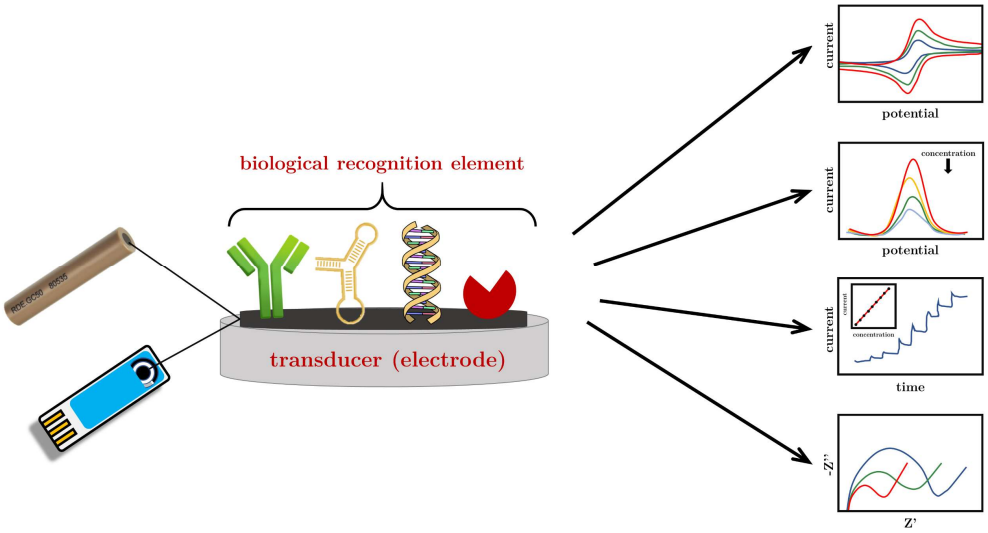


Figure 1.5: Schematic of an electrochemical biosensor, including choice of the supporting electrode (solid conventional or disposable electrodes), sensor architecture with possible biorecognition elements, and generated electrochemical signals through CV, pulse voltammetric technique, chronoamperometry, or EIS (from top to bottom).

The biological recognition elements in electrochemical biosensors can include (i) enzymes, (ii) antibodies, (iii) antigens, (iv) nucleic acids, and (vi) aptamers. **Enzymes** are biological catalysts that accelerate biochemical reactions by interacting with a substrate and converting it into different molecule; most enzymes are proteins by nature, but there are also RNA enzymes, i.e., ribozymes [44]. **Antibodies**, larger Y-shaped proteins, interact with a foreign molecules (antigens) to help the immune system recognize and respond to them. **Antigens** are molecules recognizes as foreign by the body, often originating from pathogenic microbes [45]. **Nucleic acids** are the fundamental biopolymers essential to life; they are composed of nucleotides, monomers consisting of the combination of a 5-carbon sugar, a phosphate group and a nitrogenous base. There are two types of nucleic acids, deoxyribonucleic acid (DNA) and ribonucleic acid (RNA). They differ in the 5-carbon sugar in their nucleotides: the former has deoxyribose, while the latter has ribose. Additionally, while DNA is double-stranded, RNA is typically single-stranded [44]. The size of common probes for genosensing also generally varies between fifteen and one hundred base pairs

(for double-stranded DNA) or nucleotides (for single-stranded DNA and RNA). **Aptamers** are synthetic nucleotides produced using a laboratory process called SELEX (systematic evolution of ligands by exponential enrichment), in which they are selected by repeated rounds of binding, separation and amplification [46]. As a rule, they consist of several dozen to hundreds of nucleotides. Aptamers are very stable, easy to modify and inexpensive to synthesize. They can bind to certain targets with high affinity and specificity and are therefore suitable as probes for the construction of biosensors [47].

1.3.1 Types of biosensors

Biosensors can be categorized based on their transducer type, detection mechanism, target analyte, or biorecognition element. In this dissertation, they will be classified into two main types: immunosensors and genosensors.

1.3.1.1 Electrochemical immunosensors

Electrochemical immunosensors are a class of biosensors that utilize biomolecules produced by the natural immune response of animals, i.e., antibodies. Antibodies are large proteins that recognize foreign substances, known as antigens, which can be whole bacteria, viruses, or their fragments. They can be monoclonal, binding to a single site on the antigen, or polyclonal, binding to multiple sites. Both types are used in immunosensor development due to the highly specific interaction between an antibody (Figure 1.6A) and its corresponding antigen (Figure 1.6B) [48].

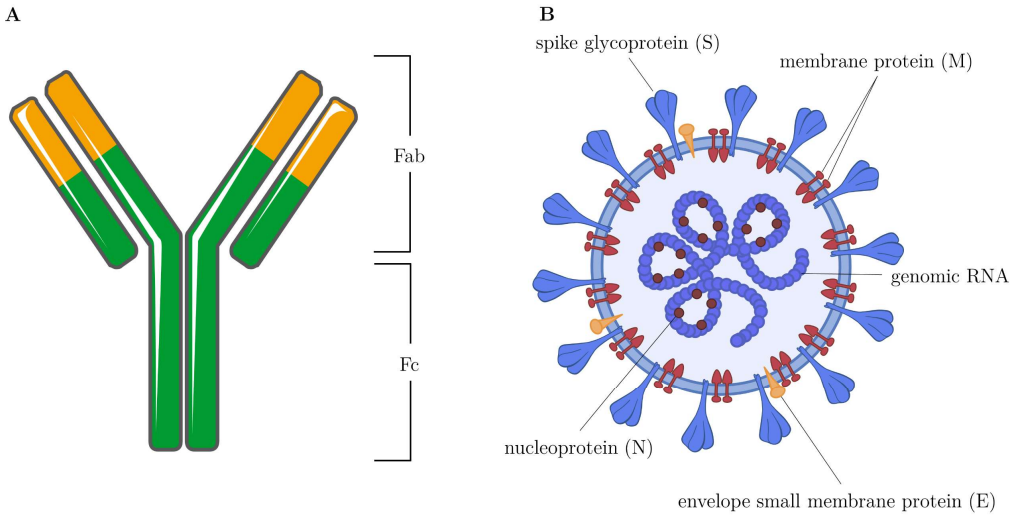


Figure 1.6: (A) Structure of a monoclonal IgG antibody, highlighting the two heavy chains and two light chains, with the antigen-binding fragments (Fab) and the crystallizable fragment (Fc) clearly labeled, (B) schematic representation of the SARS-CoV-2 virus, illustrating the spike proteins (antigens), envelope, membrane proteins, and RNA genome.

The working principle of electrochemical immunosensors involves converting the immunochemical reaction into a measurable electrical signal proportional to the analyte concentration. Depending on the sensor design, the biological recognition element can be either an antibody or an antigen [42].

Several electrochemical immunosensors have been developed for the detection of viral diseases such as Dengue [49], [50], Zika [51], [52], Hepatitis B [53] and C [54], and, more recently, SARS-CoV-2 [55], [56].

The immobilization method used in the development of an immunosensor should ensure the stability of the antibodies or antigens, maintaining their specificity and biological activity, through preferential alignment on the surface of the supporting electrode. Following the immobilization of the biological recognition element, it is important to prevent the non-specific binding through introduction of the "so-called" blocking agents, e.g., bovine serum albumin (BSA), glycine, and surfactants (e.g., Tween20, hexadecyltrimethylammonium bromide (CTAB) and sodium dodecyl sulphate (SDS), among others) [57]. These compounds will restrict the non-specific binding of target and interferent species that could reduce the sensitivity of the sensor, therefore allowing its usage in complex samples.

According to their immunoassay setup, the electrochemical immunosensors can be categorized as: label-free, sandwich-type, and competitive.

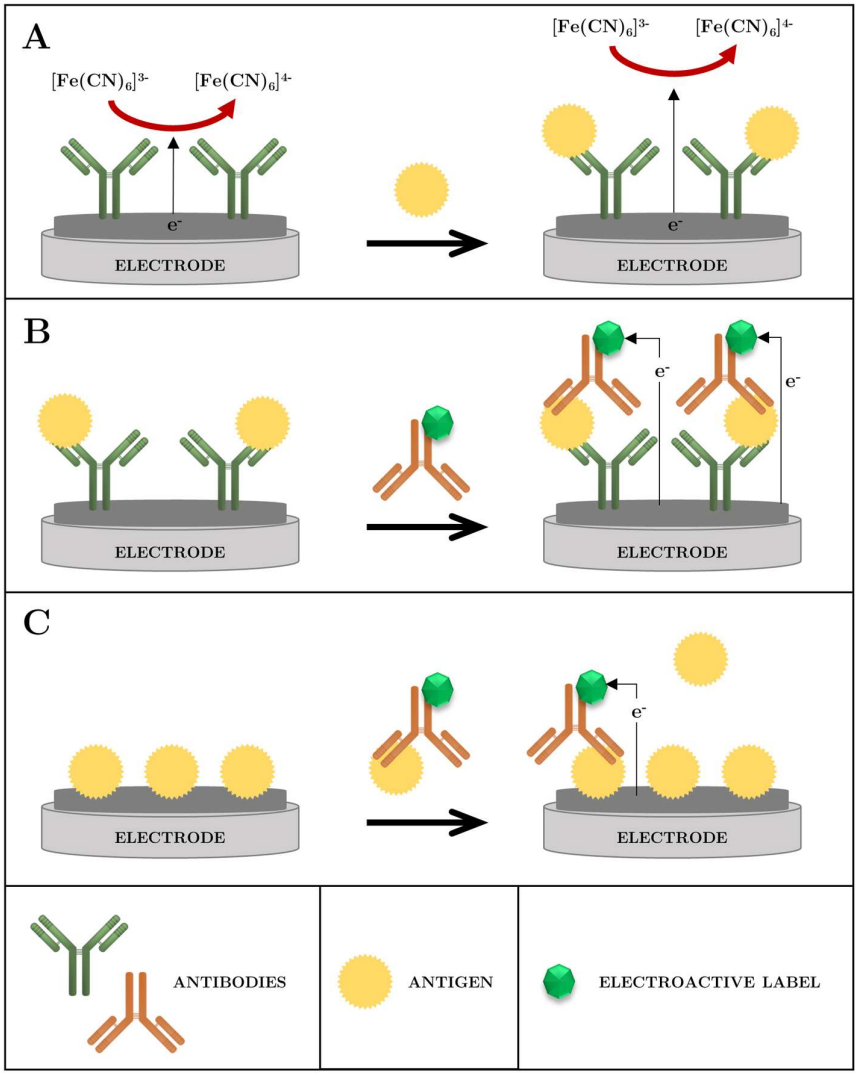


Figure 1.7: Schematic representation of (A) label-free, (B) sandwich, and (C) competitive electrochemical immunosensors.

Label-free electrochemical immunosensors (Figure 1.7A) take advantage of the electrochemical inactivity of most antibodies and antigens. By introducing a redox probe into the electrolyte solution, the immunochemical reaction will block the electron transfer between the electrode surface and the redox probe, changing the analytical signal. In voltammetric sensors, the peak current values decrease upon the addition of the analyte, while in impedimetric sensors, the charge transfer resistance increases [12].

In **sandwich-type electrochemical immunosensors** (Figure 1.7B), after the reaction between a primary antibody (biological recognition element) and an antigen (the analyte), a labelled secondary antibody is added. The measurable signal will be generated by the electroactive label in the secondary antibody and will be proportional to the amount of analyte in the sample. Several labels can be employed, such as electroactive compounds, enzymes and electrocatalysts. Sandwich-type sensors are generally more complex and expensive than label-free ones, but their analytical performance is better [12].

Competitive electrochemical immunosensors have labelled and free biomolecules compete for a limited number of binding sites immobilized on the surface of an electrode. As shown in Figure 1.7C, the immobilized antigen reacts preferentially with the labelled antibody in competition with the free antigens, with the analytical signal decreasing upon the increase in the concentration of the free antigen in the sample. The competitive approach is a good alternative for the detection of small molecules that do not produce relevant signal changes in label-free strategies or do not support sandwich assays [12].

1.3.1.2 Electrochemical genosensors

Electrochemical genosensors use immobilized nucleic acid capture probes as a biological recognition element, allowing for specific hybridization reactions to occur via DNA-DNA or DNA-RNA molecular recognition [58]. The efficiency of electrochemical genosensors has been reported for the detection of several viruses such as Ebola [59], [60], Dengue [61], Zika [62], Avian Influenza [63], [64], among others. Since viroids typically have a secondary structure that is difficult to deal with in electrochemical sensing, the development of electrochemical genosensors to detect them is still in early stages, and it has only been reported for *Coconut cadang-cadang viroid* (CCCVd) [65].

The construction of an electrochemical genosensor involves the modification of the electrode surface for the immobilization of the capture probe, and the following detection of the target through nucleic acid hybridization [66].

The nucleic acid hybridization is based on Watson and Crick's base pairing rules, wherein two complementary single strands of nucleic acids will form specific hydrogen bonds between their nucleobases; adenosine with thymine (DNA) or uracil (RNA), and guanine with cytosine [67]. The hybridization typically does not yield an electrochemical response by itself, so it is necessary to either label a "so-called" reporter probe that will generate a signal, use a redox probe or rely on the target's or probe's intrinsic electroactivity [68]. Therefore, akin to immunosensors, electrochemical genosensors can be divided into sandwich-type and label-free.

In **sandwich-type electrochemical genosensors**, the hybridization reaction can be detected by the addition of a reporter probe labeled with a redox signal amplifier that exhibits a specific electrochemical response. The redox signal amplifier can be an enzyme or a nanomaterial that produces redox-active molecules. After hybridization of the target with the capture probe, the reporter probe is added to bind with the reporter probe and the amount of target is indirectly quantified by the signal response of the reporter probe (Figure 1.8) [67].

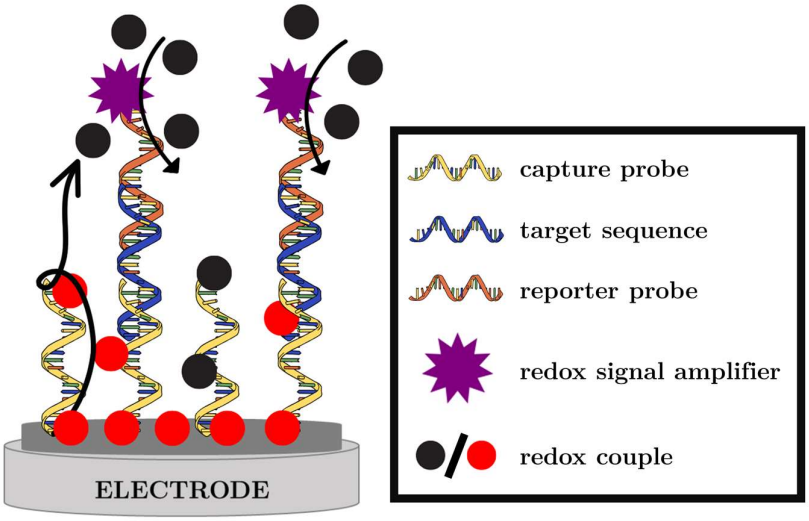


Figure 1.8: A sandwich-type electrochemical genosensor.

Label-free electrochemical genosensors can be fabricated in two ways. The first is similar to the label-free immunosensors, in which a redox probe is added to the electrolyte and its response will allow for the quantification of the target after hybridization (Figure 1.9) [12]. The second takes advantage of the intrinsic electrochemical activity of some nucleobases, which has been exploited in many applications to detect DNA damage, DNA hybridization, DNA-protein interactions, among others [68]; in this particular case, the non-hybridized probe will allow for good electron transfer and when the hybridization happens the electron transfer resistance will increase significantly, allowing for target quantification [12].

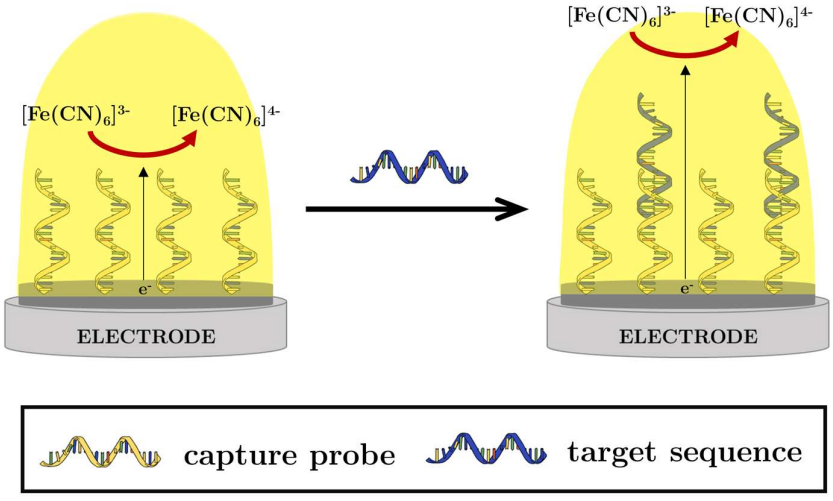


Figure 1.9: A label-free electrochemical genosensor.

Finally, the **electrochemical aptasensors**, which can be considered a subcategory of genosensors, utilize aptamers in place of a nucleic acids [69], and operate on the same principles as in the case of nucleic acid-based genosensors. Aptamers are short, single-

stranded DNA or RNA molecules that can fold into unique three-dimensional structures, allowing them to bind specifically and tightly to a wide range of target molecules, such as proteins, small molecules, or even cells. Aptamers are frequently referred to as artificial antibodies because they can mimic the binding ability of antibodies.

1.3.2 Electrochemical biosensor design and development

The design of an efficient electrochemical biosensor involves, in simple terms, three steps, which are **(i) the surface modification**, **(ii) the immobilization of the biorecognition element**, and **(iii) the electrochemical detection**.

The efficiency of a biosensor can be determined by its specificity and sensitivity, and both parameters need to be high enough to validate the sensor, by matching the clinically-relevant ranges for antibodies or antigens, or disease severity thresholds for plant pathogens [70]. Specificity is the ability of a sensor to unmistakably recognize the analyte in a complex sample, i.e., a sample containing other components that can interfere with the measurement [71]. The sensitivity of a sensor is defined as the minimum change in parameter input that will create a detectable output change [72].

1.3.2.1 Surface modification

The supporting electrode surface may need a modification (i) to facilitate the proper immobilization of the biorecognition element, (ii) to establish stable, reproducible electroanalytical signal, and (iii) to achieve high sensitivity of the operating biosensor.

While electrochemical biosensors can yield analytical results in the simplest setup in which the biorecognition element is just physically adsorbed or chemically bound onto the unmodified surface of the supporting electrode, the need for signal enhancement to reach lower detection limits and more reproducible signals remains. Signal stabilization and amplification can be obtained via addition of the functional (polymeric) membranes, and/or introduction of the (electro)catalytic (nano)materials, and/or via antibody amplification or nucleic acid polymerization reactions [73], [74].

Polymeric materials from natural or artificial sources are widely used as immobilization membranes in the development of biosensors. The membranes serve to immobilize the biorecognition element and/or to support the nanomaterials, which due to their high surface area and usually high electrical conductivity, provide good electrochemical communication between the outer sensing layers and the underlying supporting electrode. Polymers can be either electrochemically deposited on the active electrode surface or drop-casted. Drop-casting is an easy and straightforward process consisting of dropping a polymeric solution on the working electrode surface followed by the evaporation of the solvent, resulting in the formation of a polymeric layer [75]. A common natural polymer used for above described purposes is chitosan due to its good biocompatibility and high density of positive charge, which, for instance, attracts negatively-charged DNA [58], [76]. Another biopolymer that has shown potential in the past years is gelatin, which is also biocompatible and non-immunogenic; like chitosan, it allows for the stable immobilization of the biorecognition element as well as to sequester the signal enhancement nanomaterials [77], [78]. On the other hand, the electropolymerization is typically conducted by applying a constant potential (amperometry) or a potential sweep (CV) in the precursor monomer solution, resulting in the deposition of a polymer film on the working electrode surface [79], [80]. It can result in a highly uniform layer due to the possibility of controlling its thickness by adjusting the electrochemical parameters during the electrodeposition procedure [81].

Carbon-based materials are frequently used as signal enhancement materials in the development of electrochemical sensors, including the carbon black, carbon nanotubes (CNTs), carbon nanofibers, and two-dimensional (2D) materials such as graphene, (reduced) graphene oxide and MXenes [82], [83].

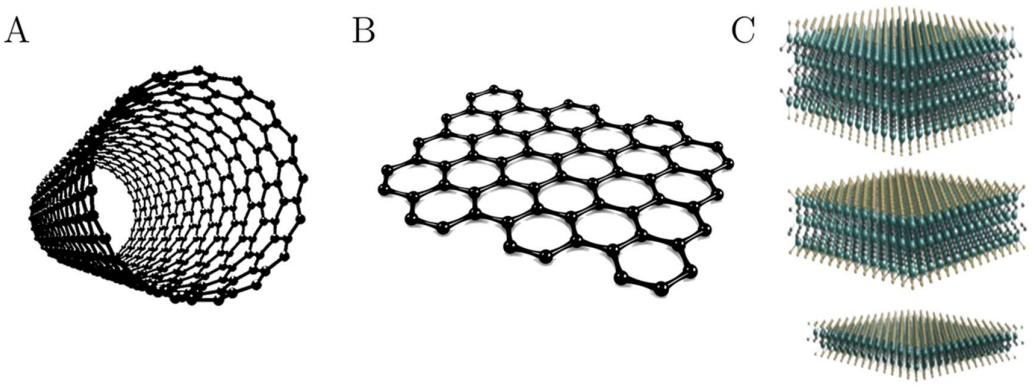


Figure 1.10: State-of-the-art nanomaterials used in electrochemical biosensing for signal enhancement purposes: (A) carbon nanotubes, (B) graphene, and (C) $M_4X_3T_x$, M_3X_2Tx, M_2XTx MXenes (from top to bottom), adapted from Hong et al [84].

CNTs (Figure 1.10A) are carbon nanostructures that consist of rolled-up graphene sheets that form cylindrical tubes with diameters in the nanometer range. A distinction is made between single-walled (SWCNTs), which consist of a single graphene layer, and multi-walled (MWCNTs), which consist of several concentric layers. offer exceptional electrical conductivity, mechanical strength, and thermal stability, making them ideal for nanoelectronics, energy storage, and sensing applications [85]. Their high surface to volume ratio leads to the outstanding adsorption of biomolecules and facilitate efficient electron transfer in electrochemical biosensors. The functionalization, either covalent or non-covalent, of CNTs enables the immobilization of enzymes, antibodies or nucleic acids, making them valuable for immunosensors, genosensors and enzymatic biosensors [86].

Graphene (Figure 1.10B) is a 2D nanomaterial composed of a single layer of sp^2-hybridized carbon atoms arranged in a honeycomb lattice. Since its isolation in 2004, it has gained significant attention due to its exceptional electrical, mechanical, and thermal properties, as well as its high surface area, flexibility, and chemical stability [87]. Functionalization of graphene, through oxidation (graphene oxide, GO) or reduction (reduced graphene oxide, rGO), allows for tunable surface chemistry, enhancing its biocompatibility, dispersibility, and interaction with biomolecules. These modifications expand its potential applications in electrochemical biosensors, where it serves as a highly conductive transducer for signal amplification [88].

MXenes (Figure 1.10C) are a promising class of 2D nanomaterials discovered in 2011, which have been rapidly explored due to their unique properties, including mechanical stability, hydrophilicity, biocompatibility, high electron transfer capability, large surface area, excellent electrocatalytic performance, and ease of surface functionalization and modification [89], [90]. Derived from three-dimensional (3D) MAX phases, MXenes have a general formula of $M_{n+1}X_nT_x$, where M represents an early transition metal (e.g., tantalum, tungsten, titanium, vanadium, chromium, zirconium, niobium, molybdenum, hafnium), X represents either carbon or nitrogen. One of the most commonly studied MXenes is $Ti_3C_2T_x$, where T_x denotes surface functional groups such as –O, –OH, and –F. The surface chemistry

of MXenes can vary depending on the abundance of these functional groups, influencing their properties and potential applications [91].

Non-carbon materials have also been employed; they include metallic nanomaterials, silica nanomaterials, ITO, organic polymers, etc. [92]. As mentioned before, AuNPs are extensively used for genosensing due to the gold-thiol chemistry; additionally, they possess exceptional electrochemical behavior due to their intrinsic metallic behavior and biocompatibility [93]. Nanomaterials such as copper, platinum and silver have also been extensively explored, with silver nanoparticles (AgNPs) at the forefront owing to the similar behavior compared to AuNPs [92], [94]. Finally, porous crystalline materials are interesting for improving the transport of electrons through rational design [92]; ITO is also extensively explored because of its unique optoelectronic characteristics, good conductivity, excellent transmittance, and cost-effectiveness [92].

Conductive polymers are interesting due to the facile tailoring of their electrochemical properties and high synthesis yield. They can be used for the development of low-cost, miniaturized and flexible sensors. Additionally, the correlation of nanocomposites with conducting polymers has been explored to improve catalytic stability due to their combined electrochemical performances [95], [96].

Nucleic acid amplification in conjunction with the electrochemical sensor is a viable approach that provides signal amplification for improved sensor sensitivity. The most well-known method for amplification of nucleic acids is the polymerase chain reaction, which consists of three steps (denaturation, annealing, and extension), each of which requires a different temperature, so the PCR protocol involves thermal cycling. An alternative to PCR is loop-mediated isothermal amplification (LAMP), a technique that allows DNA to be amplified at a constant temperature. It has been used in the construction of electrochemical biosensors for the detection of viruses such as hepatitis B virus (HBV) [97], SARS-CoV-2 [98], and others [99]. There is also recombinase polymerase amplification (RPA), a newer alternative technology that can operate at constant temperatures similar to LAMP to generate nucleic acid copies. Khater et al. proposed solid-phase RPA directly in the electrode for impedimetric detection of *Citrus tristeza virus*; the electrode surface was previously modified with AuNPs to which a thiolated forward primer was attached for in situ isothermal RPA [100]. Rolling circle amplification (RCA), another isothermal method, was used for an electrochemical genosensor to detect a synthetic DNA template of Ebola virus [101].

1.3.2.2 Immobilization of the biological recognition element

The immobilization of the biological recognition element can be either direct or indirect. In the **direct immobilization model**, the biorecognition element is assembled on the electrode surface through physisorption (noncovalent binding), chemisorption, covalent binding, affinity binding [70]. Additionally, the supporting electrode surface can be modified with different means and materials that will either assist in immobilizing the biorecognition element to the working electrode or enhance the electrical signal. Either the electrode surface is coated with polymers or nanoparticles that can interact electrostatically with the probe, or a part of the biorecognition element is modified with an appropriate functional group to form a corresponding bond on the electrode surface for the immobilization [92].

In the **indirect immobilization model**, the biorecognition element is attached to a nanostructure platform that will subsequently be immobilized on the supporting electrode surface. The density and orientation of the element play a significant role in the efficiency of the sensor. With indirect immobilization, there are more possibilities for effective oriented dispersion of the probe. The choice of the best immobilization protocol depends

on the electrode material and the properties of the chosen analyte [70]. An efficient immobilization must guarantee that the target and the biological recognition element will be able to interact effectively, otherwise a poor immobilization can generate false and unreliable signals which could be due to substrate defects, aggregation of or non-specifically adsorbed material [18], [102].

Physisorption relies on the electrostatic attraction between the probe and the electrode surface and does not require special nucleic acid modifications [58]. It is a well-known and commonly used method due to its simplicity, however, it holds many drawbacks since the accessibility of the probe to the target analyte can be impaired due to the close contact of the length of the probe with the electrode surface, causing poor analytical performance of the sensor. One way to try to fight this disadvantage is to modify the electrode surface with a polymeric layer with desirable properties, e.g., biocompatibility, stability or protection of the electrode from nonspecific analyte adsorption [103].

Chemisorption, on the other hand, is when the interaction between the probe and the surface is held together by chemical bonds. The most explored method of this kind involves the usage of a self-assembled monolayer (SAM) of DNA probes, being formed through the chemisorption of the SAM on either gold electrodes or gold nanoparticles (AuNPs). This approach is frequently used for immobilization due to the binding of thiol-modified nucleic acid and gold surface [18]. Besides, the Au-S bond is strong, stable and reproducible; thus, it is widely exploited in genosensing [76].

Covalent binding relies on anchoring the chemically modified end of the probe DNA on the activated surface of a support matrix through the formation of covalent bonds [18]. In contrast to physisorption, its sensing layer has higher stability, flexibility, and binding strength. Additionally, this method can provide a good vertical orientation of the probe DNA, allowing for higher efficiency of the DNA hybridization step. Pyrrole and its derivatives are common in covalent binding; they can be electropolymerized through cyclic voltammetry and generate polymeric films that form a covalent bond with the nucleic acid probe [81]. Additionally, the use of carbodiimide reagents is common in probe immobilization, most of the time N-hydroxysuccinimide (NHS) and 1-ethyl-3-(3-dimethylaminopropyl) carbodiimide (EDC), acting as carboxyl activators to assist the covalent attachment between carboxyl groups and amines [76]. Glutaraldehyde is also used in genosensing design as a cross-linking agent [104].

Affinity binding is a non-covalent immobilization technique that occurs when molecules are bound to the electrode surface through a biorecognition event [44]. The most prominent example of affinity binding is the avidin-biotin system, wherein the DNA probe is biotinylated to bind with the avidin/streptavidin molecules anchored in the electrode [105], [106]. The advantages of this system are its stability and mechanical resistance [70]. Supramolecular interactions are also explored; Ortiz et al. fabricated a DNA sensor based on the interfacial complexation of a bifunctionalized carboxymethylcellulose (CMC) polymer backbone bearing ferrocene units and a DNA probe on a cyclodextrin-functionalized surface [107].

Alternative to the previously mentioned methods, there are the indirect probe immobilization methods, which use structures such as DNA nanoobjects, one-dimensional arrays and 2D and 3D crystalline to attach the probe and provide interaction with the target analyte without necessarily being in contact with the electrode surface. These nanofabricated structures are varied and biocompatible and allow easy attachment of functional materials [70]. A DNA tetrahedron was designed to immobilize the probe to a gold surface via three thiol groups in each tetrahedron vertices, while the DNA probe was attached to the fourth vertex [108]. The 3D tetrahedron structure provided enhanced accessibility of the probe, maintaining the upright orientation of the probes, leading to

elevated efficiency of the target hybridization and consequently high sensitivity and selectivity of the sensor [70], [108].

1.3.2.3 Electrochemical detection and biosensor validation

Although this is the final step in biosensor construction, it is a critical one. Selecting the appropriate electrochemical technique depends on several factors, including: (i) the inherent electrochemical properties of the target analyte, (ii) the most suitable electrolyte or redox probe for measurement, and (iii) the required sensitivity of the biosensor.

The most relevant electrochemical techniques for immunosensors and genosensors are thoroughly discussed in section 1.2.1 of this dissertation.

Regarding validation, an ideal electrochemical biosensor should exhibit the following key characteristics:

Sensitivity: The biosensor must effectively detect the analyte within its relevant concentration range, which varies by target. For instance, glucose biosensors should detect concentrations between 1–10 mmol L^{-1} of glucose in blood, whereas SARS-CoV-2 biosensors must operate within 0.001–10 µg mL^{-1} of spike S1 protein in nasopharyngeal fluid.

Selectivity: The biosensor should specifically recognize the target analyte with minimal or no cross-reactivity to other structurally similar molecules.

Response linearity and calibration: It must maintain linearity over the measurable concentration range, ensuring accurate detection limits and calibration.

Reproducibility: The biosensor should generate consistent analytical signals when measuring identical target concentrations under the same conditions.

Dynamic and stable response: The signal must be precise, free from electrical noise, and suitable for real-time analysis.

Environmental stability: The biosensor should resist variations in pH, temperature, and other physical conditions to ensure reliable performance.

Operational lifespan: The biological recognition element should remain functional over an extended period to allow continuous monitoring.

Additionally, an ideal biosensor should be cost-effective, biocompatible, miniaturized, and suitable for portable, on-site analysis [19].

Chapter 2

Goals and Hypotheses

This dissertation focuses on developing innovative electrochemical devices to detect viruses and viroids, in particular, an immunosensor for SARS-CoV-2 and a genosensor for *Citrus bark cracking viroid*. The purpose of this dissertation is to provide a thorough and systematic study and selection of appropriate supporting electrodes and high-performance sensing interfaces that allow for the detection of specific analytes in the interference-free regime. The choice of the *Citrus bark cracking viroid* as an analyte was governed by the high public demand for the development of a sensing device for the detection of this insidious viroid, being responsible for large economic losses in Slovenia, Germany, and the Czech Republic. On the other hand, it goes without saying that the SARS-CoV-2 pandemic has brought profound socio-economic changes worldwide, and the emergence of potentially more transmissible variants or viruses that may resist commercially available vaccines continues to challenge societies in establishing effective prevention and treatment strategies. Such a situation motivates the competition among research teams to develop and validate viable alternatives to commercially available RT-PCR (reverse transcription polymerase chain reaction) and widely used serological tests.

This dissertation showcases the use of conventional supporting electrodes and disposable screen-printed carbon electrodes. The former offers excellent conductivity and more consistent and reliable electrochemical readings. In contrast, the latter offers the possibility of developing devices for point-of-need applications in the field or clinical setting. In the scope of this work, gelatin is incorporated for the first time as a stable, biocompatible membrane for advanced sensing applications, being able to simultaneously contribute to the higher electrochemical reproducibility of the screen-printed carbon electrodes while serving as an excellent immobilization medium for the biological recognition element. Also, this dissertation presents one of the pioneering works concerning the application of the (electro)catalytic 2D-layered MXenes in electrochemical biosensing and harvesting their large surface-to-area ratio, high adsorption capability, thermal stability, and ease of functionalization. Another purpose of this dissertation is to showcase the direct detection of the target RNA sequence without the necessity for the amplification step by choosing a suitable modification membrane and optimizing the content of the (electro)catalytic component. Finally, this doctoral dissertation provides a comprehensive overview of the biological recognition interactions at the proposed sensing interfaces.

Goals of the dissertation:

- Evaluate available supporting electrodes and select the most suitable for the sensor fabrication;
- Investigate different protocols for direct or indirect binding of the biological recognition elements, such as antibodies and nucleic acid capture sequences;
- Investigate gelatin as a suitable membrane material for use in electrochemical sensing;
- Develop a one-shot electrochemical immunosensor for the detection of the SARS-CoV-2 spike protein using a screen-printed electrode in combination with gelatin as a surface modifier;
- Select suitable (electro)catalytic materials and improve the analytical performance of the sensor architecture, such as 2D and 3D nanomaterials or metal oxides;
- Gain insights into the potential applications of such materials and interfaces in sensor technology by systematically characterizing their electrochemical and physicochemical properties;
- Design a sensor interface with high performance (electro)catalytic materials and develop an electrochemical genosensor for *Citrus bark cracking viroid* without the conventional amplification step;
- Detect the *Citrus bark cracking viroid* in real total RNA samples obtained from fields.

Hypotheses:

1. Screen-printed electrodes can serve as supporting electrodes for sensitive and reproducible biosensors after appropriate pre-treatment, despite their innate irreproducibility; the introduction of gelatin can improve the electrochemical reproducibility of screen-printed carbon electrodes; a stable and biocompatible modifying layer of gelatin will allow for the immobilization of biological recognition elements, such as anti-SARS-CoV-2 antibodies;
2. Electrochemical immunosensors based on the stable gelatin membrane can sensitively and selectively detect the SARS-CoV-2 spike protein in artificial nasopharyngeal fluid;
3. The streptavidin-agarose layer can serve as a suitable immobilization layer for the biological recognition element on the glassy carbon electrode. In addition, the streptavidin-biotin interaction can be used as a suitable way to immobilize a single-stranded biotinylated DNA capture probe that is highly specific for the target sequence of *Citrus bark cracking viroid*;
4. 2D-laminated (electro)catalytic MXenes can be used as a transducing surface in biosensing due to their easy functionalization and can enhance and/or stabilize the analytical signal of an electrochemical genosensor for *Citrus bark cracking viroid*;
5. The proposed electrochemical genosensor containing a streptavidin-agarose layer and (electro)catalytic MXenes can be used for interference-free detection of *Citrus bark cracking viroid* in real total RNA samples.

Chapter 3

Scientific Publications

Three research articles were published in peer-reviewed journals as part of this dissertation.

In **manuscript 1**, an immunosensor for the impedimetric detection of SARS-CoV-2 was developed. Various supporting electrodes were investigated for the development of this sensor, but the SPCE was selected due to its versatility, miniaturization and practicality. To attach the biorecognition element and improve reproducibility, a gelatin layer was applied to the electrode, which was then further processed with EDC/NHS to effectively attach protein A, a protein that binds to the Fc domain of antibodies and leaves the Fab domains free to bind to the target. The SARS-CoV-2 antibody was then introduced, followed by BSA to block non-specific binding on the sensor surface. The gelatin modification of these SPCEs increased their electrochemical reproducibility and enabled the successful fabrication of the electrochemical immunosensor to detect the SARS-CoV-2 spike protein in both standard samples and artificial nasopharyngeal fluid (ANF) with a good linear response and a low limit of detection of 169 pg mL^{-1} (2.2 pM) in PBS and 90 pg mL^{-1} (1.2 pM) in ANF.

In **manuscript 2**, an impedimetric sensor for SARS-CoV-2 based on SPCE was developed, with a higher sensitivity compared to the immunosensor presented in manuscript 1. For this second sensor, the supporting SPCE was modified with V_2CT_x MXene and an additional Nafion immobilization layer. Prior to incubation with the anti-SARS-CoV-2 antibody solution, the SPCE was additionally modified with glutaraldehyde, as a cross-linker, and protein A, for the sake of proper orientation of the anti-SARS-CoV-2 antibodies. The non-specific binding sites were covered with BSA. This immunosensor showed excellent sensitivity and selectivity against the SARS-CoV-2 spike protein with a detection limit of 3.4 pg mL^{-1} (45 fM).

While manuscripts 1 and 2 targeted a virus (SARS-CoV-2), **manuscript 3** shows the development of the first electrochemical sensor to date for the detection of a viroid – CBCVd. In manuscript 3, a GCE was used as the supporting electrode because it is reliable and reproducible when compared to the SPCE. The immobilization layer in this case consisted of streptavidin-agarose beads. Due to the well-known streptavidin-biotin interaction, this layer was ideal for attaching the biotinylated single-stranded DNA (ssDNA), which serves as a capture probe. After the capture probe was introduced into the system, glycine was added to prevent non-specific binding. $Ti_3C_2T_x$ MXene was used in this genosensor to increase stability and sensitivity. It was mixed with the streptavidin-agarose solution and drop-casted onto the electrode. The samples were total RNA obtained from infected and non-infected hop, and the limit of detection was 0.5 fg μL^{-1} (5.5 fM).

In all three manuscripts, the detection signal was obtained through EIS, and the redox probe used was potassium hexacyanoferrate(II)/(III) in KCl.

3.1 Manuscript 1: "Development of a Simple Gelatin-Based Sensing Platform for the Sensitive Label-Free Impedimetric Detection of SARS-CoV-2"

Electrochimica Acta 463 (2023) 142823

Contents lists available at ScienceDirect

Electrochimica Acta

journal homepage: www.journals.elsevier.com/electrochimica-acta

Development of a simple gelatin-based sensing platform for the sensitive label-free impedimetric detection of SARS-CoV-2

Alnilan Lobato [a,b], Maja Šubic [a], Tea Romih [a], Lea Žibret [a], Dino Metarapi [a], Mojca Benčina [c], Roman Jerala [c], Kristijan Vidović [a], Samo B. Hočevar [a,*], Nikola Tasić [a,*]

[a] Department of Analytical Chemistry, National Institute of Chemistry, Ljubljana, Slovenia
[b] International Postgraduate School Jožef Štefan, Ljubljana, Slovenia
[c] Department of Synthetic Biology and Immunology, National Institute of Chemistry, Ljubljana, Slovenia

ARTICLE INFO

Keywords:
Impedimetric immunosensor
Gelatin-based sensing platform
SARS-CoV2 S1 protein
Label-free disposable sensor
Artificial nasopharyngeal fluid

ABSTRACT

The persistent nature of the SARS-CoV-2 virus, characterized by its large-scale periodical recurrence and high infectivity, has imposed an increasing demand for rapid and frequent tests. This paper presents a simple, disposable, sensitive, and selective label-free sensor for impedimetric detection of the virus Spike S1 protein. We modified a screen-printed carbon electrode with gelatin as the biocompatible support to deposit a protein A layer, acting as the structure-directing agent for subsequent site-induced binding of antibodies. We thoroughly investigated the main design factors, such as gelatin deposition, protein A and antibody concentrations, incubation time, BSA blocking time, followed by the analytical performance studies using the Spike S1 protein in phosphate-buffered saline (PBS) and artificial nasopharyngeal fluid (ANF). The immunosensor exhibited an excellent linear impedimetric response for Spike S1 in the clinically-relevant range of 0.001 - 10 μg mL^{-1} (13 pM - 130 nM), along with very low limits of detection of 169 pg mL^{-1} (2.2 pM) in PBS and 90 pg mL^{-1} (1.2 pM) in ANF. Together with favorable stability, repeatability, and selectivity, the newly developed immunosensor can be designated for its point-of-need application.

1. Introduction

During the past two and a half years, humanity has witnessed a large socio-economical catastrophe due to the SARS-CoV-2 pandemic. The significant infectivity of the novel virus strains, accompanied by the incoherency of the proposed preventive and vaccination strategies, and flexible abidance to the imposed measures, has led to the omnipresence of the virus and increased demand for the testings. This is additionally emphasized by the growing concerns about the adverse effects of the virus on the organs, especially the respiratory system [1]. Thus far, over half a billion people have been infected with a variant of COVID-19, resulting in more than 6.8 million deaths.

As the most viable alternative to conventional molecular and serological tests, which dominate in practical applications, various types of electrochemical immunosensors have recently emerged [2]. With properly chosen and optimized protocols for the fabrication and modification of the supporting electrode materials with stable, functional biorecognition elements and by employing different sensing strategies, clinically relevant limits of detection could be achieved in a relatively short time [3]. Moreover, taking into account significant breakthroughs toward miniaturized instrumentation, mobility, and facile data acquisition, the electrochemical sensors seem promising for point-of-need applications [4]. The existing literature recognizes voltammetric detection methods as the most frequently utilized for the detection of both specific antibodies and antigens [5–10], followed by devices based on impedimetric measurements [11–17].

Most state-of-art electrochemical sensing platforms for detecting SARS-CoV-2 are based on the supporting electrodes modified with functional (nano)materials exploiting their advantages such as the enhanced charge transfer, electrocatalytic effect, surface roughness, and typically large electroactive surface area [18]. Recently, Adeel et al. synthesized flexible graphitic carbon foil for covalent immobilization of anti-SARS-CoV-2 antibodies via ethylenediamine functionalization and EDC/NHS cross-linking for the voltammetric detection of the Spike S1 protein in PBS (pH=7.4) and diluted blood serum [19]. Similarly, they prepared AuNPs-coated carbon cloth electrodes, modified with a

* Corresponding authors at: Department of Analytical Chemistry, National Institute of Chemistry, Hajdrihova 19 SI-1000 Ljubljana, Slovenia.
E-mail addresses: samo.hocevar@ki.si (S.B. Hočevar), nikola.tasic@ki.si (N. Tasić).

https://doi.org/10.1016/j.electacta.2023.142823
Received 29 December 2022; Received in revised form 30 June 2023; Accepted 3 July 2023
Available online 4 July 2023
0013-4686/© 2023 The Authors. Published by Elsevier Ltd. This is an open access article under the CC BY-NC-ND license (http://creativecommons.org/licenses/by-nc-nd/4.0/).

thiol-functionalized DNA aptamer for the detection of Spike S1 protein in PBS (pH=7.4) and diluted human saliva [20]. Another way to detect SARS-CoV-2 via impedimetric and amperometric quantification of its nucleic acid was demonstrated by the glassy carbon electrode modified with multi-walled carbon nanotubes (MWCNTs) non-covalently functionalized with avidin as affinity support for the biotinylated-DNA capture probes [21]. Obviously, the choices for electrode modification materials are quite diverse in order to provide selective and sensitive platforms for the detection of SARS-CoV-2, which is in-details reviewed elsewhere [18,22].

On the other hand, our strategy is based on utilizing a biocompatible gelatin polymeric support for the successful incorporation of the biorecognition element while providing a reproducible, stable, and selective electrochemical signal. Gelatin is a three-dimensional biopolymer obtained by acidic or alkaline processing of collagen, a protein that originates from the connective tissues of various animals. It is a suitable medium for ionic transport owing to its hydrophilicity and good immobilization or entrapment capability for enzymes, cells, tissues, and aptamers [23–25]. Apart from its functional versatility, gelatin also complies with the contemporary demands for environmentally friendly and biodegradable agents [26]. However, to the best of our knowledge, its usage in electrochemical bio-affinity sensors for antigen detection is surprisingly scarce and limited only to entrapment purposes. In one of a few publications on gelatin-based electrochemical sensors, gelatin was used to entrap the HRP-labelled hepatitis B antibodies previously attached to the Nafion-modified platinum disk electrode; quantification of the antigens was carried out potentiometrically [27]. In another study, gelatin was mixed with colloidal silver particles and anti-AFP antibodies on the platinum disk electrode to form a sensing membrane for potentiometric detection of α-fetoprotein [28].

Herein, we present a novel approach in which gelatin serves as a biocompatible surface modifier for the screen-printed carbon electrode, acting as the supporting building block incorporating biorecognition elements via site-directed binding. The latter was achieved by integrating a protein A layer as the linker prior to the immobilization of specific antibodies. Our research involves several optimization steps to enhance the electroanalytical characteristics of a newly developed label-free disposable sensor. The sensor exhibited good performance for highly sensitive and selective detection of COVID-19 Spike S1 protein in phosphate-buffered saline (PBS) and in the artificial nasopharyngeal fluid (ANF).

2. Experimental

2.1. Chemicals

All commercial reagents were of analytical grade and were used without further purification. All aqueous solutions were prepared using ultrapure water with resistivity not less than 18.2 MΩ cm at 298 K (Milli-Q, Millipore, Corp., Marlborough, USA).

Gelatin from porcine skin (gel strength 300, Type A), 4-morpholineethanesulfonic acid monohydrate (MES), Sodium azide (NaN_3), 1-ethyl-3-(3'-dimethyl aminopropyl)carbodiimide, HCl (EDC), N—Hydroxysuccinimide, 89% (NHS) and Bovine Serum Albumin (BSA) were purchased from Sigma Aldrich (St. Louis, USA). Sodium phosphate dibasic ($Na_2HPO_4{\cdot}2H_2O$) and glycerol ($C_3H_8O_3$, redistilled, *pro analysis*) were purchased from Kemika, Pliva (Zagreb, Croatia). Sodium hydroxide (NaOH) and sodium chloride (NaCl) were purchased from Merck (Darmstadt, Germany). N,N-dimethylformamide, potassium phosphate monobasic (KH_2PO_4), and potassium hexacyanoferrate (III) ($K_3[Fe(CN)_6]$) were purchased from Fluka (Buchs, Switzerland). Potassium chloride (KCl) and potassium hexacyanoferrate (II) ($K_4[Fe(CN)_6]$) were purchased from Riedel-de Haën (Seelze, Germany). Protein A (ab71456), human monoclonal anti-SARS-CoV-2 Spike glycoprotein S1 antibodies (ab286179), and recombinant human coronavirus SARS-CoV-2 Spike glycoprotein S1 (ab273068) were purchased from Abcam (Cambridge, UK). Artificial nasopharyngeal fluid (ANF) was purchased from BioCHEMAZONE (Hamilton, ON, Canada).

2.2. Preparation of buffers

MES buffer was prepared by dissolving 5.33 g of MES monohydrate in 250.0 mL of purified H_2O. Phosphate-buffered saline (PBS, pH=7.4) was prepared by dissolving 8.00 g of NaCl, 200.0 mg of KCl, 1.81 g of $Na_2HPO_4{\cdot}2H_2O$, and 240.0 mg of KH_2PO_4 in 1.0 L of purified H_2O. When the PBS was used to dilute proteins, 0.001% of NaN_3 was added to the solution as a preservative.

2.3. Modification of the working electrode and sensor fabrication

The screen-printed carbon electrodes (SPCEs) were modified using an optimized procedure as follows: 0.10 g of gelatin was dissolved in 9.5 mL of purified H_2O at 50 °C, followed by the addition of 500 μL of 100% glycerol. After thorough and vigorous homogenization using a magnetic stirrer, 12 μL of the suspension (cooled down to room temperature) was carefully drop-casted onto the working electrode of the SPCE unit. Afterward, the deposited layer was left to dry on air in a model atmosphere (22–23 °C) for at least 36 h before use.

Bare and gelatin-modified SPCEs were subjected to optical inspection using profilometry (Zegage PRO HR, Zygo Corporation, PA). 3D information was obtained using a 50× magnification lens with a lateral resolution of 0.52 mm, and a surface topography repeatability of ≤3.5 nm.

After the completion of the drying step, which was visually characterized by the noticeable formation of a thick transparent layer, the electrodes were left for one hour at 4 °C in the solution containing 400.0 mM EDC and 100.0 mM NHS in MES (pH=5.5). After that, the electrodes were rinsed in PBS and then in purified H_2O to remove the unreacted species, followed by drying under a mild stream of nitrogen at 0.2 bar. After introducing the cross-linkers, the working electrodes were incubated with protein A solution (20–100 μg mL^{-1}) in MES (pH=5.5) for one hour, followed by rinsing with purified H_2O and drying under the nitrogen stream. In the next step, 10 μL of the anti-SARS-CoV-2 Spike glycoprotein S1 antibodies, with concentrations ranging from 5 to 50 μg mL^{-1} in PBS, was carefully cast onto the working electrode and left for up to one hour, incubating at room temperature. After rinsing off the unbound antibodies with PBS, the non-active antibody sites were blocked with the addition of BSA (10 μg mL^{-1} in PBS) and subsequently rinsed and dried. Incubation with Spike S1 protein was performed at room temperature for 15–120 min, and its electrochemical detection was conducted by electrochemical impedance spectroscopy (EIS) measurements in the presence of 1.0 mM $[Fe(CN)_6]^{3-/4-}$ redox couple in 0.1 M KCl.

2.4. Electrochemical measurements

All electrochemical measurements were performed using a portable PalmSens 4 electrochemical system operated by the software PSTrace 5.9 (PalmSens BV, Netherlands). EIS spectra (Nyquist plots) were recorded in the frequency range of 10^5–10^{-1} Hz at the formal potential of +0.14 V vs. integrated silver quasi-reference electrode (at the SPCE) and an amplitude of 20 mV, using 1.0 mM $[Fe(CN)_6]^{3-}/^{4-}$ in 0.1 M KCl as a redox probe. The experiments were carried out using the supporting screen-printed carbon electrodes (SPCEs, DropSens, DRP-C110) purchased from Metrohm (Herisau, Switzerland) with a 4 mm diameter of the working electrode. For each measurement, the working, reference, and counter electrodes were covered with a 50 μL drop of the redox probe solution.

3. Results and discussion

3.1. Fabrication of the immunosensor

Deposition of the gelatin onto the SPCE was performed by drop-casting the gelatin solution containing glycerol as the rheological agent that assures uniform distribution and satisfactory thickness homogeneity of the coating. The latter was investigated by 3D profilometry, and the corresponding results are presented in Fig. 1. As can be seen, the bare SPCE exhibits a relatively rough surface profile (Fig. 1**a and b**), resembling the structure of a well with an outer ring of approx. 400 μm wide, irregular base with a diameter of approx. 3.0 mm and roughness of 1.36±0.04 μm ($n = 3$).

Upon the deposition of gelatin and subsequent drying, the surface roughness was reduced to 0.85±0.06 μm ($n = 3$), with an average gelatin coating height of 11.2 μm (Fig. 1b). The significant reduction of roughness (≈38%) suggests that the gelatin layer is efficiently thick and homogenous enough to compensate for both the roughness and irregular 3D nanostructure of the supporting electrode surface, as depicted in Fig. 1c.

In addition, randomly selected bare SPCEs ($n = 20$) were subjected to EIS measurements in 1.0 mM $[Fe(CN)_6]^{3-/4-}$ before and after modification with gelatin. The relative standard deviation (RSD) of the charge transfer resistance (R_{CT}) obtained by fitting the raw EIS data of unmodified SPCEs was 23.8% (1291.6 ± 68.9 Ω), whereas the R_{CT} of gelatine-modified SPCEs exhibited an RSD of 16.6% (1285.6 ± 47.6 Ω). Importantly, the attenuation of RSD implies that the deposition of gelatin also reduced the intrinsic electrochemical irreproducibility of the SPCEs, making them more applicable for (bio)sensor fabrication. The corresponding measurements, along with fitting parameters, are summarized in **Figure S1** and **Table S1**, respectively.

Multi-step construction of the immunosensor was monitored by EIS measurements in 1.0 mM $[Fe(CN)_6]^{3-/4-}$ with the corresponding results presented in Fig. 2, whereas the extracted fitting parameters are listed in Table 1. The deposition of gelatin was characterized by a significant change in the Nyquist spectrum and the occurrence of a small semicircle, which was attributed to the charge transfer within the deposited gelatin coating (Fig. 2b). The raw impedance data were fitted using the equivalent circuit R_S-(R_{GEL}||Q_1)-((R_{CT}-W)||C_1). Herein, R_S corresponds to the solution resistance, R_{GEL} reflects the low resistance of the heterogeneous gelatin layer, Q_1 is the non-ideal capacitance of the gelatin layer (non-ideal due to the typical presence of some sequestered water molecules and/or ions, non-ideal surface, pinholes, etc.), R_{CT} is the charge transfer resistance of the upper sensing layer (related to the antibody-antigen interaction), W is the Warburg element that models the diffusion phenomena, and C_1 is the double-layer capacitance of the upper sensing layer.

The first modification step was the introduction of the EDC/NHS cross-linking pair via its reaction with the gelatin COOH groups to ensure proper chemical binding of proteins. By taking into account the heterogeneous structure of gelatin originating from the porcine skin, there are two possibilities for the protein binding, i.e., one via the proposed chemical route involving gelatin carboxyl groups (78 COOH groups per 100 amino acids) for binding with protein A using EDC/NHS protocol, and an alternative one based on the direct random adsorption of the proteins. The chemical route leads to the preferentially oriented antibodies in a stable arrangement, in which protein A binds to the Fc domain of the antibody while leaving the antibody Fab domains exposed for the binding with the target antigen. On the other hand, random adsorption of antibodies would result in an unstable sensing surface, prone to protein reorientation, denaturation, and low binding capacity towards the target antigen. Thus, to promote the chemical route, we soaked the gelatin-modified SPCEs in a solution containing 400.0 mM EDC and 100.0 mM NHS in MES (pH=5.5) followed by the gelatin carboxyl groups cross-linking with protein A that binds with the Fc region of the anti-SARS-CoV-2 antibodies. The intermediate ester (gelatin-COO-EDC) and the amine-reactive sulfo-HNS ester (product of the reaction between gelatin-COO-EDC and NHS) both react with the protein A to form stable conjugates via the amide bond. Simultaneously, the unstable gelatin-COO-EDC intermediate can hydrolyze and liberate carboxylic groups of the gelatin. This effect can be minimized with the appropriate pH of the reaction solution and temperature. A certain quantity of isourea is produced as the byproduct related to the NHS reaction path. It must be noted that the existing EDC/NHS protocols vary a lot in terms of reaction conditions, i.e., the molar ratio between the reagents and their overall concentrations, choice of the solvents, treatment temperature, and duration. In this study, the procedure was carried out at 4 °C, to ensure the stability of the reagents, which were introduced in MES buffer of specific pH of 5.5 (NHS : EDC = 0.25), aiming for prolonged durability of the formed NHS ester intermediate, and to avoid side-reactions, such as the spontaneous hydrolysis [29,30].

The introduction of the EDC/NHC pair in the sensor's architecture resulted in a relatively large R_{CT} amplification (1062.73 → 3612.33 Ω), suggesting that significant cross-linking density was achieved (Fig. 2c). This was followed by a small drop of R_{CT} upon the introduction of protein A (3612.33 → 2886.33 Ω), as shown in Fig. 2d. This decrease of the R_{CT} upon introduction of protein A and rinsing suggests that only the chemically bonded protein A remains in the sensing structure and that the excess of EDC and NHS, previously added in a 4:1 ratio, and byproducts, are washed from the gelatin, thus leaving more active sites for the redox probe signaling.

The introduction of protein A induced a site-directed End-on Fab-up immobilization of the anti-SARS-CoV-2 Spike glycoprotein S1 antibodies via their Fc fragments, which enhances antigen binding efficiency and consequently results in improved immunosensor sensitivity [31]. Such an approach is an alternative to the random adsorption of antibody molecules [32] or conventional, by far the most utilized antibody immobilization protocol, with thiol-based self-assembled monolayers deposited onto various types of supporting electrodes [33–36]. Compared to random adsorption, the latter approach enables better stability and potential reusability owing to the covalent bonds but still suffers from the decreased availability of active antibody sites due to their arbitrary orientation [37].

Furthermore, the addition of antibodies (5 μg mL^{-1}, incubation of 60

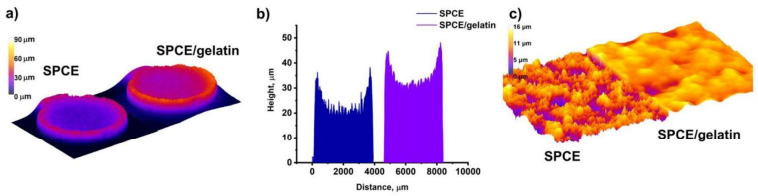


Fig. 1. 3D profilometry imaging (a), thickness profile (b), and morphology (c) of the SPCE before and after modification with gelatin.

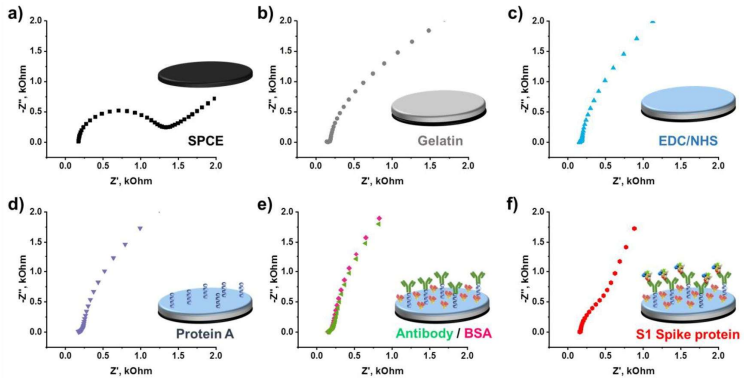


Fig. 2. Step-by-step fabrication of the immunosensor monitored by EIS (Niquist plots) in the presence of 1.0 mmol L^{-1} $[Fe(CN)_6]^{3-/4-}$ in 0.1 mol L^{-1} KCl at bare SPCE (a), (a)+gelatin (b), (b)+EDC/NHS (c), (c)+protein A (d), (d)+anti-SARS-CoV-2 Spike glycoprotein S1 antibody and BSA (e), (e)+Spike S1 protein (f).

Table 1
Fitted parameters of the obtained raw impedance data presented in Fig. 2.

Step/parameter	R_S, Ω	R_{GEL}, Ω	Q_1, μT	n, ϕ	R_{CT}, Ω	W, kσ	C_1, mF
Gelatin	150.83	41.09	221.17	0.66	1062.73	1.42	0.266
	±	±	±	±	±	±	±
	2.03	1.45	42.87	0.04	65.10	0.07	0.011
EDC/NHS	160.37	113.03	560.77	0.56	3612.33	1.98	0.229
	±	±	±	±	±	±	±
	3.03	7.02	46.77	0.01	199.00	0.05	0.015
Protein A	165.03	88.97	532.23	0.57	2886.33	2.25	0.201
	±	±	±	±	±	±	±
	3.19	10.37	145.30	0.03	116.91	0.11	0.013
Antibody	156.77	122.10	595.90	0.57	4236.33	2.38	0.198
	±	±	±	±	±	±	±
	5.82	5.02	77.02	0.02	377.27	0.23	0.002
BSA	158.57	108.64	499.20	0.64	4425.00	2.22	0.196
	±	±	±	±	±	±	±
	4.43	4.07	105.04	0.04	472.25	0.18	0.011
Spike S1	157.93	346.63	160.10	0.96	6153.33	3.17	0.199
	±	±	±	±	±	±	±
	4.79	27.36	5.94	0.01	91.67	0.13	0.003

min) resulted in a typical increase of the R_{CT} (2886.33 → 4236.33 Ω) demonstrated in Fig. 2e. This increase is associated with the formation of a biorecognition layer which suppresses the charge transfer between the redox-active probe molecules and the supporting electrode surface. Blocking of the unoccupied sites with BSA (10 μg mL^{-1}, incubation of 30 min) was characterized by a discrete rise of the impedance (4236.33 → 4425.00 Ω), whereas the 60 min incubation with the analyte, i.e., Spike S1 protein (10 μg mL^{-1}), yielded a rise in both R_{CT} (4425.00 → 6153.33 Ω), and R_{GEL} (108.64 → 346.63 Ω), suggesting strong affinity of the sensing surface towards binding the antigen (Fig. 2f). Alternatively, the build-up process of the sensor was characterized by the square-wave voltammetric (SWV) measurements, with the corresponding data presented in **Figure S2**. The obtained voltammetric results showed peak current changes consistent with the impedimetric measurements.

3.2. Optimization studies

Aimed at improving the electroanalytical response of the immunosensor, we carried out studies of several key parameters related to the sensor's fabrication, including protein A concentration, antibody concentration, BSA blocking time, and Spike S1 protein incubation time. The relative increase of the sensor's charge transfer resistance (R_{CT}) upon the incubation with 10 μg mL^{-1} Spike S1 protein was used as the feedback signal (ΔR) to determine the optimal parameters for sensor design. To obtain the R_{CT} values, the recorded raw impedance spectra were fitted using the appropriate Randles-type equivalent circuit, i.e., R_S-(R_{GEL}IIQ$_1$)-(($R_{CT}W$)IIC$_1$), explained in Section 3.1. All measurements during the optimization experiments were carried out in triplicates.

As expected, the largest change in the analytical signal was detected by altering the Spike S1 incubation time. A gradual increase of the ΔR was observed in the range of 30–60 min, followed by a mildly rising trend up to 120 min of incubation, indicating the commencement of saturation (Fig. 3a). Since the reproducibility of the signal for the last examined point at 120 min was rather low, i.e., implying the intrinsic rearrangements within the protein layer [38], we adopted 60 min as the optimal incubation time for further investigation. In the next study, we tackled the effect of BSA blocking time on the immunosensor response. We observed that the prolonged blocking time in the range of 0–45 min resulted in a somewhat decreased immunosensor response, as depicted in Fig. 3b, with 30 min being the most optimal blocking time considering the signal reproducibility and signal height. When increasing the anti-SARS-CoV-2 antibody concentration, the sensor revealed the

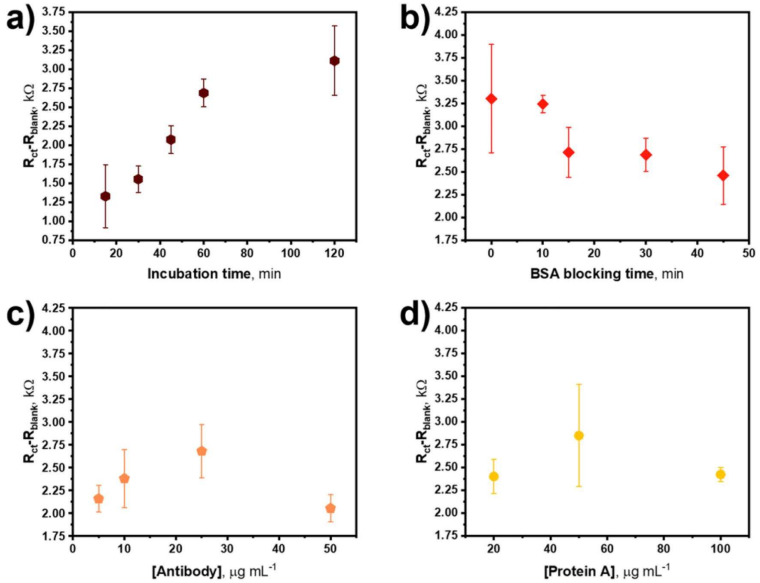


Fig. 3. EIS response of the immunosensor upon changing: incubation time t_{inc} ([Antibody]=15 μg mL^{-1}, [protein A]=20 μg mL^{-1}, [BSA]=10 μg mL^{-1}, t_{BSA}=30 min) (a), BSA blocking time t_{BSA} ([BSA]=10 μg mL^{-1}, [Antibody]=15 μg mL^{-1}, [protein A]=20 μg mL^{-1}, t_{inc}=60 min) (b), antibody concentration ([protein A]=20 μg mL^{-1}, [BSA]=10 μg mL^{-1}, t_{BSA}=30 min, t_{inc}=60 min) (c), and protein A concentration ([Antibody]=5 μg mL^{-1}, t_{inc}=60 min, [BSA]=10 μg mL^{-1}, t_{BSA}=30 min) (d). The signals were obtained upon incubation with 10 μg mL^{-1} of Spike S1 protein in PBS (pH=7.4) using the fully fabricated sensor.

highest response for the concentration of 25 μg mL^{-1}, as shown in Fig. 3c; however, the highest signals were at the same time less reproducible. Considering the most favorable compromise between the reproducibility and signal height, we choose the antibody concentration of 5 μg mL^{-1} as an optimum. A similar trend was observed in examining the effect of protein A concentration on the immunosensor response (Fig. 3d). In this case, the concentration of 100 μg mL^{-1} of protein A exhibited the optimal ratio between the signal height and reproducibility. It is evident that the examined parameters are interdependent; thus, the preparation of the immunosensor requires thorough optimization of each parameter to provide improved sensitivity and reproducibility. The corresponding data related to the EIS measurements of this optimization study are summarized in **Tables S2-S5** in the Supporting Information.

3.3. *Analytical performance and sample analysis*

The electroanalytical performance of the immunosensor was investigated in PBS samples and in simulated real samples of ANF, both spiked with protein S1, and the corresponding EIS measurements are presented in Fig. 4.

The raw impedance data were fitted using the equivalent circuit R_S-(R_{GEL}IIQ$_1$)-(($R_{CT}W$)IIC$_1$), and the related fitting parameters are summarized in **Tables S6-S7.** Diffusion contribution was elucidated by plotting the frequency-related admittance Cole-Cole plots, presented in **Figure S3**. The small semicircle, i.e., the high-frequency semicircle described by R_{GEL}IIQ$_1$ loop, can be assigned to the gelatin itself (inset of Fig. 4a and c). The structural complexity of gelatin can result in a small portion of its structure remaining unmodified, thus being exposed as the charge transfer membrane that is characterized by a small resistance pattern at high frequencies, which is essentially constant throughout the biosensor's fabrication procedure and its sensing operation. However, only at the highest antigen concentration in PBS, i.e., 10 μg mL^{-1}, the contribution of the high-frequency semicircle becomes noticeable and is excellently fitted by the proposed loop. Nevertheless, this adsorption-based phenomenon does not compromise the analytical loop of the proposed equivalent circuit, i.e., ($R_{CT}W$)IIC$_1$. When tested in PBS solution (Fig. 4a and 4b), the new immunosensor exhibited an excellent linear operation in the examined concentration range of 0.001–10 μg mL^{-1} Spike S1 protein with r^2 of 0.99 and a favorably low limit of detection of 169 pg mL^{-1} (2.2 pM).

A good intraday repeatability value of 6.2% was obtained for the impedimetric measurements carried out in a PBS solution containing 0.01 μg mL^{-1} of Spike S1 protein (n = 5, R_{CT}=4996.8 ± 138.9 Ω). In spiked ANF solution (Fig. 4c and 4d), the immunosensor also revealed satisfactory linear operation in the same examined concentration range of 0.001–10 μg mL^{-1} with a slightly lower r^2 of 0.98 along with an even lower limit of detection of 90 pg mL^{-1} (1.2 pM). An intraday repeatability value of 9.5% was calculated for the measurements performed in an ANF solution containing 1.0 μg mL^{-1} of Spike S1 protein (n = 5, R_{ct} = 3004.4 ± 116.7 Ω).

To obtain additional insights into the electroanalytical performance of the immunosensor, we investigated its operation in the presence of model interferents, such as protein N (MW = 49.5 kDa) and BSA (MW = 68 kDa). The latter was chosen as an interferent because of its structural similarity to Spike S1 protein in terms of molecular weight, although it cannot be found in real samples, whereas the former was selected as potentially present interference as a constituent of the SARS-COV-2

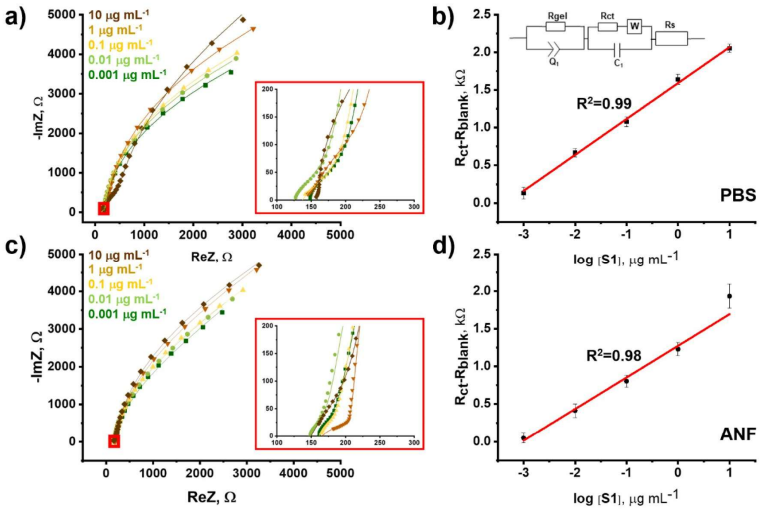


Fig. 4. EIS responses for increasing concentrations of Spike S1 protein in PBS (pH=7.4) (a) together with calibration curve (b), and in simulated real samples (ANF spiked with Spike S1 protein) (c) together with calibration curve (d); the inset in Fig. 4b depicts the equivalent circuit model. Measurements were carried out in triplicates using the optimized sensor fabrication parameters.

virus. For this purpose, PBS solutions containing 10 μg mL^{-1} of each analyte were used in combination with 60 min incubation time. The selectivity factor (α) was calculated by dividing the analytical (impedimetric) signal corresponding to the interferent by the signal of Spike S1 protein; the obtained results for α are depicted in Fig. 5 as a column chart.

As can be seen, responses for protein N and BSA, i.e., 20% increase and 32% decrease of the signal, respectively, compared to the signal of Spike S1 protein, suggest certain level of interactions between the sensing structure and chosen interfering proteins, meaning that their presence in the sample could somewhat compromise the virus quantification. This is mainly attributed to the high affinity of the biorecognition antibody moieties, i.e., anti-SARS-CoV-2 Spike glycoprotein

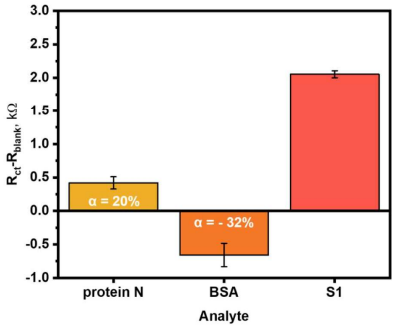


Fig. 5. EIS response of the immunosensor (Δ*R*) in the presence of interferents with corresponding α values.

S1 antibodies, and the insusceptibility of the sensing surface toward interactions with the chosen interferents.

Additionally, we investigated the short-term stability of our sensor by performing measurements of 0.1 μg mL^{-1} Spike S1 protein in ANF, after three and seven days of sensor storage in the refrigerator at 4 °C (n = 2). On day 3, the EIS measurements revealed 106.2% of the R_{CT} signal measured on day 1, whereas on day 7, the immunosensor exhibited 102.2% of the signal measured on day 1. Interestingly, at the same time, the relative standard deviation of the EIS measurements decreased from the initial 6.0% on day 1 to 1.0% on day 7; such good stability and overall electroanalytical performance can be primarily attributed to the obviously absent denaturation of the antibodies due to the chosen storage conditions, and more importantly, due to the immunosensor's surface integrity assured by the gelatine-based sensing platform, retaining antibody orientation, and BSA blocking functionality.

As a final note, we have provided a short review of the proposed impedimetric, label-free, Faradaic sensors for the detection of SARS-CoV-2 in Table 2, showing their diverse characters through the complexity of their structures and operating mechanisms. The reported sensing platforms include molecularly-imprinted polymer detection [14, 16] and more common antibody-antigen-affinity sensors; some of them also involving functional nanoparticles such as reduced graphene oxide [12], graphene [11], or metal-organic frameworks [17]. In the context of the biorecognition element immobilization, several protocols are reported, including Au-thiol [13], biotin-streptavidin [15], cysteamine/glutaraldehyde [17], and EDC/NHS [12]. Some of the proposed sensors even demonstrate limits of detection, which were beyond belief just a decade ago [11]. Comparatively, we have proposed a sensitive, simple, gelatin-based, and yet stable sensing platform, combined with a label-free operation and excellent immunosensing performances encompassing favorably low limits of detection, favorable selectivity, and high linearity in the clinically-relevant concentration range.

Table 2
A brief overview of impedimetric Faradaic platforms for detection of SARS-CoV-2.

Electrode material	Modifier and target analyte	LOD
Macroporous Au-SPE [16]	molecularly-imprinted ortho-phenylenediamine: virus (and RBD) as target	0.7 (and 40) pg mL^{-1}
SPCE [14]	CNTs/WO_3 - molecularly-imprinted 3-aminophenol: virus as target	57 pg mL^{-1}
GCE [12]	r-GO - EDC/NHS – Ab: RBD as target	150ng mL^{-1}
Graphene/carbon SPE [11]	PBASE - Protein A - IgG as biorecognition element: RBD as target	0.25 fg mL^{-1}
SPCE [17]	SiO_2@UiO-66 nanocomposite - cysteamine and glutaraldehyde: S1 as target	100 fg mL^{-1}
ITO [13]	AuNPs - thiol - EDC/NHS - anti-RBD as biorecognition element: RBD as target	0.577 fg mL^{-1}
Au electrode [15]	thiol - EDC/NHS, streptavidin, biotin, peptide as a biorecognition element: S1 as target	r. 0.05 - 10 μg mL^{-1}
SPCE [this study]	gelatin - EDC/NHS - protein A – Ab: S1 as target	90 pg mL^{-1}

Au-SPE - screen-printed gold electrode, CNTs - carbon nanotubes, r-GO - reduced graphene oxide, RBD - receptor binding domain, GCE - glassy carbon electrode, PBASE - 1-pyrenebutanoic acid succinimidyl ester, UiO-66 - metal organic framework, ITO - Indium-doped tin oxide, AuNPs - gold nanoparticles. r – range.

4. Conclusions

We have developed a disposable and label-free impedimetric sensor for sensitive detection of the SARS-CoV2 Spike S1 protein. This was achieved by the introduction of a gelatin-based sensing platform in combination with the supporting screen-printed carbon electrode (SPCE), resulting in an improved electrochemical reproducibility of the SPCE itself and excellent suitability for further surface modifications with protein A and corresponding antibodies. Thorough optimization of the design parameters revealed that a relatively low concentration of the anti-SARS-CoV-2 Spike glycoprotein S1 antibodies (5 μg mL^{-1}) was efficient in achieving a high and stable impedimetric signal. A good linear response was demonstrated in the clinically-relevant concentration range of 0.001–10 μg mL^{-1} Spike S1 protein in PBS, accompanied by a fairly low detection limit of 169 pg mL^{-1} (2.2 pM). The immunosensor disclosed a favorable functioning in the simulated real sample, i.e., in spiked ANF, with an excellent limit of detection of 90 pg mL^{-1} (1.2 pM). We can conclude that a gelatin-based sensing platform imparts efficient integrity of the sensing layers and, together with diligently optimized design and operational parameters, provides excellent analytical performances that can compete favorably or even surpass the existing immunosensing schemes.

CRediT authorship contribution statement

Alnilan Lobato: Investigation, Visualization, Formal analysis, Data curation. **Maja Šubic:** Investigation, Formal analysis. **Tea Romih:** Conceptualization, Methodology. **Lea Zibret:** Investigation, Formal analysis. **Dino Metarapi:** Investigation, Formal analysis, Data curation, Visualization. **Mojca Benčina:** Conceptualization, Methodology. **Roman Jerala:** Conceptualization, Funding acquisition. **Kristijan Vidović:** Writing – review & editing. **Samo B. Hočevar:** Conceptualization, Methodology, Supervision, Funding acquisition, Writing – review & editing. **Nikola Tasić:** Investigation, Supervision, Visualization, Conceptualization, Methodology, Writing – original draft, Writing – review & editing.

Declaration of Competing Interest

The authors declare that they have no known competing financial interests or personal relationships that could have appeared to influence the work reported in this paper.

Data availability

Data will be made available on request.

Acknowledgments

This research received funding from the Slovenian Research Agency (Research Programs P1-0034 and P4-0176 and Research Project V4-2038) and the Slovenian Research Agency's Young Researchers Programme (grant agreement No. 56119).

Supplementary materials

Supplementary material associated with this article can be found, in the online version, at doi:10.1016/j.electacta.2023.142823.

References

[1] M.D. Shah, A.S. Sumeh, M. Sheraz, M.S. Kavitha, B.A. Venmathi Maran, K. F. Rodrigues, A mini-review on the impact of COVID 19 on vital organs, Biomed. Pharmacother. 143 (2021), 112158, https://doi.org/10.1016/j.biopha.2021.112158.
[2] A.K. Kaushik, J.S. Dhau, H. Gohel, Y.K. Mishra, B. Kateb, N.-Y. Kim, D.Y. Goswami, Electrochemical SARS-CoV-2 sensing at point-of-care and artificial intelligence for intelligent COVID-19 management, ACS Appl Bio Mater 3 (2020) 7306–7325, https://doi.org/10.1021/acsabm.0c01004.
[3] W.T. Sow, F. Ye, C. Zhang, H. Li, Smart materials for point-of-care testing: from sample extraction to analyte sensing and readout signal generator, Biosens. Bioelectron. 170 (2020), https://doi.org/10.1016/j.bios.2020.112682.
[4] J. Kudr, P. Michalek, L. Ilieva, V. Adam, O. Zitka, COVID-19: a challenge for electrochemical biosensors, TrAC Trends Anal. Chem. 136 (2021), 116192, https://doi.org/10.1016/j.trac.2021.116192.
[5] A. Yakoh, U. Pimpitak, S. Rengpipat, N. Hirankarn, O. Chailapakul, S. Chaiyo, Paper-based electrochemical biosensor for diagnosing COVID-19: detection of SARS-CoV-2 antibodies and antigen, Biosens. Bioelectron. 176 (2021), 112912, https://doi.org/10.1016/j.bios.2020.112912.
[6] L. Fabiani, M. Saroglia, G. Galatà, R. de Santis, S. Fillo, V. Luca, G. Faggioni, N. D'Amore, E. Regalbuto, P. Salvatori, G. Terova, D. Moscone, F. Lista, F. Arduini, Magnetic beads combined with carbon black-based screen-printed electrodes for COVID-19: a reliable and miniaturized electrochemical immunosensor for SARS-CoV-2 detection in saliva, Biosens. Bioelectron. 171 (2021), 112686, https://doi.org/10.1016/j.bios.2020.112686.
[7] A. Idili, C. Parolo, R. Alvarez-Diduk, A. Merkoçi, Rapid and efficient detection of the SARS-CoV-2 spike protein using an electrochemical aptamer-based sensor, ACS Sens 6 (2021) 3093–3101, https://doi.org/10.1021/acssensors.1c01222.
[8] T. Chaibun, J. Puenpa, T. Ngamdee, N. Boonapatcharoen, P. Athamanolap, A. P. O'Mullane, S. Vongpunsawad, Y. Poovorawan, S.Y. Lee, B. Lertanantawong, Rapid electrochemical detection of coronavirus SARS-CoV-2, Nat. Commun. 12 (2021), 802, https://doi.org/10.1038/s41467-021-21121-7.
[9] J. Zhao, Z. Fu, H. Li, Y. Xiong, S. Cai, C. Wang, Y. Chen, N. Han, R. Yang, Magnet-assisted electrochemical immunosensor based on surface-clean Pd-Au nanosheets for sensitive detection of SARS-CoV-2 spike protein, Electrochim. Acta 404 (2022), 139766, https://doi.org/10.1016/j.electacta.2021.139766.
[10] E.D. Nascimento, W.T. Fonseca, T.R. de Oliveira, C.R.S.T.B. de Correia, V.M. Faça, B.P. de Morais, V.C. Silvestrini, H. Pott-Junior, F.R. Teixeira, R.C. Faria, COVID-19 diagnosis by SARS-CoV-2 Spike protein detection in saliva using an ultrasensitive magneto-assay based on disposable electrochemical sensor, Sens. Actuat. B 353 (2022), 131128, https://doi.org/10.1016/j.snb.2021.131128.
[11] M.A. Ehsan, S.A. Khan, A. Rehman, Screen-Printed Graphene/Carbon Electrodes on Paper Substrates as Impedance Sensors for Detection of Coronavirus in Nasopharyngeal Fluid Samples, Diagnostics 11 (2021) 1030, https://doi.org/10.3390/diagnostics11061030.
[12] G.C. Zaccariotto, M.K.L. Silva, G.S. Rocha, I. Cesarino, A novel method for the detection of SARS-CoV-2 based on graphene-impedimetric immunosensor, Materials 14 (2021) 4230, https://doi.org/10.3390/ma14154230.
[13] E.B. Aydın, M. Aydın, M.K. Sezgintürk, Highly selective and sensitive sandwich immunosensor platform modified with MUA-capped GNPs for detection of spike Receptor Binding Domain protein: a precious marker of COVID 19 infection, Sens. Actuat. B 345 (2021), 130355, https://doi.org/10.1016/j.snb.2021.130355.
[14] H.A. Hussein, A. Kandeil, M. Gomaa, R.Mohamed El Nashar, I.M. El-Sherbiny, R.Y. A. Hassan, SARS-CoV-2-impedimetric biosensor: virus-imprinted chips for early and rapid diagnosis, ACS Sens. 6 (2021) 4098–4107, https://doi.org/10.1021/acssensors.1c01614.
[15] M. Wolfe, S. Webb, Y. Chushak, R. Krabacher, Y. Liu, N. Swami, S. Harbaugh, J. Chávez, A high-throughput pipeline for design and selection of peptides targeting the SARS-Cov-2 Spike protein, Sci. Rep. 11 (2021) 21768, https://doi.org/10.1038/s41598-021-01225-2.
[16] M. Amouzadeh Tabrizi, J.P. Fernández-Blázquez, D.M. Medina, P. Acedo, An ultrasensitive molecularly imprinted polymer-based electrochemical sensor for the

determination of SARS-CoV-2-RBD by using macroporous gold screen-printed electrode, Biosens. Bioelectron. 196 (2022), 113729, https://doi.org/10.1016/j.bios.2021.113729.
[17] M. Mehmandoust, Z.P. Gumus, M. Soylak, N. Erk, Electrochemical immunosensor for rapid and highly sensitive detection of SARS-CoV-2 antigen in the nasal sample, Talanta 240 (2022), 123211, https://doi.org/10.1016/j.talanta.2022.123211.
[18] G. Balkourani, A. Brouzgou, M. Archonti, N. Papandrianos, S. Song, P. Tsiakaras, Emerging materials for the electrochemical detection of COVID-19, J. Electroanal. Chem. 893 (2021), 115289, https://doi.org/10.1016/j.jelechem.2021.115289.
[19] M. Adeel, K. Asif, V. Canzonieri, H.R. Barai, M.M. Rahman, S. Daniele, F. Rizzolio, Controlled, partially exfoliated, self-supported functionalized flexible graphitic carbon foil for ultrasensitive detection of SARS-CoV-2 spike protein, Sens. Actuat. B 359 (2022), 131591, https://doi.org/10.1016/j.snb.2022.131591.
[20] S. A. M. Adeel, K. Asif, F. Alshabouna, V. Canzonieri, M.M. Rahman, S.A. Ansari, F. Güder, F. Rizzolio, S. Daniele, Label-free electrochemical aptasensor for the detection of SARS-CoV-2 spike protein based on carbon cloth sputtered gold nanoparticles Biosens. Bioelectron. X 12 (2022), 100256 https://doi.org/10.1016/j.biosx.2022.100256.
[21] M.L. Mujica, A. Tamborelli, A. Castellaro, D. Barcudi, M.D. Rubianes, M. C. Rodríguez, H.A. Saka, J.L. Bocco, P.R. Dalmasso, G.A. Rivas, Impedimetric and amperometric genosensors for the highly sensitive quantification of SARS-CoV-2 nucleic acid using an avidin-functionalized multi-walled carbon nanotubes biocapture platform, Biosens. Bioelectron. X 12 (2022), 100222, https://doi.org/10.1016/j.biosx.2022.100222.
[22] A. Gowri, N.A. Kumar, B.S. Anand, Recent advances in nanomaterials based biosensors for point of care (PoC) diagnosis of COVID-19–a minireview, TrAC Trends Anal. Chem. 137 (2022), 116205, https://doi.org/10.1016/j.trac.2021.116205.
[23] H. Yao, N. Li, Y.-L. Wei, J.-J. Zhu, A H2O2 biosensor based on immobilization of horseradishperoxidase in a gelatine network matrix, Sensors 5 (2005) 277–283, https://doi.org/10.3390/s5040277.
[24] N. Li, M.-H. Xue, H. Yao, J.-J. Zhu, Reagentless biosensor for phenolic compounds based on tyrosinase entrapped within gelatine film, Anal. Bioanal. Chem. 383 (2005) 1127–1132, https://doi.org/10.1007/s00216-005-0115-5.
[25] E. Hamidi-Asl, F. Dardenne, R. Blust, K. de Wael, An improved electrochemical aptasensor for chloramphenicol detection based on aptamer incorporated gelatine, Sensors 15 (2015) 7605–7618, https://doi.org/10.3390/s150407605.
[26] S. Campuzano, M. Pedrero, P. Yáñez-Sedeño, J.M. Pingarrón, Antifouling (Bio) materials for electrochemical (Bio)sensing, Int. J. Mol. Sci. 20 (2019), https://doi.org/10.3390/IJMS20020423.
[27] D.P. Tang, R. Yuan, Y.Q. Chai, X. Zhong, Y. Liu, J.Y. Dai, L.Y. Zhang, Novel potentiometric immunosensor for hepatitis B surface antigen using a gold nanoparticle-based biomolecular immobilization method, Anal. Biochem. 333 (2004) 345–350, https://doi.org/10.1016/j.ab.2004.06.035.
[28] Z. Qiang, R. Yuan, Y. Chai, N. Wang, Y. Zhuo, Y. Zhang, X. Li, A new potentiometric immunosensor for determination of α-fetoprotein based on improved gelatin–silver complex film, Electrochim. Acta 51 (2006) 3763–3768, https://doi.org/10.1016/j.electacta.2005.10.039.
[29] J.v. Staros, R.W. Wright, D.M. Swingle, Enhancement by N-hydroxysulfosuccinimide of water-soluble carbodiimide-mediated coupling reactions, Anal. Biochem. 156 (1986) 220–222, https://doi.org/10.1016/0003-2697(86)90176-4.
[30] A.J. Kuijpers, G.H.M. Engbers, J. Krijgsveld, S.A.J. Zaat, J. Dankert, J. Feijen, Cross-linking and characterisation of gelatin matrices for biomedical applications, J. Biomater. Sci. Polym. Ed. 11 (2000) 225–243, https://doi.org/10.1163/156856200743670.
[31] M. Buch, J. Rishpon, An electrochemical immunosensor for C-reactive protein based on multi-walled carbon nanotube-modified electrodes, Electroanalysis 20 (2008) 2592–2594, https://doi.org/10.1002/elan.200804358.
[32] M.E. Wiseman, C.W. Frank, Antibody adsorption and orientation on hydrophobic surfaces, Langmuir 28 (2012) 1765–1774, https://doi.org/10.1021/la203095p.
[33] N. Carlin, S. Martic-Milne, Anti-tau antibodies based electrochemical sensor for detection of tau protein biomarkers, J. Electrochem. Soc. 165 (2018) G3018–G3025, https://doi.org/10.1149/2.0041812jes.
[34] N.K. Chaki, K. Vijayamohanan, Self-assembled monolayers as a tunable platform for biosensor applications, Biosens. Bioelectron. 17 (2002) 1–12, https://doi.org/10.1016/S0956-5663(01)00277-9.
[35] G. Bacher, S. Pal, L. Kanungo, S. Bhand, A label-free silver wire based impedimetric immunosensor for detection of aflatoxin M1 in milk, Sens. Actuat. B 168 (2012) 223–230, https://doi.org/10.1016/j.snb.2012.04.012.
[36] B. Rezaei, T. Khayamian, N. Majidi, H. Rahmani, Immobilization of specific monoclonal antibody on Au nanoparticles for hGH detection by electrochemical impedance spectroscopy, Biosens. Bioelectron. 25 (2009) 395–399, https://doi.org/10.1016/j.bios.2009.07.026.
[37] A. Makaraviciute, A. Ramanaviciene, Site-directed antibody immobilization techniques for immunosensors, Biosens. Bioelectron. 50 (2013) 460–471, https://doi.org/10.1016/j.bios.2013.06.060.
[38] A. Frutiger, A. Tanno, S. Hwu, R.F. Tiefenauer, J. Voros, N. Nakatsuka, Nonspecific binding—fundamental concepts and consequences for biosensing applications, Chem. Rev. 121 (2021) 8095–8160, https://doi.org/10.1021/acs.chemrev.1c00044.

3.2 Manuscript 2: "Study of V_2CT_x-MXene Based Immunosensor for Sensitive Label-Free Impedimetric Detection of SARS-CoV-2 Spike Protein"

ACS APPLIED MATERIALS & INTERFACES

Open Access
This article is licensed under CC-BY 4.0

www.acsami.org
Research Article

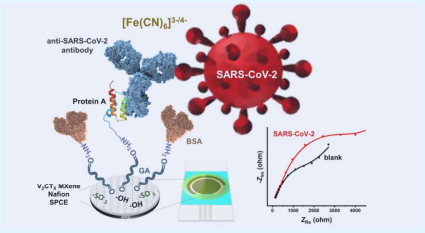
Study of V_2CT_x-MXene Based Immunosensor for Sensitive Label-Free Impedimetric Detection of SARS-CoV-2 Spike Protein

Nikola Tasić, Ivan Konjević, Alnilan Lobato, Dino Metarapi, Matjaž Finšgar, Filipa M. Oliveira, Zděnek Sofer, Rui Gusmão,* Xueji Zhang, and Samo B. Hočevar*

Cite This: https://doi.org/10.1021/acsami.4c04567
Read Online

ACCESS | Metrics & More | Article Recommendations | Supporting Information

ABSTRACT: Rapid and reliable immunosensing is undoubtedly one of the priorities in the efficient management and combat against a pandemic, as society has experienced with the SARS-CoV-2 outbreak; simple and cost-effective sensing strategies are at the forefront of these efforts. In this regard, 2D-layered MXenes hold great potential for electrochemical biosensing due to their attractive physicochemical properties. Herein, we present a V_2CT_x MXene-based sensing layer as an integral part of a label-free immunosensor for sensitive and selective detection of the SARS-CoV-2 spike protein. The sensor was fabricated on a supporting screen-printed carbon electrode using Nafion as an immobilizing agent for MXene and glutaraldehyde, the latter enabling effective binding of protein A for further site-oriented immobilization of anti-SARS-CoV-2 antibodies. A thorough structural analysis of the sensor architecture was carried out, and several key parameters affecting the fabrication and analytical performance of the immunosensor were investigated and optimized. The immunosensor showed excellent electroanalytical performance in combination with an impedimetric approach and exhibited a low detection limit of only 45 fM SARS-CoV-2 spike protein. Its practical applicability was successfully demonstrated by measuring the spike protein in a spiked artificial nasopharyngeal fluid sample.



KEYWORDS: *V_2CT_x MXene, SARS-CoV-2, spike protein, immunosensor, electrochemical, impedimetric*

Downloaded via NATL INST OF CHEMISTRY on June 7, 2024 at 08:23:11 (UTC).
See https://pubs.acs.org/sharingguidelines for options on how to legitimately share published articles.

1. INTRODUCTION

The world has suffered a huge socioeconomic disaster in the context of the SARS-CoV-2 pandemic. With the emergence of potentially more transmissible variants and their possible resistance to commercially available vaccines, societies undoubtedly face the challenge of ensuring adequate prevention and treatment strategies.[1,2] Consequently, the endeavors of the research teams to fabricate and validate viable alternatives to the commercially available RT-PCR (reverse transcription polymerase chain reaction) or widely exploited serological tests are still underway.[3]

It is known that electrochemical immunosensors are capable of detecting trace amounts of biological molecules in a highly selective manner, with a rapid response, by making use of miniaturized devices that nominates them for point-of-need applications.[4−7] The existing literature on electrochemical detection of SARS-CoV-2 has already been reviewed elsewhere, suggesting that significant progress in this field has been made since the pandemic outbreak.[8,9]

The etching process of precursor MAX phases selectively removes the 'A' element layers (usually Al), exposing the MXene layers, which are laminated sheets of transition metal carbides, nitrides, or carbonitrides.[10] MXenes are state-of-the-art 2D-layered nanostructures characterized by high electrical conductivity in both the in-plane and out-of-plane directions. Their large surface-to-volume ratio, high adsorption capacity, and thermal stability make them perfect candidates for smart sensing applications.[11] These applications include the voltammetric detection of gaseous H_2O_2,[12] humidity sensing,[13] trace metals analysis,[14] chemiresistive sensing,[15] and piezoresistive sensors.[16] However, as far as the development of sensing devices for SARS-CoV-2 is concerned, reports on MXenes are still very limited and restricted to biosensors based on field-effect transistors (FET),[17] chemiresistive biosensors based on DNA-functionalized $Ti_3C_2T_x$,[18] luminescent nanoprobes,[19] and electrochemiluminescent sensors.[20]

On the other hand, V_2CT_x MXene has mainly been used in energy storage applications due to the spontaneous intercalation of various cations between its layers.[21] Its potential in

Received: March 19, 2024
Revised: May 13, 2024
Accepted: May 15, 2024

ACS Publications
© XXXX The Authors. Published by American Chemical Society

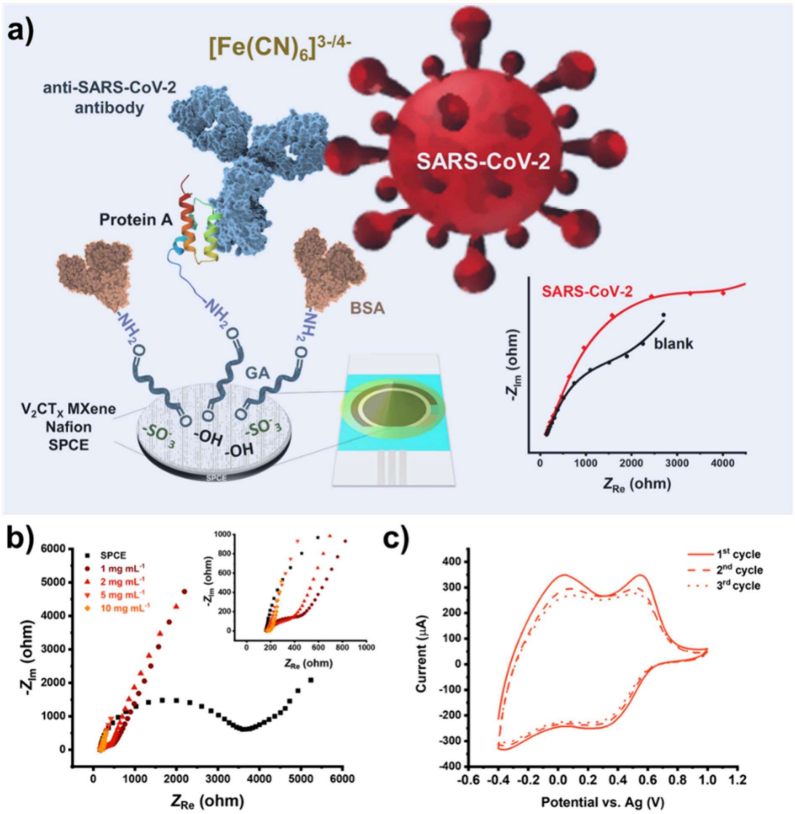


Figure 1. (a) Λ detailed scheme of the immunosensor architecture and its detection principle, (b) Nyquist spectra of the V_2CT_x MXene-modified SPCEs using 1.0 mM $[Fe(CN)_6]^{3-/4-}$ + 0.1 M L^{-1} KCl as a redox probe. The inset shows a magnified high-frequency region of the spectra, and (c) CVs of SPCE modified with 2 mg mL^{-1} V_2CT_x MXene in 0.1 M KCl.

gas sensing has been demonstrated, owing to the surface oxygen functional groups present on the surface of V_2CT_x nanoflakes and rich surface chemistry.[22] Only recently it has been introduced into biosensing as conductive support for the in situ formation of spindle-shaped gold nanoparticles, serving as a metal tag for the antibodies and consequent detection of interleukin 6 from breast cancer cells.[23]

In this work, we developed an impedimetric immunosensor for SARS-CoV-2 spike protein based on V_2CT_x MXene nanomaterial. We used a protocol for the chemical binding of anti-SARS-CoV-2 antibodies with glutaraldehyde (GA) as a cross-linker and protein A, facilitating the subsequent site-oriented binding of the antibody. Several studies were carried out encompassing the modification protocols and critical operational key parameters. Finally, we demonstrated a sensitive and selective detection of spike protein in PBS and nasopharyngeal samples within the time frame of ca. 15 min, making a step forward toward true point-of-need applications.

2. METHODS

2.1. Chemicals. All commercial reagents were of analytical grade and were used without further purification. All aqueous solutions were prepared using ultrapure water with a resistivity of 18.2 MΩ cm at 298 K (Milli-Q, Millipore, Corp., Marlborough, MA). Potassium hexacyanoferrate(III) ($K_3Fe(CN)_6$), Nafion perfluorinated resin solution (5% in a mixture of lower aliphatic alcohols and water), and glutaraldehyde (GA) solution (25% in water) were purchased from Sigma-Aldrich. Sodium azide (NaN_3) and bovine serum albumin (BSA) were purchased from Fluka. Potassium hexacyanoferrate(II) trihydrate ($K_4Fe(CN)_6{\cdot}3H_2O$) was purchased from Riedel de Haen. Potassium chloride (KCl), sodium chloride (NaCl), sodium hydrogen phosphate dihydrate ($Na_2HPO_4{\cdot}2H_2O$), and potassium dihydrogen phosphate (KH_2PO_4) were purchased from Merck. Absolute ethanol (C_2H_5OH) was purchased from Carlo Erba. Protein A (ab71456) and

https://doi.org/10.1021/acsami.4c04567
ACS Appl. Mater. Interfaces XXXX, XXX, XXX−XXX

human monoclonal anti-SARS-CoV-2 spike glycoprotein S1 antibodies (ab286179) were purchased from Abcam. SARS-CoV-2 spike protein (S1 subunit, nCoV-P001) and nucleocapsid protein (protein N, nCoV-P003) were purchased from Bio Bench. HCoV-OC43 spike S1 protein (40607-V08H1), HCoV-HKU1 spike S1 protein (40021-V08H), HCoV-NL63 spike S1 protein (40600-V08H), and HCoV-229E spike protein (40605-V08B), and MERS spike protein (40069-V08B) were all purchased from Sino Biological Europe GmbH, Eschborn, Germany. The artificial saliva was purchased from BioChemazone. The chemicals used in the MAX phase etching were all from Sigma-Aldrich, except when specified otherwise.

2.2. Preparation of Buffer Solutions. Phosphate-buffered saline (PBS, pH = 7.4) was prepared by dissolving 8.00 g of NaCl, 200.0 mg of KCl, 1.81 g of $Na_2HPO_4{\cdot}2H_2O$, and 240.0 mg of KH_2PO_4 in 1.0 L of purified H_2O. When the PBS was used to dilute proteins, 0.001% NaN_3 was added to the solution as a preservative.

2.3. Synthesis and Characterization of V_2CT_x MXene. The synthesis of multilayered V_2CT_x MXene powder involved selectively removing Al from V_2AlC powder. Initially, 5.0 g of V_2AlC MAX phase material sourced from Jinzhou Haixin Metal Materials in China was gradually added to a solution of 250.0 mL of 40.0% hydrofluoric acid (HF). This mixture was continuously stirred for 48 h within a 500 mL capacity Teflon-lined stainless-steel autoclave. Subsequently, the sample was stirred for an additional 48 h in hydrochloric acid (HCl) to a concentration of 6 mol L^{-1}. For the final etching step, the sample was immersed in a mixture of lithium fluoride (LiF, ≥98.5 wt %), 6 mol L^{-1} HCl, and deionized water for 72 h. Following the etching process, the sediment underwent multiple washes with deionized water until the pH of the supernatant reached approximately 6, followed by a wash with absolute ethanol. Finally, the obtained powders were dried in a vacuum for 24 h at a temperature of 60 °C.

2.4. Modification of the Supporting Electrode and Sensor Preparation. The working electrode of the screen-printed carbon electrode (SPCE, DropSens, DRP-110, Metrohm, Herisau, Switzerland, diameter of 4 mm) was first modified with V_2CT_x MXene by drop casting 10 μL of its 2 mg mL^{-1} aqueous solution and left at ca. 35 °C to dry in the closed and light-protected dish. Prior to this, the drop-casting solution was sonicated for 15 min (Elma Transsonic Digital S ultrasound bath, frequency of 40 kHz, 100% applied sonication power at 22−30 °C). In the next step, the working electrode was covered with a Nafion protective/immobilization layer by drop casting 2.2 μL of the 0.0025% Nafion solution in ethanol. After drying at room temperature (23 °C, ca. 1 h), the working electrode was modified with 10 μL of 2.5% GA solution in PBS (pH 7.4) for 2 h at 4 °C, in a light-protected dish. Then the electrode was rinsed carefully by immersing it in purified water for ca. 5 s and dried for ca. 10 s with nitrogen at 0.2 bar. In the following step, the electrode was incubated using 10 μL of 2 μg mL^{-1} protein A solution in PBS (pH 7.4) for 1 h, at room temperature, and then rinsed and dried again in the same way as after the addition of GA. Afterward, the working electrode was incubated with 10 μL of 2 μg mL^{-1} anti-SARS-CoV-2 antibody solution in PBS (pH 7.4) for 30 min. The electrodes were then kept at 4 °C overnight to reach the conformational stability of proteins. The remaining nonspecific binding sites were covered with BSA by exposing the working electrode of the SPCE to 10 μL of 10 μg mL^{-1} BSA solution in PBS for 30 min, at room temperature. Finally, the electrodes were rinsed with purified water and dried with nitrogen to eliminate liquid residues on the surface and were ready for use. When not used, the immunosensors were stored in a closed vessel in the refrigerator at 4 °C. A detailed scheme of the immunosensor architecture and its detection principle is shown in Figure 1a.

2.5. Electrochemical Measurements. All electrochemical measurements, i.e., cyclic voltammetric (CV) and electrochemical impedance spectroscopic (EIS), were performed using a portable PalmSens 4 potentiostat/galvanostat controlled by the PSTrace 5.9 software (PalmSens BV, Netherlands). Electrochemical impedance spectroscopy (EIS, Nyquist plots) measurements were performed in the frequency range of 10^4−10^{-1} Hz at the potential of +0.14 V vs integrated silver quasi-reference electrode at the SPCE, with an amplitude of 5 mV, using 1.0 mM $[Fe(CN)_6]^{3-/4-}$ in 0.1 M KCl as a redox probe. As the analytical signal, the difference between the R_{ct} value extracted from the measurement of the incubated sensor (R_{inc}) and the R_{ct} value of the nonincubated sensor (R_{blank}), i.e., $R_{inc} - R_{blank}$, was used. These values were obtained by fitting the raw impedance data using the equivalent electrical circuit $R_S(R_{MXene}Q_{MXene})([R_{ct}Z_W]C_{dl})$. Herein, R_S corresponds to the solution resistance, C_{dl} is the double-layer capacitance, R_{ct} is the charge transfer resistance of the sensing layer/electrolyte interface, and Z_W is the Warburg element that models the diffusion phenomenon; R_{MXene} and Q_{MXene} correspond to the resistance and the constant phase element of the nonideal capacitance of the underlying V_2CT_x MXene layer, respectively.

2.6. Characterizations. The X-ray photoelectron spectroscopy (XPS) measurements were performed using a Supra+ device (Kratos, Manchester, UK) and an Al K_α excitation source. The binding energy (BE) scale was corrected based on the C−C/C−H peak in the C 1s spectra. High-resolution spectra were acquired at a 90° takeoff angle. Sputtering was performed with a 5 keV Ar_{2000}^+ gas cluster ion beam rastering over 2 by 2 mm. During the depth profiling, spectra were acquired in the center of the sputter crater on a 110-μm spot size (in diameter) at the pass energy of 40 eV. Spectra acquisition and processing were performed using ESCApe 1.5 software (Kratos).

Time-of-flight secondary ion mass spectrometry (ToF-SIMS) measurements were conducted using a M6 device (IONTOF, Munster, Germany) and a 30 keV Bi^+ primary beam (target current of 1.0 pA). Spectra acquisition and processing were performed with SurfaceLab 7.3 software (IONTOF). 3D depth profiles were obtained using 2.5 keV Ar_{1900}^+ gas cluster ion beam rastering over 500 by 500 μm and the analysis of an area of 300 by 300 μm in the middle of the sputter crater. Spectra calibration was performed with the signals at known m/z.

The morphology of the exfoliated materials was observed by Tescan Maia 3 with a field emission gun (Tescan, Czech Republic). The measurements were performed at an acceleration voltage of 20 keV. An SDD detector (X-MaxN 80 TS) from Oxford Instruments (England) was used to obtain the elemental maps and EDX spectra. The materials were sonicated in an aqueous solution for 20 min in an ultrasonic bath (T < 30 °C, 37 Hz, 100%) to guarantee a dispersion of the MXene and drop-cast on a TEM grid (Cu; 200 mesh; Formvar/carbon). The drop-cast samples were dried under a vacuum. Field-emission scanning electron microscopy (FE-SEM) images and the EDX analysis of V_2CT_x MXene deposited onto the SPCEs were obtained with a high-resolution scanning electron microscope (Carl Zeiss SUPRA 35 VP FE-SEM) equipped with an energy-dispersive X-ray spectrometer (Oxford Instruments Inca 400 EDX).

3. RESULTS AND DISCUSSION

3.1. Characterization of V_2CT_x MXene Layer. MXenes were introduced on the electrode surface by a drop-casting technique. It has been shown that a relatively small quantity of (nano)particles needs to be dispersed over the electrode surface to harvest the electrocatalytic potential of MXenes;[24] thus, the concentration of the MXene suspensions in the initial experiments was in the range of 1−10 mg mL^{-1}, corresponding to the final mass concentrations of 80−800 μg cm^{-2} in the deposited layer. In addition to a V_2CT_x MXene layer, we also introduced a highly diluted Nafion coating (0.0025% in absolute ethanol) to immobilize the MXene particles at the electrode surface. The surface of the modified electrodes was first investigated using 3D interferometry, and the corresponding images are presented in Figure S1a−c. With MATLAB-compiled software, we calculated the average thickness of the V_2CT_x MXene coatings using the prerecorded interferograms of the nonmodified and modified SPCEs as the source data. All data sets consisted of approximately 4600 imaging points per circular electrode area. The highest average thickness of the modification coating was observed when using 10 μL of 10 mg

https://doi.org/10.1021/acsami.4c04567
ACS Appl. Mater. Interfaces XXXX, XXX, XXX−XXX

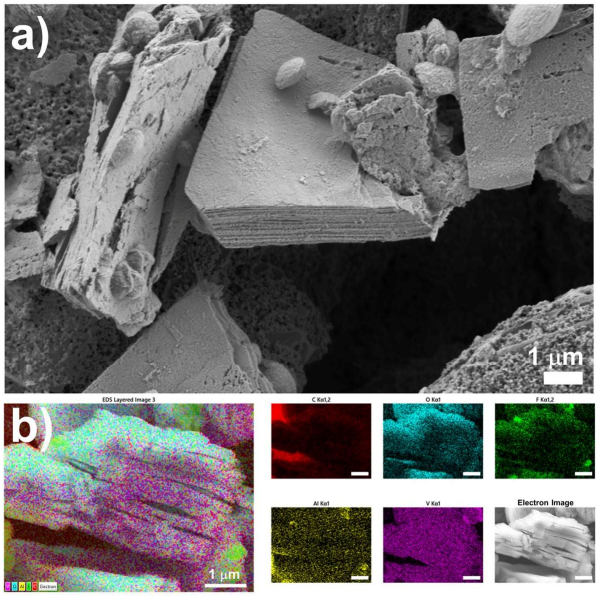


Figure 2. (a) FE-SEM analysis of the synthesized V_2CT_x MXene and (b) EDX analysis of an accordion-like V_2CT_x MXene moiety.

mL^{-1} MXene, i.e., ca. 1.5 μm in height, and significantly lower thicknesses for modifications with more diluted MXene solutions (see Figure S1a). The fluctuation of the thickness within the same sample, commonly present in drop-cast films, was elucidated by observing randomly chosen line sections through the approximate geometrical center of the modified electrode (see Figure S1c). Notably, the same trends in all samples were observed regardless of the chosen line section.

The initial electrochemical study of the V_2CT_x MXene deposits was conducted by EIS analysis in the presence of 1.0 mM $[Fe(CN)_6]^{3-/4-}$ in 0.1 M KCl, and the corresponding Nyquist spectra are shown in Figure 1b. The spectra considerably changed by introducing the modification coatings using 1 and 2 mg mL^{-1} V_2CT_x MXene in the drop-casting solutions compared to a nonmodified SPCE that exhibited a relatively high charge transfer resistance. The EIS spectra changed further with the increasing concentration of the MXene to 5 and 10 mg mL^{-1}, showing a predominant contribution of the diffusion of redox species. When using the last two concentrations of V_2CT_x MXene, a somewhat higher degree of irreproducibility for the impedimetric parameters was observed, which was not the case at lower concentrations of 1 and 2 mg mL^{-1} V_2CT_x MXene (results not shown). This lack of reproducibility was manifested in larger standard deviations of EIS-fitted parameters (>25%) across replicate measurements. Additionally, the introduction of the highest examined MXene concentration of 10 mg mL^{-1} resulted in a certain extent (although low) of undesired material leaching. For this reason, we have decided to use electrodes modified with 2 mg mL^{-1} solution of V_2CT_x MXene in all further studies. In addition, the electrodes modified with 2 mg mL^{-1} solution of V_2CT_x MXene were characterized by CV, and the obtained voltammograms are presented in Figure 1c. Similarly to already investigated titanium MXene, i.e., $Ti_3C_2T_x$, the V_2CT_x MXene is also susceptible to electrooxidation, in this case to the stepwise electrooxidation in the anodic region at ca. +0.1 and +0.6 V, with a decrease and merging of the related peaks with further voltammetric cycles, implying the presence of metal oxide;[25] likewise, a weak reduction signal at ca. +0.3 V still persists after subsequent scans. The matter of the innate MXene oxidation was already addressed in the case of $Ti_3C_2T_x$,[26,27] suggesting that the oxidation results from the anodization of metallic atoms at the defect sites and edges, and the extent of this electrochemical instability is mainly governed by pH of the electrolyte and thickness of the MXene flakes. Although most of the vanadium sites are likely to remain intact by the electrochemical process and do not transform into oxide, from the application perspective, this instability might be a favorable intrinsic property of the MXene-based materials. For example, the electrochemically induced coexistence of different vanadium valence states was successfully implemented for high-performing Zn-ion batteries.[28] More specifically, a nanoscale vanadium oxide (VO_x) coating effectively served for multielectron reactions while the sublayers of V_2CT_x remained structurally intact and formed "so-called" nanochannels with intrinsically high conductivity, creating an overall synergy between the existing structural features. We also characterized the SPCE surfaces modified with the

https://doi.org/10.1021/acsami.4c04567
ACS Appl. Mater. Interfaces XXXX, XXX, XXX−XXX

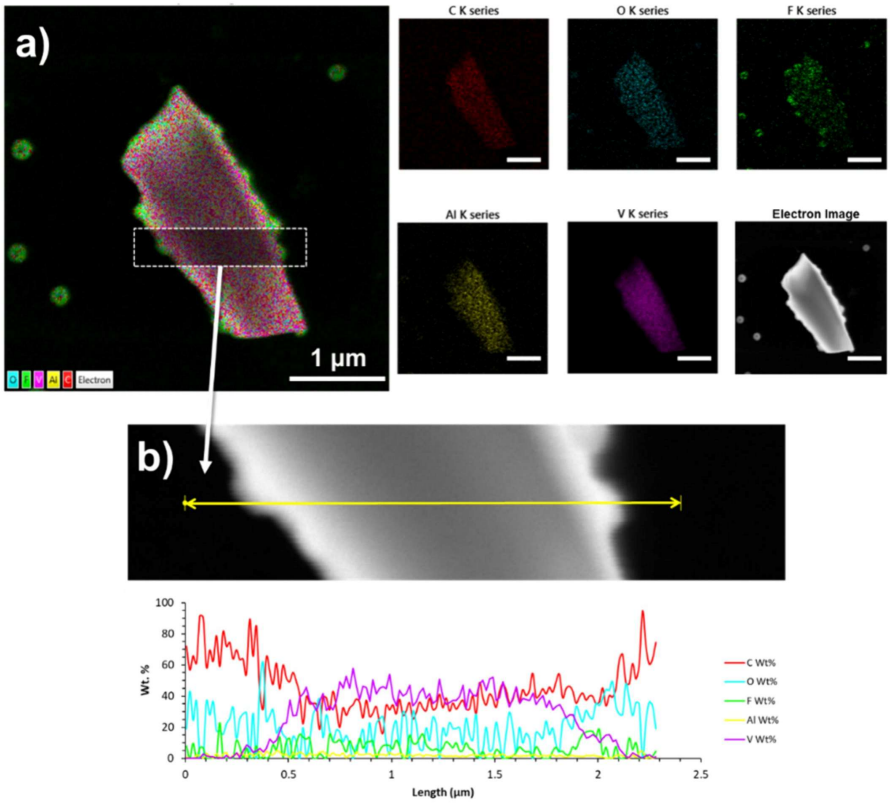


Figure 3. (a) Bright-field mode STEM/EDX analysis of the V_2CT_x MXene flake with EDX layered image, respective map of elements and electron micrograph. (b) Detail of the area used for EDX 1D line scan analysis of the V_2CT_x MXene flake and respective profile of detected elements (wt %). The scale bars represent 1 μm, and the length of the line scan is ca. 2.3 μm.

optimized amount of V_2CT_x MXene, i.e., 2 mg mL^{-1}, after sonication of as-synthesized material, and the corresponding images are shown in Figures S1b, S2a, and S2b. A 15 min sonication of the modification material resulted in almost complete delamination of the V_2CT_x MXene particles, assuring uniform coverage of the electrode surface with the predominant existence of MXene-originating flakes and irregular submicrometer particles.

In addition, we performed a morphology analysis of the synthesized V_2CT_x MXene (Figure 2a). The etching process during MXene synthesis caused the removal of metallic interlayers from the precursor V_2AlC MAX phase, resulting in an irregular, accordion-like morphology of the multilayered V_2CT_x moieties.

As previously reported, the etching process is the most delicate step in MXene synthesis, where the removal of metallic interlayers can lead to the presence of different MXene structures, including MXene clay, intercalated MXene clay, and delaminated clay, accompanied by the degradation of MX layers to carbon and vanadium oxide.[29] In other words, the phase structure of V_2CT_x MXene, its structural integrity, and particle size distribution are strongly dependent on the synthesis of the precursor V_2AlC MAX phase and the subsequent etching protocols. Under the given experimental conditions, we observed the coexistence of several features, which were confirmed by the presence of clay laminated moieties, delaminated clay, and irregular submicron oxide particles decorating the scattered MXene-based particles.

We also carried out an EDX analysis of the material shown in Figure 2b. The vanadium, oxygen, fluorine, and carbon were detected in all sampled areas of the material, corresponding mainly to MXene-based moieties and/or vanadium-based oxides. In addition, low amounts of aluminum impurities were detected, originating from the precursor MAX phase;

https://doi.org/10.1021/acsami.4c04567
ACS Appl. Mater. Interfaces XXXX, XXX, XXX−XXX

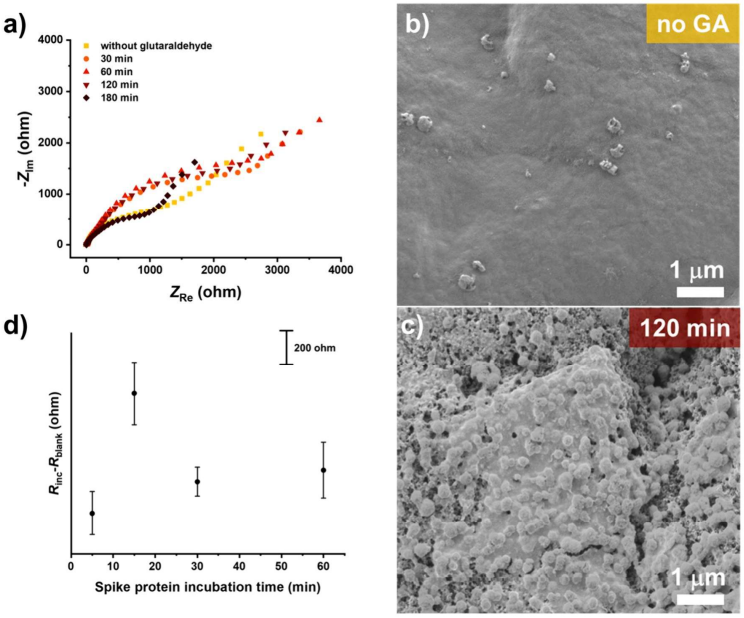


Figure 4. (a) Nyquist spectra of the V_2CT_x/Nafion SPCEs incubated for 1 h with 10 μg mL^{-1} protein A after modification with GA using different modification times, and without GA; surface morphology (FE-SEM) of (b) electrodes incubated with protein A without GA as a cross-linker, followed by incubation with protein A, and (c) electrodes modified with GA for 120 min, followed by incubation with protein A, and (d) effect of the SARS-CoV-2 spike protein incubation time upon the signal. The incubation drop volume was 10 μL, and the concentration of spike protein in PBS (pH = 7.4) was 10^{-5} μg mL^{-1}.

however, their presence is not expected to significantly affect the functionality of the MXene-modified immunosensor. Oxygen was mainly present on the exposed surfaces of the as-synthesized material (see Figures S3a and S3b), and the corresponding elemental compositions are listed in Table S1. This is also supported by the STEM/EDX mapping of elements on individual micrometer scale flakes after the sonication (Figures 3, S4a, S4b). The midsection line scan analysis of the flake indicates that the distribution of O wt % is consistent across, while F wt % seems to be more abundant at the edges of the flakes. The C wt % is overestimated due to the evaporated carbon film characteristic of STEM grids. Moreover, V wt % has a noticeable increase within the region of the flake, up to 58%, while the Al wt % is kept under 7 wt % level. Oxygen can be attributed either to the terminal groups in the remaining MXene nanoflakes or to the presence of vanadium-based oxide nanoparticles. Finally, a significant amount of fluorine was observed, originating from the exfoliation agent, i.e., HF. Its presence is assigned to fluoride or oxyfluoride species and the terminal groups in MXene moieties.

3.2. Sensor Architecture Optimization Studies. GA is widely used as a cross-linking agent due to its high reactivity toward amino, hydroxyl, and carboxyl groups. In this study, GA was used to form a stable cross-link between the V_2CT_x MXene/Nafion layer and protein A, the latter supporting the site-oriented immobilization of the anti-SARS-CoV-2 antibodies. The existing literature contains several articles in which proteins were directly adsorbed onto the composite layer of various nanoparticles with Nafion, such as carbon nanodots,[30,31] carbon nanotubes,[32] or multiwalled carbon nanotubes.[33] However, the adsorption approach inevitably leads to protein denaturation, lower stability, and random alignment, resulting in sensors' poorer analytical performance.[34] Alternatively, the surface can be modified with different cross-linkers, e.g., MPA (3-mercaptopropionic acid) or EDC-NHS (carbodiimide 1-ethyl-3-(3-(dimethylamino)propyl)-carbodiimide and *N*-hydroxysuccinimide),[35,36] prior to the immobilization of antibodies, providing improved stability. Our approach exploits the reactivity of GA toward various end groups at the Nafion-coated V_2CT_x MXene layer, such as sulfonate groups in Nafion and OH terminal groups in V_2CT_x, and its efficacy in immobilizing proteins.[37−39] Nonetheless, GA protocols are designed empirically with respect to the binding protein and require optimization of pH, concentration, temperature, time, etc.[40] Moreover, based on our experience, it is of utmost importance that the GA solutions are always freshly prepared prior to the modification step and that the subsequent reaction with the proteins is carried out instantly;[41] otherwise, cross-linking can be compromised due to the intrinsic instability of GA. Our initial study (not shown)

https://doi.org/10.1021/acsami.4c04567
ACS Appl. Mater. Interfaces XXXX, XXX, XXX−XXX

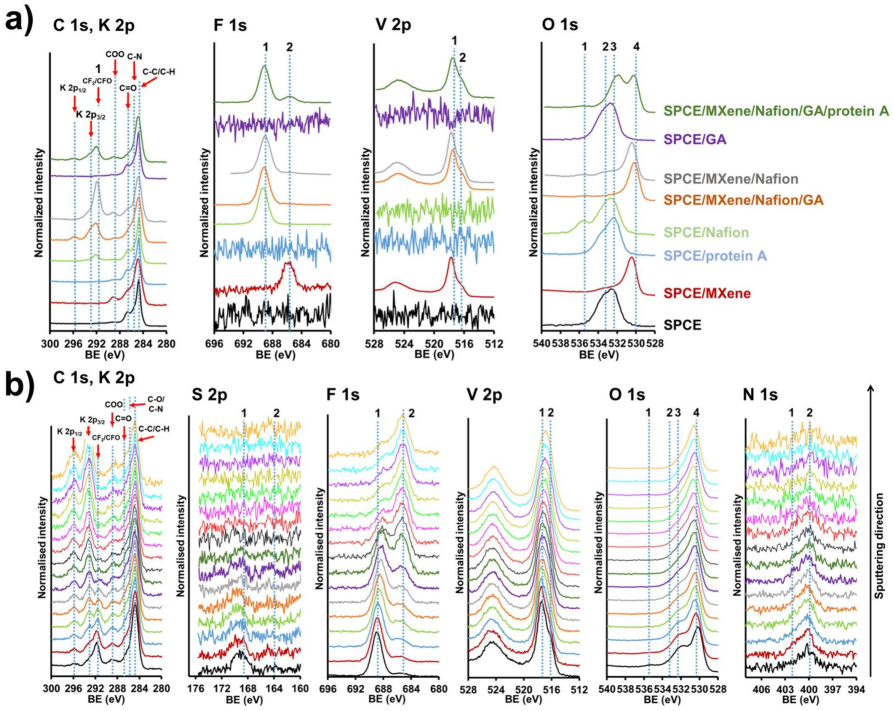


Figure 5. High-resolution XPS spectra (a) of C 1s and K 2p, F 1s, V 2p, and O 1s for different samples, and (b) obtained during depth profiling with the 5 keV Ar_{2000}^{+} of C 1s, S 2p, F 1s, V 2p, O 1s, and N 1s for the SPCE/MXene/Nafion/GA/protein A sample. The lowest spectra presented in part b correspond to the measurements before sputtering.

revealed that the modification with GA should be performed at 2−8 °C and under reduced light conditions to prevent its degradation. On the contrary, modifications performed under ambient and daylight conditions resulted in a nonreproducible electroanalytical behavior.

The efficiency of GA cross-linking was investigated by EIS in the presence of 1.0 mM $[Fe(CN)_6]^{3-/4-}$ in 0.1 M KCl after the GA-modified electrode surface was incubated with 10 μg mL^{-1} protein A for 1 h. The experiments were carried out with different GA modification times ranging from 30 up to 180 min. For comparison, we also included the sample without GA as a cross-linker; Nyquist spectra show a depressed semicircle related to charge transfer resistance at the surfaces of the electrodes and diffusion tails related to the mass transfer of redox species (Figure 4a). The Nyquist spectrum of the electrode surface without GA exhibits a less resistive behavior than surfaces with the GA (up to 120 min), indicating that the direct adsorption approach without a cross-linker leads to lower coverage of the electrode surface with protein A. On the other hand, the extended modification time of 3 h for GA exhibited lower resistance, indicating degradation of GA in water-based solutions.[42] In addition, we examined protein A-modified SPCE by FE-SEM and observed abundant cross-linked spherical protein A clusters of ca. 100 nm at the SPCE surface modified with GA for 120 min (Figure 4c). On the contrary, the electrode modified with protein A without a cross-linking step exhibited a significantly different morphology with fewer and randomly scattered protein A moieties (Figure 4b). Considering the results of this study, further optimization steps were carried out using V_2CT_x/Nafion SPCEs modified in a 2.5% GA solution for 120 min prior to protein A immobilization.

Before testing the analytical performance, we conducted an optimization study considering the incubation time of the SARS-CoV-2 spike protein. The study was aimed at finding the most intense signal, i.e., the difference between the R_{ct} determined from EIS measurements for the sensor incubated at a relatively low spike protein concentration (10^{-5} μg mL^{-1}, i.e., 67 fM) in PBS (R_{inc}) and the R_{blank} (Figure 4d). The investigation of the spike protein incubation time showed that 5 min of incubation was insufficient to obtain a signal 3-times higher than the standard deviation of the R_{blank}, whereas the highest analytical signal was observed after 15 min of incubation. It was observed that for times longer than 15

https://doi.org/10.1021/acsami.4c04567
ACS Appl. Mater. Interfaces XXXX, XXX, XXX−XXX

min, the analytical signal decreased and reached a plateau due to the equilibrium state between the forward and reverse reaction, i.e., binding and dissociation of antigen, respectively. In solution, the antibody−antigen reaction occurs in a few seconds,[43] and to reach complete equilibrium, where a significant proportion of antibodies are bound to the antigen, more time is required, ranging from minutes to hours. On the other hand, the forward reaction between the antibody and antigen at the solid−liquid interfaces is constrained by both the geometry and organization of the receptor molecules.[44] This means the surface reactions are less pronounced and take longer to reach equilibrium than those in solution. To tackle this, the incubation solution was applied via a droplet of 10 μL, which concentrated the antigen in the proximity of the antibody-modified electrode, potentially leading to more effective binding and faster equilibrium. However, since the sharp increase of the forward reaction was observed already after 15 min, characterized by a stable charge transfer signal, we incorporated this incubation time for all further tests. Such a short incubation time fulfills the requirements of rapid on-site applications that match the performance of existing so-called rapid commercial (qualitative only) serological and molecular assays.[45]

The stepwise fabrication of the immunosensor described above was monitored via CV and EIS, as shown in Figure S5. The change of the vanadium- and iron-related signals in cyclic voltammograms performed in 1.0 mM $[Fe(CN)_6]^{3-/4-}$ in 0.1 mol L^{-1} KCl at the V_2CT_x/Nafion SPCEs was used to follow the sequential addition of sensing layers, i.e., GA as a cross-linker, protein A, anti-SARS-CoV-2 antibody, and BSA as a blocking agent (see Figure S5a). As the electrode becomes covered with mostly negatively charged components, the diffusion of negatively charged redox probes toward available electrode sites decreases. At the same time, the thicker sensing layer decreases the ion exchange efficiency needed for the successful operation of the vanadium redox activity. The successful incorporation of proteins, i.e., protein A, antibodies, and BSA, was confirmed by gradual increases in the size of the Nyquist semicircles corresponding to the charge transfer resistance at the sensor interface, indicating sequential changes in the sensor architecture (Figure S5b).

3.3. XPS and ToF-SIMS Studies of the Sensor Architecture. The sensor architecture during the fabrication process was investigated using XPS and ToF-SIMS techniques. Figure 5a shows high-resolution XPS spectra recorded at different fabrication stages. Potassium (K 2p doublet) was detected in some samples but not in all. It may originate from the PBS residues and potassium hexacyanoferrate(II/III) used to characterize the electrochemical behavior of SPCE when obtained and before their modification. The main peak in the C 1s spectra at a BE of 284.8 eV corresponds to the C−C/C−H (present in all samples). The shoulder on the more positive binding energy (BE) side of the main peak represents the C−N signal originating from the amino acids that are the major building blocks of protein A (blue spectrum in Figure 5a). The peak at ca. 292 eV is attributed to the CF_2/CFO in Nafion. This peak is present for the Nafion-contained samples and decreases as more layers are applied to the Nafion, i.e., GA and protein A (see orange and dark green spectra in Figure 5a).[46] On the other hand, MXene-related features corresponding to C═O and O−C═O are located at ca. 287 and 289 eV, respectively.[47] These features are present in all samples containing V_2CT_x MXenes. The F 1s spectra confirm the presence of Nafion and MXene on the electrode surface. The position at the dashed line 1 at ca. 689 eV corresponds to the position of the Nafion-based fluorine signal,[48] while the fluorine terminal groups in MXene are described by a low-intensity peak at more negative BE (at the position of dashed line 2, approximately at 685 eV).[49] As for the vanadium features, a clear doublet of the V 2p spectra is observed. The position of the V $2p_{3/2}$ indicates that vanadium is present in the V(II), V(III), and V(IV).[47,50,51] In addition, the position at the dashed line 1 at ca. 517 eV corresponds to V−O, while the low-intensity shoulder at ca. 516 eV (line 2) can be associated with V−C. Since oxygen is present in all components, the corresponding O 1s spectra provide deeper information about the architecture of our sensor and its stepwise fabrication. Bare SPCE contains two features at ca. 532 and 534 eV, both of which are due to oxygen originating from organic molecules or bound water molecules on the SPCE surface (positions at dashed lines 2 and 3). On the other hand, the signal from oxygen belonging to the sulfonate groups in Nafion develops at ca. 535 eV (dashed line 1), which was observed in the SPCE/Nafion sample and other samples containing Nafion. In the SPCE/MXene sample, the feature at the most negative BE at ca. 530 eV (dashed line 4) belongs to O in V−C−O and/or V−C−OH originating from MXene.[49] In the case of protein A adsorbed on the surface of SPCE, i.e., for the sample SPCE/protein A (O 1s blue spectrum in Figure 5a), the O 1s spectrum is slightly different from that of the bare SPCE, likely due to the contribution of the amino acids, i.e., C═O, C−O, and O−C═O with BE positions at ca. 532 eV. When the SPCE is modified with both MXene and Nafion (O 1s gray spectrum in Figure 5a), the spectrum is dominated by the features belonging to the oxygen in MXene (the same as for red spectrum in Figure 5a), while the oxygen from the sulfonate groups of Nafion from SPCE/MXene/Nafion is present at the same position (O 1s gray spectrum in Figure 5a) as in the SPCE/Nafion sample (O 1s green spectrum in Figure 5a, position at dashed line 1). Finally, an intense feature appears at ca. 532 eV after the addition of protein A, which can be assigned to its oxygen belonging to the hydroxyl, carbonyl, or carboxyl groups of amino acids.

Additional XPS spectra are presented in the Supporting Information. The peak in Al 2p spectra was detected for the sample SPCE/MXene/Nafion/GA/protein A (Figure S6a). As shown above, in the discussion concerning the EDX analysis, about 1 wt % Al is randomly distributed on the surface of the electrode and belongs to the parental MAX phase and/or aluminum (oxo)fluoride particles; the contribution of aluminum in the XPS spectra is incidental with respect to the acquisition site and was observed only in the complete architecture of SPCE/MXene/Nafion/GA/protein A.

As the Al 2p peak was present, it suggests that the remaining sparse Al moieties on the surface are exposed as inactive areas, implying that they do not interact with additional functional layers. Additionally, Cl 2p and Si 2p spectra shown in Figures S6b and S6c belong to SPCEs originating from binders commonly used for the preparation of screen-printing carbon pastes. Therefore, the signals of these two elements were only detected in samples not covered with MXene, where the coating was thinner than the sampling depth of the XPS technique (ca. 5−10 nm), i.e., at the SPCE/GA, SPCE/Nafion, and SPCE/protein A. As expected, the complete sensor architecture has no Cl 2p and Si 2p signals. The N 1s spectra are shown in Figure S6d. The nitrogen signal mainly comes

https://doi.org/10.1021/acsami.4c04567
ACS Appl. Mater. Interfaces XXXX, XXX, XXX−XXX

from the amino groups, with a characteristic feature at about 400 eV, which is most intense for adsorbed protein A in sample SPCE/protein A (blue spectrum in Figure S6d) and in chemically bound protein A to GA (dark green spectrum in Figure S6d). It is also observable in the sample SPCE/MXene at the position of 402 eV (red spectrum in Figure S6d), corresponding to the binder of the screen-printing paste, or hexacyanoferrate from SPCE pretests explained above in the manuscript.

In addition to the XPS analyses for each stage of the sensor fabrication process, Figure 5b demonstrates spectra obtained during depth profiling using a 5 keV Ar_{2000}^+ for the SPCE/MXene/Nafion/GA/protein A sample. The lowest spectra represent the surface of the sample before sputtering, whereas the upper spectra are stacked based on the sputtering progress through the sample. In the C 1s and K 2p spectra, potassium signal was observed, originating from the potassium hexacyanoferrate(II/III) residues during SPCE characterization. The signal K 2p increases with sputtering and has a more significant contribution closer to the surface of the SPCE, as can be seen in the upper spectra (K 2p spectra in Figure 5b). Also, increasing the sputtering time decreases the CF_2/CFO signal as the Nafion is gradually removed from the sensor surface. In the S 2p spectra, the signal has low intensity and is more pronounced closer to the SPCE surface, which can be attributed to the Nafion layer. The analyzed spot size for XPS measurements during depth profiling is smaller, i.e., the diameter of the analyzed area during depth profiling was 110 μm, whereas for the spectra acquisition shown in Figure 5a, a larger area was analyzed, i.e., 300 by 700 μm. Thus, the intensity of species with low surface atomic concentrations is less pronounced during depth profiling. This is most likely why the S 2p signal corresponding to protein A, i.e., from methionine amino acids, was not developed (positioned at dashed line 2). However, the N 1s signal originating from protein A is present (described below). The F 1s spectra shown in Figure 5b reveal a BE shift in the signal representing Nafion (dashed line 1) to the underlying MXene (dashed line 2) as sputtering progresses. The environment of V does not change significantly during sputtering, as seen in the V 2p spectra in Figure 5b; however, it is noticeable that the low BE side of the most intense peak is more pronounced for spectra representing regions closer to the electrode surface, suggesting that the upper part of the MXene layer consists of higher valence V(IV) states. As sputtering progresses, the peak corresponding to O in inorganic species, i.e., V−C−O bond, becomes more intense (position on dashed line 4), and the high BE features of O in organic species associated with protein A become less intense with sputtering (positions at dashed lines 1−3), as the organic species are gradually removed during the sputtering process. Finally, as expected, the signal for N, originating from protein A (in particular from amino groups), is more intense at the topmost position (lower N 1s spectra) and decreases during the sputtering procedure. The depth profiles (surface atomic concentration vs sputtering time) of the main species for the SPCE/MXene/Nafion/GA/protein A sample are shown in Figure S7.

The ToF-SIMS technique was used to determine the spatial distribution of the constituents within our sensor architecture before introducing the antibody. 3D ToF-SIMS profiles were measured in positive (Figure 6) and negative (Figure S8) polarity. VO^+ or VO_2^- signals were used to represent V_2CT_x MXene; CF^+ and CF_3^- signals were employed to determine

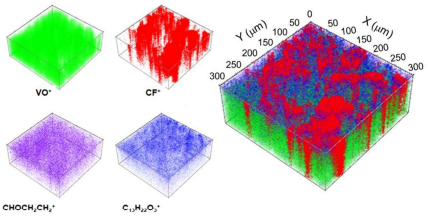


Figure 6. 3D ToF-SIMS images showing the distribution of main constituents of sensor architecture. The signal representing V_2CT_x MXene is shown in green, Nafion in red, GA in violet, and protein A in blue.

the spatial distribution of Nafion ($C_7HF_{13}O_5S{\cdot}C_2F_4$); $CHOCH_2CH_2^+$ signal represents a fragment ion from GA ($C_5H_8O_2$); protein A was characterized by $C_{13}H_{22}O_3^+$ and $C_3HO_3^-$ fragments. The corresponding MXene signals, i.e., both positive (VO^+) in Figure 6 and negative (VO_2^-) in Figure S8, are evenly distributed in the observed region, which is in agreement with the presented 3D profilometry, microscopy analysis, and the elemental XPS depth profiling. The Nafion membrane, which serves to immobilize the particles, appears to be evenly distributed when the contributions of the negative CF^- moieties are taken into account (Figure S8). The contribution of GA is clearly visible and is based on the coherent $CHOCH_2CH_2^+$ signal; moreover, GA forms visibly homogeneous cross-linking support for the upstream protein A molecules. The latter are characterized by a signal deriving from high carbon, hydrogen, and oxygen moiety $C_{13}H_{22}O_3^+$. Similar moieties have already been used for protein identification by the means of ToF-SIMS.[52] The observed distribution agrees well with the results of the FE-SEM analysis, which showed protein A clusters on the top of the modified electrode that typically form in the presence of the GA cross-linker.

3.4. Analytical Performance of the Sensor. Due to the well-known intrinsic irreproducibility, the SPCEs were first subjected to the square-wave voltammetric characterization in 1.0 mmol L^{-1} $[Fe(CN)_6]^{3-/4-}$ in 0.1 mol L^{-1} KCl, and only those with the peak current falling into the range of 50−60 μA were used for further modifications to prepare immunosensors; this voltammetric technique offers improved sensitivity versus cyclic voltammetry, particularly for electrochemically reversible redox systems. The electroanalytical performance of the V_2CT_x MXene-based immunosensor was investigated by increasing the concentration of spike protein in the broad range of 10^{-5} μg mL^{-1} − 0.1 μg mL^{-1} (Figures 7a and 7b). The immunosensor revealed a linear $R_{inc} - R_{blank}$ response (r^2 = 0.99) in the examined concentration range in combination with a short incubation time of only 15 min. Using the 3σ criteria, a very low limit of detection of 45 fM was obtained. In addition, the intraday reproducibility calculated as the relative standard deviations of 8% and 9% were observed for nonincubated sensors and sensors incubated with 10^{-5} μg mL^{-1} of spike protein, respectively.

We tested the immunosensor in the presence of a model interferent SARS-CoV-2 nucleocapsid protein, also known as protein N, at three different concentrations, i.e., 10^{-5}, 10^{-3}, and 10^{-1} μg mL^{-1}. Surprisingly, negligible changes in the R_{ct}

https://doi.org/10.1021/acsami.4c04567
ACS Appl. Mater. Interfaces XXXX, XXX, XXX−XXX

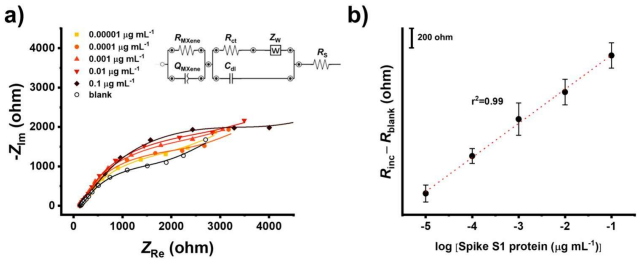


Figure 7. (a) EIS response for increasing concentrations of spike protein in PBS (pH = 7.4, six replicates) and (b) the corresponding calibration curve of the fully optimized sensor. The obtained spectra were fitted using the equivalent circuit shown in the inset of part a and explained in Methods.

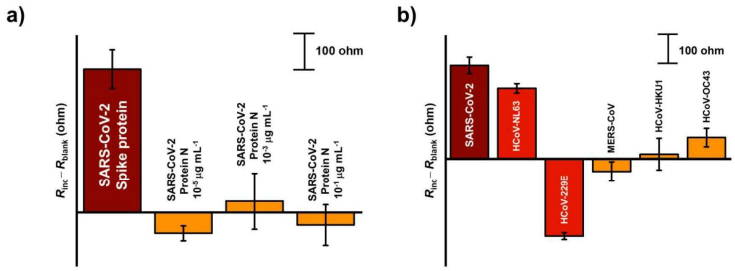


Figure 8. (a) EIS signals for three different concentrations of protein N and 10^{-5} μg mL^{-1} spike protein (pH = 7.4, three replicates) and (b) EIS signals obtained for equal concentration (10^{-3} μg mL^{-1}) of different coronaviruses, i.e., SARS-CoV-2, HCoV-NL63, HCoV-229E, MERS-CoV, HCoV-HKU1, and HCoV-OC43.

were observed upon incubation for all three investigated protein N concentrations (Figure 8a). The R_{ct} values were in the range of a blank signal and significantly lower compared to the signal obtained for a low concentration of the target spike protein, indicating a favorable selectivity of the newly developed immunosensor.

To thoroughly investigate the potential of our sensor, we also performed a selectivity study including spike proteins of several human coronaviruses of similar structures to SARS-CoV-2, i.e., HCoV-OC43, HCoV-HKU1, HCoV-NL63, HCoV-229E, and MERS-CoV. All of these viruses commonly cause mild to moderate upper respiratory tract illnesses in humans. Their symptoms can overlap with the symptoms caused by SARS-CoV-2. The results of this study are presented in Figure 8b. It can be noted that MERS-CoV, HCoV-HKU1, and HCoV-OC43 did not cause any significant interference, with observed selectivity factors of −13%, +5%, and +23%, respectively. The selectivity factors were calculated as a ratio between the EIS signal of interferent and SARS-CoV-2. On the other hand, HCoV-NL63 showed a somewhat higher signal contribution with a selectivity factor of +75%. Interestingly, a substantial decrease in the analytical signal occurred upon incubation with HCoV-229E with a selectivity factor of −81%. Considering the latter results, it is rather challenging to completely interpret the observed phenomenon; the higher molecular weight of the HCoV-229E spike protein compared to other investigated candidates, as well as its positive net charge, may explain the unexpectedly low signal. On the contrary, structural similarities to SARS-CoV-2 are notably the most pronounced in the case of HCoV-NL63, resulting in the highest positive selectivity factor observed.

Finally, we carried out measurements in the artificial nasopharyngeal fluid (ANF) spiked with 100 μg mL^{-1} spike protein. Nasopharyngeal fluid, being rich in diverse components, such as mucus, proteins, protein mimics, salts, ions, and cells, can strongly influence the immunosensor's operation. Thus, the spiked nasopharyngeal samples present a big challenge for the electrochemical immunosensing platforms. To attenuate the matrix effect of the nasopharyngeal fluid, we implemented dilutions of the sample with PBS (pH = 7.4), i.e., 10, 20, and 50 times. A linear signal for three consecutive dilutions (r^2 = 0.99, n = 3) was obtained, along with a sensitivity of 51.22 ± 6.26 Ω·mL·μg^{-1}, as shown in Figure S9a,b. Notably, likely due to the matrix effect, the shape of the obtained EIS spectra was affected so that the contribution from the MXene-modification layer, characterized by determined R_{ct} when incubated with the spike protein samples in PBS, was not observed and was excluded from the corresponding equivalent circuit; this phenomenon is attributed to the sluggish ion diffusion. Thus, to process the obtained data, an even simpler Randles-type circuit was used, i.e., $R_S([R_{ct}Z_W]Q_{dl})$. The obtained values for the analytical signal, i.e., $R_{inc} - R_{blank}$, were lower in comparison to the values obtained for the samples in PBS, accounting for the idle kinetics of the

https://doi.org/10.1021/acsami.4c04567
ACS Appl. Mater. Interfaces XXXX, XXX, XXX−XXX

antigen−antibody reactions in a complex matrix within the incubation time frame of 15 min. Under the given conditions, the reactivity of SARS-CoV-2 spike protein toward antibodies immobilized on the surface can be reduced due to interactions with other glycoproteins or entrapment by macrophages and dendritic cells of ANF. Although the accuracy of the measurements was slightly compromised, the sensor exhibited high linearity and good sensitivity, demonstrating its potential for reliable detection of SARS-CoV-2 spike protein. Furthermore, due to potential pH fluctuations in real samples, the operation of the immunosensor was tested in samples with different pH values, i.e., 5, 6, 7.5, and 8. Interestingly, the experiments revealed the highest response ($R_{inc} - R_{blank}$) in the sample with pH 7.5, and the samples with pH 5 and 6 showed almost the same responses which were ca. 25% lower than that at pH 7.5, whereas the measurement in the sample with pH 8 exhibited a signal ca. 14% lower compared to the signal recorded at pH 7.5 (Figure S10).

Such electroanalytical performances can be attributed to favorable interlayer synergies of the presented immunosensor's architecture. This includes, apart from the inherent sensitivity of the EIS technique, a stable and (electro)catalytically active layer of V_2CT_x MXene flakes immobilized in Nafion film, which simultaneously serves as an effective support for glutaraldehyde deposition, the latter enabling an efficient binding of protein A for further site-oriented covalent immobilization of anti-SARS-CoV-2 antibodies. At the same time, the application of BSA as a blocking agent against unspecific binding events still allowed a very sensitive functioning of the immunosensor. In comparison with other similar impedimetric immunosensors for the SARS-CoV-2 antigen listed in Table S2, we can conclude that our immunosensor compares favorably or even surpasses them, considering the overall sensing performances.[53−61]

4. CONCLUSIONS

An immunosensor based on V_2CT_x MXene exhibited excellent sensitivity and satisfactory selectivity toward SARS-CoV-2 spike protein in combination with electrochemical impedance spectroscopy. The electrocatalytic MXene was immobilized on the supporting SPCE surface using a thin Nafion layer additionally functionalized with the GA-cross-linked protein A. The optimized immunosensor architecture showed a favorable electrocatalytic capability of V_2CT_x MXene, enabling sensitive, label-free, and rapid impedimetric detection of the SARS-CoV-2 spike protein with a detection limit as low as 45 fM, in combination with only 15 min incubation. The practical applicability of the immunosensor was demonstrated through the successful detection of SARS-CoV-2 spike protein in artificial nasopharyngeal fluid. Its electroanalytical performance indicates a great potential of the MXene-based interfaces for their broader immunosensing applications and suggests another direction toward developing rapid and point-of-need immunoassays.

■ ASSOCIATED CONTENT

Supporting Information

The Supporting Information is available free of charge at https://pubs.acs.org/doi/10.1021/acsami.4c04567.

3D profilometry analysis of coatings with different V_2CT_x MXene loadings. FE-SEM images of V_2CT_x MXene deposited on the SPCE. FE-SEM/EDX analysis of the as-synthesized V_2CT_x MXene and elemental composition. Bright-field mode STEM/EDX analysis of the V_2CT_x MXene flake with EDX layered image. Step-by-step fabrication of the immunosensor monitored by EIS and CV. High-resolution XPS spectra of different samples. XPS depth profiles for different elements. 3D negative ion ToF-SIMS images of sensing architecture. The calibration curve of the fully optimized immunosensor in ANF. The effect of pH of the ANF on the signal of immunosensor. Comparison of impedimetric immunosensors for the detection of SARS-CoV-2 spike protein (PDF)

■ AUTHOR INFORMATION

Corresponding Authors

Samo B. Hočevar − *Department of Analytical Chemistry, National Institute of Chemistry, 1000 Ljubljana, Slovenia;* orcid.org/0000-0003-2980-4822; Email: samo.hocevar@ki.si

Rui Gusmão − *Department of Inorganic Chemistry, University of Chemistry and Technology Prague, 166 28 Praha 6-Dejvice, Czech Republic;* orcid.org/0000-0001-6358-7601; Email: rui.gusmao@vscht.cz

Authors

Nikola Tasić − *Department of Analytical Chemistry, National Institute of Chemistry, 1000 Ljubljana, Slovenia;* orcid.org/0000-0002-0582-2252

Ivan Konjević − *Department of Analytical Chemistry, National Institute of Chemistry, 1000 Ljubljana, Slovenia; Faculty of Chemistry and Chemical Technology, University of Ljubljana, 1000 Ljubljana, Slovenia*

Alnilan Lobato − *Department of Analytical Chemistry, National Institute of Chemistry, 1000 Ljubljana, Slovenia; International Postgraduate School Jožef Štefan, 1000 Ljubljana, Slovenia;* orcid.org/0000-0002-4936-5647

Dino Metarapi − *Department of Analytical Chemistry, National Institute of Chemistry, 1000 Ljubljana, Slovenia*

Matjaž Finšgar − *Faculty of Chemistry and Chemical Engineering, University of Maribor, 2000 Maribor, Slovenia;* orcid.org/0000-0002-8302-9284

Filipa M. Oliveira − *Department of Inorganic Chemistry, University of Chemistry and Technology Prague, 166 28 Praha 6-Dejvice, Czech Republic;* orcid.org/0000-0001-7268-3144

Zdeněk Sofer − *Department of Inorganic Chemistry, University of Chemistry and Technology Prague, 166 28 Praha 6-Dejvice, Czech Republic;* orcid.org/0000-0002-1391-4448

Xueji Zhang − *School of Biomedical Engineering, Shenzhen University Health Science Center, Shenzhen S18054 Guangdong, P.R. China;* orcid.org/0000-0002-0035-3821

Complete contact information is available at: https://pubs.acs.org/10.1021/acsami.4c04567

Author Contributions

Nikola Tasić: Conceptualization, investigation, visualization, formal analysis, data evaluation, methodology, writing - original draft, writing - review and editing. Ivan Konjević: Investigation, formal analysis, data evaluation, methodology. Alnilan Lobato: Investigation, formal analysis. Dino Metarapi: Methodology,

https://doi.org/10.1021/acsami.4c04567
ACS Appl. Mater. Interfaces XXXX, XXX, XXX−XXX

visualization, software, formal analysis, data evaluation. Matjaž Finšgar: Investigation, visualization, formal analysis, data evaluation, methodology, writing - original draft. Filipa M. Oliveira: Investigation, formal analysis. Zděnek Sofer: Supervision, funding acquisition. Rui Gusmão: Methodology, supervision, writing - original draft. Xueji Zhang: Formal analysis, conceptualization, supervision. Samo B. Hočevar: Conceptualization, methodology, supervision, funding acquisition, writing - original draft, writing - review and editing.

Notes

The authors declare no competing financial interest.

■ ACKNOWLEDGMENTS

This research received funding from the Slovenian Research Agency (research programs P1-0034, P2-0118, and research project J1-4416) and the Slovenian Research Agency's Young Researchers Program (grant agreement no. 56119). The project is cofinanced by the Republic of Slovenia, the Ministry of Higher Education, Science and Innovation, and the European Union under the European Regional Development Fund. The authors acknowledge funding from the ERC-CZ program (project LL2101) from the Ministry of Education Youth and Sports (MEYS), large infrastructure from project Advanced Functional Nanorobots (reg. no. CZ.02.1.01/0.0/0.0/15_003/0000444 financed by the EFRR), and Dr. Arvind Kumar Gupta from the National Institute of Chemistry (Ljubljana, Slovenia) for the acquisition of MERS spike protein.

■ REFERENCES

(1) Delardas, O.; Kechagias, K. S.; Pontikos, P. N.; Giannos, P. Socio-Economic Impacts and Challenges of the Coronavirus Pandemic (COVID-19): An Updated Review. *Sustainability* **2022**, *14* (15), 9699.

(2) Coccia, M. Pandemic prevention: lessons from COVID-19. *Encyclopedia* **2021**, *1* (2), 433−444.

(3) Artik, Y.; Coşğun, A. B.; Cesur, N. P.; Hızel, N.; Uyar, Y.; Sur, H.; Ayan, A. Comparison of COVID-19 laboratory diagnosis by commercial kits: Effectivity of RT-PCR to the RT-LAMP. *J. Med. Virol.* **2022**, *94* (5), 1998−2007.

(4) Ricci, F.; Adornetto, G.; Palleschi, G. A review of experimental aspects of electrochemical immunosensors. *Electrochim. Acta* **2012**, *84*, 74−83.

(5) Wen, W.; Yan, X.; Zhu, C.; Du, D.; Lin, Y. Recent advances in electrochemical immunosensors. *Anal. chem.* **2017**, *89* (1), 138−156.

(6) Mollarasouli, F.; Kurbanoglu, S.; Ozkan, S. A. The role of electrochemical immunosensors in clinical analysis. *Biosensors* **2019**, *9* (3), 86.

(7) Felix, F. S.; Angnes, L. Electrochemical immunosensors−a powerful tool for analytical applications. *Biosens. Bioelectron.* **2018**, *102*, 470−478.

(8) Kotru, S.; Klimuntowski, M.; Ridha, H.; Uddin, Z.; Askhar, A. A.; Singh, G.; Howlader, M. M. Electrochemical sensing: A prognostic tool in the fight against COVID-19. *TrAC Trends Anal. Chem.* **2021**, *136*, No. 116198.

(9) Kumar, N.; Shetti, N. P.; Jagannath, S.; Aminabhavi, T. M. Electrochemical sensors for the detection of SARS-CoV-2 virus. *Chem. Eng. J.* **2022**, *430*, No. 132966.

(10) Haemers, J.; Gusmão, R.; Sofer, Z. Synthesis protocols of the most common layered carbide and nitride MAX phases. *Small Methods* **2020**, *4* (3), 1900780.

(11) Ho, D. H.; Choi, Y. Y.; Jo, S. B.; Myoung, J. M.; Cho, J. H. Sensing with MXenes: progress and prospects. *Adv. Matter.* **2021**, *33* (47), 2005846.

(12) Isailović, J.; Oberlintner, A.; Novak, U.; Finšgar, M.; Oliveira, F. M.; Paštika, J.; Sofer, Z.; Gusmao, R.; Hočevar, S. B.; Tasić, N. Study of Chitosan-Stabilized $Ti_3C_2T_x$ MXene for Ultrasensitive and Interference-Free Detection of Gaseous H_2O_2. *ACS Appl. Mater. Interfaces.* **2023**, *15* (26), 31643−31651.

(13) An, H.; Habib, T.; Shah, S.; Gao, H.; Patel, A.; Echols, I.; Zhao, X.; Radovic, M.; Lutkenhaus, J. L.; Green, M. J. Water sorption in MXene/polyelectrolyte multilayers for ultrafast humidity sensing. *ACS Appl. Nano Mater.* **2019**, *2* (2), 948−955.

(14) Zhu, X.; Liu, B.; Hou, H.; Huang, Z.; Zeinu, K. M.; Huang, L.; Yuan, X.; Guo, D.; Hu, J.; Yang, J. Alkaline intercalation of Ti_3C_2 MXene for simultaneous electrochemical detection of Cd (II), Pb (II), Cu (II) and Hg (II). *Electrochim. Acta* **2017**, *248*, 46−57.

(15) Chaudhary, V.; Ashraf, N.; Khalid, M.; Walvekar, R.; Yang, Y.; Kaushik, A.; Mishra, Y. K. Emergence of MXene−polymer hybrid nanocomposites as high-performance next-generation chemiresistors for efficient air quality monitoring. *Adv. Funct. Mater.* **2022**, *32* (33), 2112913.

(16) Li, Y.; Huang, S.; Peng, S.; Jia, H.; Pang, J.; Ibarlucea, B.; Hou, C.; Cao, Y.; Zhou, W.; Liu, H.; Cuniberti, G. Toward Smart Sensing by MXene. *Small* **2023**, *19*, 2206126.

(17) Seo, G.; Lee, G.; Kim, M. J.; Baek, S. H.; Choi, M.; Ku, K. B.; Lee, C. S.; Jun, S.; Park, D.; Kim, H. G.; Kim, S. J.; Lee, J. O.; Kim, B. T.; Park, E. C.; Kim, S. I. Rapid detection of COVID-19 causative virus (SARS-CoV-2) in human nasopharyngeal swab specimens using field-effect transistor-based biosensor. *ACS Nano* **2020**, *14* (4), 5135−5142.

(18) Chen, W. Y.; Lin, H.; Barui, A. K.; Gomez, A. M. U.; Wendt, M. K.; Stanciu, L. A. DNA-Functionalized $Ti_3C_2T_x$ MXenes for selective and rapid detection of SARS-CoV-2 nucleocapsid gene. *ACS Appl. Nano Mater.* **2022**, *5* (2), 1902−1910.

(19) Song, M.; Ma, Y.; Li, L.; Wong, M. C.; Wang, P.; Chen, J.; Chen, H.; Wang, F.; Hao, J. Multiplexed detection of SARS-CoV-2 based on upconversion luminescence nanoprobe/MXene biosensing platform for COVID-19 point-of-care diagnostics. *Mater. Des.* **2022**, *223*, No. 111249.

(20) Zhang, K.; Fan, Z.; Huang, Y.; Ding, Y.; Xie, M. A strategy combining 3D-DNA Walker and CRISPR-Cas12a trans-cleavage activity applied to MXene based electrochemiluminescent sensor for SARS-CoV-2 RdRp gene detection. *Talanta* **2022**, *236*, No. 122868.

(21) Dall'Agnese, Y.; Taberna, P. L.; Gogotsi, Y.; Simon, P. Two-dimensional vanadium carbide (MXene) as positive electrode for sodium-ion capacitors. *J. Phys. Chem. Lett.* **2015**, *6* (12), 2305−2309.

(22) Lee, E.; VahidMohammadi, A.; Yoon, Y. S.; Beidaghi, M.; Kim, D. J. Two-dimensional vanadium carbide MXene for gas sensors with ultrahigh sensitivity toward nonpolar gases. *ACS Sens.* **2019**, *4* (6), 1603−1611.

(23) Vessella, T.; Zhang, H.; Zhou, Z.; Cui, F.; Zhou, H. S. In-situ synthesized V_2CT_x MXene-based immune tag for the electrochemical detection of Interleukin 6 (IL-6) from breast cancer cells. *Biosens. Bioelectron.* **2023**, *237*, No. 115512.

(24) Kalambate, P. K.; Gadhari, N. S.; Li, X.; Rao, Z.; Navale, S. T.; Shen, Y.; Patil, V. R.; Huang, Y. Recent advances in MXene−based electrochemical sensors and biosensors. *TrAC Trends Anal. Chem.* **2019**, *120*, No. 115643.

(25) Mousavi, M.; Khorrami, G. H.; Kompany, A.; Yazdi, S. T. Structural, optical and electrochemical properties of F-doped vanadium oxide transparent semiconducting thin films. *Appl. Phys. A: Mater. Sci. Process.* **2017**, *123*, 1−6.

(26) Nayak, P.; Jiang, Q.; Mohanraman, R.; Anjum, D.; Hedhili, M. N.; Alshareef, H. N. Inherent electrochemistry and charge transfer properties of few-layered two-dimensional $Ti_3C_2T_x$ MXene. *Nanoscale* **2018**, *10* (36), 17030−17037.

(27) Nayak, P.; Yang, M.; Wang, Z.; Li, X.; Miao, R.; Compton, R. G. Single-entity $Ti_3C_2T_x$ MXene electro-oxidation. *Appl. Mater. Today.* **2022**, *26*, No. 101335.

(28) Liu, Y.; Jiang, Y.; Hu, Z.; Peng, J.; Lai, W.; Wu, D.; Zuo, S.; Zhang, J.; Chen, B.; Dai, Z.; Yang, Y.; Huang, Y.; Zhang, W.; Zhao, W.; Zhang, W.; Wang, L.; Chou, S. In-situ electrochemically activated surface vanadium valence in V_2C MXene to achieve high capacity and

https://doi.org/10.1021/acsami.4c04567
ACS Appl. Mater. Interfaces XXXX, XXX, XXX−XXX

superior rate performance for Zn-ion batteries. *Adv. Funct. Mater.* **2021**, *31* (8), 2008033.
(29) Kotasthane, V.; Holta, D. E.; Zhao, X.; Lutkenhaus, J. L.; Green, M. J.; Radovic, M. Core−shell mechanism of etching V_2AlC MAX phase to V_2CT_z MXenes. *J. Mater. Res.* **2023**, *38* (6), 1527−1542.
(30) Chen, M.; Zhao, C.; Chen, W.; Weng, S.; Liu, A.; Liu, Q.; Zheng, Z.; Lin, J.; Lin, X. Sensitive electrochemical immunoassay of metallothionein-3 based on $K_3[Fe(CN)_6]$ as a redox-active signal and c-dots/nafion film for antibody immobilization. *Analyst* **2013**, *138* (24), 7341−7346.
(31) Dai, H.; Yang, C.; Tong, Y.; Xu, G.; Ma, X.; Lin, Y.; Chen, G. Label-free electrochemiluminescent immunosensor for α-fetoprotein: performance of Nafion−carbon nanodots nanocomposite films as antibody carriers. *Chem. Commun.* **2012**, *48* (25), 3055−3057.
(32) Zhang, X.; Shen, Y.; Shen, G.; Wang, S. The fabrication of a label-free electrochemical immunosensor using Nafion/carbon nanotubes/charged pyridinecarboxaldehyde composite film. *Anal. Biochem.* **2016**, *504*, 14−19.
(33) Chen, S.; Yuan, R.; Chai, Y.; Min, L.; Li, W.; Xu, Y. Electrochemical sensing platform based on tris (2, 2′-bipyridyl) cobalt (III) and multiwall carbon nanotubes−Nafion composite for immunoassay of carcinoma antigen-125. *Electrochim. Acta* **2009**, *54* (28), 7242−7247.
(34) Makaraviciute, A.; Ramanaviciene, A. Site-directed antibody immobilization techniques for immunosensors. *Biosens. Bioelectron.* **2013**, *50*, 460−471.
(35) Kumar, S.; Tripathy, S.; Singh, O. K.; Singh, S. G. Cerium oxide nanofiber based electroanalytical sensor for TNF-α detection: Improved interfacial stability with Nafion. *Bioelectrochem.* **2021**, *138*, No. 107725.
(36) Liu, Y.; Zhao, Y.; Zhu, Z.; Xing, Z.; Ma, H.; Wei, Q. Ultrasensitive immunosensor for prostate specific antigen using biomimetic polydopamine nanospheres as an electrochemiluminescence superquencher and antibody carriers. *Anal. Chim. Acta* **2017**, *963*, 17−23.
(37) ElKaoutit, M.; Naranjo-Rodriguez, I.; Dominguez, M.; Hidalgo-Hidalgo-de-Cisneros, J. L. Bio-functionalization of electro-synthesized polypyrrole surface by heme enzyme using a mixture of Nafion and glutaraldehyde as synergetic immobilization matrix: Conformational characterization and electrocatalytic studies. *Appl. Surf. Sci.* **2011**, *257* (24), 10926−10935.
(38) Wang, X.; Dzyadevych, S. V.; Chovelon, J. M.; Renault, N. J.; Chen, L.; Xia, S.; Zhao, J. Development of a conductometric nitrate biosensor based on Methyl viologen/Nafion® composite film. *Electrochem. commun.* **2006**, *8* (2), 201−205.
(39) Migneault, I.; Dartiguenave, C.; Bertrand, M. J.; Waldron, K. C. Glutaraldehyde: behavior in aqueous solution, reaction with proteins, and application to enzyme crosslinking. *Biotechniques* **2004**, *37* (5), 790−802.
(40) Coetzee, J.; Van der Merwe, C. F. Some characteristics of the buffer vehicle in glutaraldehyde-based fixatives. *J. Microsc.* **1987**, *146* (2), 143−155.
(41) Romih, T.; Tasić, N.; Bibič, L.; Beltram, A.; Fazarinc, I.; Benčina, M.; Jerala, R.; Hočevar, S. B. RBD-Modified Polyaniline-Based Label-Free Immunosensor for Sensitive Impedimetric Detection of Anti-SARS-CoV-2 Antibodies. *Chemosensors* **2023**, *11* (4), 222.
(42) Hardy, P. M.; Nicholls, A. C.; Rydon, H. N. The nature of glutaraldehyde in aqueous solution. *J. Chem. Soc. D* **1969**, *10*, 565−566.
(43) Reverberi, R.; Reverberi, L. Factors affecting the antigen-antibody reaction. *Blood transfus.* **2007**, *5* (4), 227.
(44) Stenberg, M.; Nygren, H. Kinetics of antigen-antibody reactions at solid-liquid interfaces. *J. Immunol. Methods.* **1988**, *113* (1), 3−15.
(45) Akashi, Y.; Kiyasu, Y.; Takeuchi, Y.; Kato, D.; Kuwahara, M.; Muramatsu, S.; Ueda, A.; Notake, S.; Nakamura, K.; Ishikawa, H.; Suzuki, H. Evaluation and clinical implications of the time to a positive results of antigen testing for SARS-CoV-2. *J. Infect Chemother.* **2022**, *28* (2), 248−251.
(46) Friedman, A. K.; Shi, W.; Losovyj, Y.; Siedle, A. R.; Baker, L. A. Mapping microscale chemical heterogeneity in Nafion membranes with X-ray photoelectron spectroscopy. *J. Electrochem. Sci.* **2018**, *165* (11), H733−H741.
(47) Xia, J.; Guo, H.; Yu, G.; Chen, Q.; Liu, Y.; Liu, Q.; Luo, Y.; Li, T.; Traversa, E. 2D vanadium carbide (MXene) for electrochemical synthesis of ammonia under ambient conditions. *Catal. Lett.* **2021**, *151*, 3516.
(48) Susac, D.; Kono, M.; Wong, K. C.; Mitchell, K. A. R. XPS study of interfaces in a two-layer light-emitting diode made from PPV and Nafion with ionically exchanged $Ru(bpy)_3^{2+}$. *Appl. Surf. Sci.* **2001**, *174* (1), 43−50.
(49) Cao, Y.; Deng, Q.; Liu, Z.; Shen, D.; Wang, T.; Huang, Q.; Du, S.; Jiang, N.; Lin, C.; Yu, J. Enhanced thermal properties of poly (vinylidene fluoride) composites with ultrathin nanosheets of MXene. *RSC Adv.* **2017**, *7* (33), 20494−20501.
(50) Liu, C.; Pan, H.; Hu, H.; Wei, W.; Lu, Q.; Zhao, C.; Wang, H.; Du, F. Vanadium carbide MXene: as a reductant for the synthesis of gold nanoparticles and its biosensing application. *Amino Acids* **2022**, *54* (8), 1173−1181.
(51) Lan, L.; Fan, X.; Yu, S.; Gao, J.; Zhao, C.; Hao, Q.; Qiu, T. Flexible Two-Dimensional Vanadium Carbide MXene-Based Membranes with Ultra-Rapid Molecular Enrichment for Surface-Enhanced Raman Scattering. *ACS Appl. Mater. Interfaces.* **2022**, *14* (35), 40427−40436.
(52) Son, J. G.; Yoon, S.; Shon, H. K.; Moon, J. H.; Joh, S.; Lee, T. G. Ar-gas cluster ion beam in ToF-SIMS for peptide and protein analysis. *Biointerphases* **2020**, *15* (2). DOI. DOI: 10.1116/6.0000105.
(53) Mehmandoust, M.; Gumus, Z. P.; Soylak, M.; Erk, N. Electrochemical immunosensor for rapid and highly sensitive detection of SARS-CoV-2 antigen in the nasal sample. *Talanta* **2022**, *240*, No. 123211.
(54) Wolfe, M.; Webb, S.; Chushak, Y.; Krabacher, R.; Liu, Y.; Swami, N.; Harbaugh, S.; Chávez, J. A high-throughput pipeline for design and selection of peptides targeting the SARS-Cov-2 Spike protein. *Sci. Rep.* **2021**, *11* (1), 21768.
(55) Tortolini, C.; Angeloni, A.; Antiochia, R. A comparative study of voltammetric vs impedimetric immunosensor for rapid SARS-CoV-2 detection at the point-of-care. *Electroanalysis* **2023**, *35* (4), No. e202200349.
(56) Lobato, A.; Šubic, M.; Romih, T.; Žibret, L.; Metarapi, D.; Benčina, M.; Jerala, R.; Vidović, K.; Hočevar, S. B.; Tasić, N. Development of a simple gelatin-based sensing platform for the sensitive label-free impedimetric detection of SARS-CoV-2. *Electrochim. Acta* **2023**, *463*, No. 142823.
(57) Büyüksünetçi, Y. T.; Çitil, B. E.; Anık, Ü. An impedimetric approach for COVID-19 detection. *Analyst* **2021**, *147* (1), 130−138.
(58) Rahmati, Z.; Roushani, M.; Hosseini, H.; Choobin, H. Electrochemical immunosensor with Cu 2 O nanocube coating for detection of SARS-CoV-2 spike protein. *Microchim. Acta.* **2021**, *188*, 1−9.
(59) Brazaca, L. C.; Imamura, A. H.; Gomes, N. O.; Almeida, M. B.; Scheidt, D. T.; Raymundo-Pereira, P. A.; Oliveira, O. N.; Janegitz, B. C.; Machado, S. A. S.; Carrilho, E. Electrochemical immunosensors using electrodeposited gold nanostructures for detecting the S proteins from SARS-CoV and SARS-CoV-2. *Anal. Bioanal. Chem.* **2022**, *414* (18), 5507−5517.
(60) Al-Qaoud, K. M.; Obeidat, Y. M.; Al-Omari, T.; Okour, M.; Al-Omari, M. M.; Ahmad, M. I.; Alshadfan, R.; Rawashdeh, A. M. The development of an electrochemical immunosensor utilizing chicken IgY anti-spike antibody for the detection of SARS-CoV-2. *Sci. Rep.* **2024**, *14* (1), 748.
(61) Ramanathan, S.; Gopinath, S. C.; Hilmi Ismail, Z.; Subramaniam, S. Nanodiamond conjugated SARS-CoV-2 spike protein: electrochemical impedance immunosensing on a gold microelectrode. *Microchim. Acta.* **2022**, *189* (6), 226.

https://doi.org/10.1021/acsami.4c04567
ACS Appl. Mater. Interfaces XXXX, XXX, XXX−XXX

3.3 Manuscript 3: "Label-Free and Sensitive Detection of *Citrus Bark Cracking Viroid* in Hop Using $Ti_3C_2T_x$ MXene-Modified Genosensor"

Sensors & Actuators: B. Chemical 423 (2025) 136762

Contents lists available at ScienceDirect

Sensors and Actuators: B. Chemical

journal homepage: www.elsevier.com/locate/snb

Label-free and sensitive detection of *Citrus Bark Cracking Viroid* in hop using $Ti_3C_2T_x$ MXene-modified genosensor

Alnilan Lobato [a,b], Ivan Konjević [a,c], Sebastjan Radišek [d], Jernej Jakše [e], Helena Volk [e], Monika Hermanová [f], Miroslav Fojta [f], Jan Paštika [g], Zdeněk Sofer [g], Rui Gusmão [g,**], Samo B. Hočevar [a], Nikola Tasić [a,*]

[a] Department of Analytical Chemistry, National Institute of Chemistry, Ljubljana, Slovenia
[b] International Postgraduate School Jožef Stefan, Ljubljana, Slovenia
[c] Faculty of Chemistry and Chemical Technology, University of Ljubljana, Ljubljana, Slovenia
[d] Slovenian Institute of Hop Research and Brewing, Žalec, Slovenia
[e] Biotechnical Faculty, University of Ljubljana, Ljubljana, Slovenia
[f] Institute of Biophysics, Academy of Science of the Czech Republic, Brno, Czech Republic
[g] Department of Inorganic Chemistry, University of Chemistry and Technology Prague, Czech Republic

ARTICLE INFO

Keywords:
CBCVd
Viroid
Hop
RNA detection
Impedimetric genosensor
MXene

ABSTRACT

Since the discovery of *Citrus bark cracking viroid* (CBCVd) in hops in 2007, affected hop-growing countries such as Slovenia and Germany have been actively pursuing efficient and easily accessible diagnostic tools that could contribute to the early detection of CBCVd in the field. In the early stages of CBCVd infection, typical symptoms or subtle signs of spread may not be evident. Detection becomes feasible only when the plant begins to display symptoms. Unfortunately, there is currently no treatment available, which requires the removal of infected plants as the only viable solution. However, this approach leads to significant economic losses on a large scale. This work demonstrates the development and study of a sensitive, selective, and label-free impedimetric genosensor for the detection of CBCVd in total RNA hop samples. The genosensor is based on a supporting glassy carbon electrode modified with streptavidin-agarose beads, which serve as an effective immobilization layer for a biotinylated single-stranded DNA capture probe. The integration of a 2D-layered $Ti_3C_2T_x$ MXene into the sensing architecture resulted in a significantly improved electroanalytical performance of the genosensor. Several fabrication and operational parameters were optimized, such as the streptavidin-agarose beads deposition time, capture probe immobilization time and concentration, and sample incubation time. The optimized genosensor exhibited a limit of detection of only 0.5 fg μL^{-1} (5.5 fmol L^{-1}) in combination with a one-hour incubation with the denatured total RNA hop extract, thus eliminating the need for an additional and laborious amplification step.

1. Introduction

The hop (*Humulus lupulus L.*) is an economically important crop due to the worldwide use of its secondary metabolites in breweries [1] and pharmaceutical companies [2]. Over the past three decades, global hop production has surged, with the United States and Germany leading the way [3]. Hops are susceptible to many diseases, including those caused by viroids, the smallest biological pathogens capable of replication using host enzymes. Viroid infections can be highly aggressive, resulting in reduced plant growth, dwarfing, abnormal leaf shapes, yellowing, necrosis, and leaf rolling [4]. The structure of viroids consists of non-encapsulated, single-stranded, circular RNA molecules ranging in size from 239 to 401 nucleotides, whose nucleotide sequence does not allow protein-coding [5]. Viroids spread through various ways,

* Corresponding author at: Department of Analytical Chemistry, National Institute of Chemistry, Ljubljana, Slovenia.
** Corresponding author at: Department of Inorganic Chemistry, University of Chemistry and Technology Prague, Czech Republic.
E-mail addresses: alnilan.lobato@ki.si (A. Lobato), ivan.konjevic@ki.si (I. Konjević), sebastjan.radisek@ihps.si (S. Radišek), Jernej.Jakse@bf.uni-lj.si (J. Jakše), Helena.Volk@bf.uni-lj.si (H. Volk), hermanova@ipb.cz (M. Hermanová), fojta@ibp.cz (M. Fojta), jan.pastika@vscht.cz (J. Paštika), zdenek.sofer@vscht.cz (Z. Sofer), rui.gusmao@vscht.cz (R. Gusmão), samo.hocevar@ki.si (S.B. Hočevar), nikola.tasic@ki.si (N. Tasić).

https://doi.org/10.1016/j.snb.2024.136762
Received 26 April 2024; Received in revised form 7 October 2024; Accepted 9 October 2024
Available online 11 October 2024
0925-4005/© 2024 The Author(s). Published by Elsevier B.V. This is an open access article under the CC BY license (http://creativecommons.org/licenses/by/4.0/).

predominantly by mechanical contact with agricultural equipment, by leaf-to-leaf contact, and by human handling, as well as by seeds, pollen, and insect vectors [6].

The *Citrus bark cracking viroid* (CBCVd) was first discovered in citrus fruits in 1988 and was classified as a mild pathogen for these plants [7, 8]. However, in 2007, CBCVd was discovered in Slovenian hop plants, leading to the complete eradication of over 300 ha of hop fields due to the viroid's aggressive nature [9,10]. CBCVd is particularly devastating for hop cultivation, causing severe symptoms such as plant stunting (reduced growth and overall size compared to healthy plants), root dry rot, and plant dieback three to five years after infection. Despite the Slovenian national eradication program, CBCVd continues to threaten farmers and hop production as an emerging highly aggressive pathogen. In 2019, a CBCVd outbreak appeared in Germany, and the most recent report comes from Brazil in 2023 [11], posing a threat to hop-growing regions in Europe and worldwide [10].

The emergence of such pathogens underlines the urgent need for rapid and straightforward viroid detection methods. Early identification of plant diseases can prevent or limit the spread of emerging infections, ultimately reducing costs and minimizing damage caused by contamination [12]. The insidious nature of CBCVd, characterized by the absence of typical symptoms or the presence of only atypical symptoms during the early stages of infection, highlights the importance of simple and reliable on-site detection for farmers [9].

Typically, the identification of pathogens such as viruses and viroids relies on conventional or advanced molecular biology techniques [13]. These methods tend to be both costly and time-consuming. Examples of such methods include polymerase chain reaction (PCR), reverse transcription quantitative PCR (RT-qPCR), loop-mediated isothermal amplification (LAMP), enzyme-linked immunosorbent assay (ELISA), and CRISPR-Cas-based detection [14].

Alternatively, electrochemistry offers simple and cost-effective approaches for detecting microbial pathogens. Designing biosensors for plant pathogens typically involves the modification of the electrode surface to immobilize biological recognition elements for interaction with the target [15]. While significant progress has been made in the development of electrochemical biosensors for plant pathogens over the past three decades [16], reports specifically addressing viroids remain scarce. For example, a graphene/zinc oxide nanocomposite genosensing platform capable of detecting a CCCVd (*Coconut cadang-cadang viroid*) RNA oligonucleotide over a linear range of 1.0×10^{-11} M to 1.0×10^{-6} M was presented [17]. The initial modification layer was functionalized with 1-pyrenebutyric acid N-hydroxysuccinimide ester to enable chemical binding of the single-stranded DNA capture probe. Subsequent hybridization with the single-stranded RNA oligonucleotide target was monitored by either electrochemical impedance spectroscopy (EIS) or differential pulse voltammetry (DPV). More recently, a similar genosensor for CCCVd detection was developed based on gold nanoparticles decorated phosphorene nanohybrid with graphene, which achieved a similar linear range of 1.0×10^{-11} M to 1.0×10^{-6} M, with a limit of detection of 2.8×10^{-12} M [18]. In both studies, the detection target consisted of artificially prepared single-stranded RNA corresponding to a segment of the CCCVd sequence.

In this work, a sensitive and selective genosensor was demonstrated, exploiting streptavidin-agarose beads as a biocompatible immobilization matrix for a single-stranded DNA capture probe and the attractive electrocatalytic properties of 2D-layered $Ti_3C_2T_x$ MXene. The genosensor successfully detected CBCVd in infected total RNA hop samples obtained directly from the field, without the need for labeling or laborious amplification steps.

2. Experimental

2.1. Chemicals and materials

All reagents were of analytical grade and were used without further purification. All aqueous solutions were prepared using ultrapure water with resistivity not less than 18.2 MΩ cm at 298 K (Milli-Q, Millipore, Corp., Marlborough, USA). Titanium aluminum carbide (Ti_3AlC_2) was acquired from Jinzhou Haixin Metal Materials (China).

Streptavidin-agarose beads (STR-AGAR beads) from *Streptomyces avidinii*, sodium hydroxide (NaOH), and sodium chloride (NaCl) were purchased from Merck (Darmstadt, Germany), sodium azide (NaN_3), glycine, and bovine serum albumin (BSA) from Sigma Aldrich (St. Louis, USA), disodium hydrogen phosphate dihydrate ($Na_2HPO_4{\cdot}2\ H_2O$) from Kemika (Zagreb, Croatia), alumina (Al_2O_3, 0.3 μm) and polishing cloth from Buehler (Lake Bluff, USA), potassium dihydrogen phosphate (KH_2PO_4) and potassium hexacyanoferrate (III) ($K_3[Fe(CN)_6]$) from Fluka (Switzerland), and potassium chloride (KCl) and potassium hexacyanoferrate (II) ($K_4[Fe(CN)_6]$) from Riedel-de Haën (Seelze, Germany). TE buffer (10 mM Tris-HCl, 1 mM EDTA, pH 8.0) and nuclease-free water were purchased from Integrated DNA Technologies (Coralville, USA). The phosphate-buffered saline (PBS, pH=7.4) consisted of 8.00 g of NaCl, 200.0 mg of KCl, 1.81 g of $Na_2HPO_4{\cdot}2\ H_2O$, and 240.0 mg of KH_2PO_4 in 1.0 L purified H_2O.

The capture probe sequence, 50 bp in length (5′-AGAGTTGTATC-CACCGGGTAGTTTCTTTCTCAGGTCGCGAAGGAAGAAGC-3'), was synthesized by Eurofins Genomics (Germany) with a biotin moiety attached to the 5′ end. This probe was designed based on the sequence of the CBCVd isolate Hl-1 (GenBank accession number KM211546.1). The capture probe anneals perfectly to the region spanning nucleotides 182–231 of the CBCVd genome.

2.2. Total RNA isolation and CBCVd quantification

The viroid source was infected hop plants of the variety 'Celeia' from the pathogen reference collection of the Diagnostic Laboratory for Plant Protection at the Institute of Hop Research and Brewing, Žalec, Slovenia. The plants were biolistically inoculated in 2013 with infectious cDNA constructs (GenBank X07397, GenBank KM211546, GenBank X07405) of single viroids (CBCVd, HLVd) and combinations (CBCVd+HLVd and HSVd+HLVd) [19]. Viroid-free hop plants of the same variety and tomato (*Solanum lycopersicum L.*; cv. Heinz 1370) plants served as the source of negative control plant samples. From each plant, three fully developed leaves were sampled at phenological stage BBCH 38 for hops and BBCH 29 for tomatoes, then stored at −80°C until being used for RNA isolation. Total RNA was extracted from 100 mg of leaf tissue taken from all three sampled leaves of each plant using a CTAB protocol without DNase treatment [20]. The total RNA was eluted in 50 μL of a TE buffer (10 mM Tris-HCl, 1 mM EDTA, pH 8.0). The RNA concentration was measured using the Qubit® 3.0 Fluorometer (Thermo Fisher Scientific, USA) and stored at −80°C (Table S1).

The High-Capacity cDNA Reverse Transcription Kit (Thermo Fisher Scientific, USA) was used to produce cDNA from total RNA hop samples containing 500 ng RNA. The absolute quantification of CBCVd was performed by 7500 Real-Time PCR System (Thermo Fisher Scientific, USA) using a linearised plasmid containing CBCVd sequence as standards. The reaction was performed using SybrGreen chemistry and primers CBCVd-PCR-F-q: 5'-TCACTGGCGTCCAGCACC-3' and CBCVd-PCR-R-q: 5'-AGGAAGAAGCGACGATCGG-3' [21].

2.3. Synthesis of $Ti_3C_2T_x$ MXene

The synthesis of $Ti_3C_2T_x$ MXene followed the same protocol as previously published [22]. Briefly, the precursor Ti_3AlC_2 MAX phase was etched with 40 % HF for four days, followed by LiF/HCl for two days. The product was then repeatedly washed and centrifuged with H_2O until approaching neutral pH, being dried at 50°C in a vacuum oven. The resulting material was then stored in polar organic solvent at 4°C.

2.4. Characterization of $Ti_3C_2T_x$ MXene

The morphology of the precursor and synthesized materials was examined by scanning electron microscopy (SEM) with field emission Tescan LYRA$_3$ GM dual-beam microscope and Tescan MAIA$_3$ (Tescan, Czech Republic) at an acceleration voltage of 5 kV. Elemental composition was investigated by energy-dispersive X-ray spectroscopy (EDX) using an X-MaxN detector from Oxford Instruments at 20 kV acceleration voltage. For both SEM and EDX analyses, the Ti_3AlC_2 powder and the colloidal suspension of $Ti_3C_2T_x$ MXene were drop-cast on copper tape. Scanning transmission electron microscopy (STEM) was performed at Tescan MAIA$_3$ electronic microscope with a STEM sample holder and X-MaxN 150 EDX detector. The diluted suspension of MXene was drop-cast on a 200 mesh Cu TEM grid (Ted Pella, USA), and then dried. STEM measurements were carried out using a 30 kV electron beam. An InVia Raman microscope (Renishaw, England) was used for Raman spectroscopy measurements in backscattering geometry with a CCD detector. An Nd:YAG laser (532 nm, 50 mW) with a 2400 line mm^{-1} diffraction grating, an applied power of 5 %, and a 20x objective were used for the measurements. The Raman spectrum was collected with 100 accumulations in the Raman range of 100–900 cm^{-1} at room temperature. X-ray diffraction (XRD) measurements were carried out using a Bruker D2 Phaser benchtop diffractometer (Bruker, Germany) with a Cu Kα radiation source (λ=1.54178 Å). The diffraction patterns were acquired in the range of 2θ from 5 to 80° at room temperature. The data were evaluated by HighScore Plus 4.9 software. Fourier transform-infrared spectroscopy (FTIR) measurements were performed on a Nicolet iS50R FTIR spectrometer (Thermo Scientific, USA). The measurement was performed with a DLaTGS detector and a KBr beam splitter in the range 4000–400 cm^{-1} at a resolution of 4 cm^{-1}, with a total of 265 scans. FTIR spectra were measured in a KBr pellet made from 300 mg of KBr and 1 mg of materials. OMNIC software was used to acquire and process the data. Baseline correction and data treatment were performed according to recommendations by T. Parker et al. [23].

2.5. Genosensor fabrication

Before use, the GCE underwent mechanical polishing using 0.3 μm alumina slurry. The GCE was then sonicated in ethanol for 2 min, washed with ultrapure water, and dried using high-purity nitrogen gas (0.2 bar). Next, 40 mg of commercial STR-AGAR beads were dissolved in 2 mL of phosphate-buffered saline (PBS, pH 7.4) containing 0.03 % sodium azide. 10 μL of the STR-AGAR beads solution was carefully drop-casted onto the GCE surface and stored at 4 °C for 2 h.

Modification with $Ti_3C_2T_x$ MXene: the electrocatalytic 2D-layered $Ti_3C_2T_x$ MXene in ethanol was heated to approximately 30°C until the solvent evaporated slowly. The remaining powder was then redispersed in ultrapure water to obtain an aqueous solution with a concentration of 2 mg mL^{-1}. After vortexing for 1 min, the MXene suspension was mixed with the STR-AGAR beads solution in a 1:1 ratio. The resulting $Ti_3C_2T_x$-STR-AGAR mixture was vortexed for 10 seconds before depositing 4.5 μL of it onto the supporting GCE surface and stored at 4 °C for 2 h.

Between each modification step, the electrode surface was rinsed with ultrapure water for 1 min and dried using a gentle stream of nitrogen gas (0.2 bar).

Next, 8 μL of the biotinylated capture probe solution (50 ng μL^{-1}) was drop-casted onto the modified electrode surface and incubated for 2 h at 4 °C. To prevent non-specific binding, 8 μL of glycine solution (10 μg mL^{-1}) was deposited onto the surface of the genosensor for 30 min at 4 °C.

2.6. EIS genosensing

Total RNA hop samples extracted from hop plants underwent denaturation in a 95°C water bath for 3 min, followed by rapid cooling on ice for 1 min. Finally, 8 μL of the real sample solution was applied to the sensor surface and incubated for 60 min at room temperature. The sensor was then quickly rinsed with ultrapure water, and electrochemical detection was conducted in the presence of 5 mM $[Fe(CN)_6]^{3-/4-}$ in 0.1 M KCl. The fabrication of the genosensor and detection of CBCVd are depicted in Fig. 1.

2.7. Electrochemical measurements

Cyclic voltammetric (CV) and electrochemical impedance spectroscopic (EIS) measurements were carried out with a portable PalmSens 4 electrochemical workstation (potentiostat/galvanostat) operated by the PSTrace 5.9 software (PalmSens BV, Netherlands). In all experiments, a glassy carbon supporting electrode (GCE, 3 mm) was used, in combination with a single junction Ag/AgCl/KCl(satd.) reference electrode, and a Pt rod as the counter electrode. All electrodes were purchased from Metrohm (Herisau, Switzerland). EIS spectra were recorded in the frequency range of 10^5-10^{-1} Hz, at the potential of +0.14 V, with an amplitude of 5 mV, in a solution of 5 mM $[Fe(CN)_6]^{3-/4-}$ in 0.1 M KCl. CV measurements were performed in the potential range of −0.5–1.0 V or −0.2–0.6 V, with a scan rate of 100 mV s^{-1}.

3. Results and discussion

3.1. Optimization of the genosensor fabrication and operation

The genosensor development protocol was optimized with respect to several parameters. The increase in charge transfer resistance (R_{ct}) of the genosensor before and after incubation with a total RNA hop sample infected with CBCVd was used as a feedback signal to determine the optimal fabrication and measurement parameters, i.e., $\Delta R = R_{inc} - R_{blank}$. All R_{ct} values, i.e., R_{inc} (after sample incubation) and R_{blank} (before sample incubation), were determined by fitting the raw impedance spectra with a Randles-type equivalent electrical circuit ($R_S([R_{ct}Z_W]Q_{dl})$) representing the real physicochemical processes at the genosensor/electrolyte interface. Herein, R_S corresponds to the solution resistance, Q_{dl} is the constant phase element (CPE) accounting for the non-ideal double-layer capacitance, R_{ct} is the charge transfer resistance of the genosensor/electrolyte interface, and Z_W is the Warburg element that models the diffusion phenomenon. Firstly, we optimized several key parameters influencing the performances of the CBCVd genosensor, i.e., (i) STR-AGAR beads deposition time, (ii) capture probe immobilization time, (iii) sample incubation time, and (iv) capture probe concentration.

The interaction between streptavidin, a tetrameric protein from *Streptomyces avidinii*, and biotin, a water-soluble vitamin, is one of the fundamental and widespread phenomena in molecular biology and biotechnology [24,25]. This interaction has found numerous applications, including affinity purification [26], immunoassays [27], and biosensing [28]. In addition to a strong immobilization of the biotinylated single-stranded DNA capture probe, the STR-AGAR beads serve as an effective adhesion agent to prevent leaching of the sensing layer from the electrode surface and its dissolution during exposures to solutions in the subsequent fabrication steps. The STR-AGAR beads were introduced from the 20 mg mL^{-1} PBS solution (pH 7.4) by a simple drop-casting procedure at 4°C. As depicted in Fig. 2a, the highest analytical signal of the genosensor for 720 fg μL^{-1} CBCVd was obtained when STR-AGAR beads were left to deposit for two hours, whereas shorter and longer deposition times resulted in lower signals. After the optimization of the STR-AGAR beads deposition time, we investigated the effect of the biotinylated capture probe immobilization time upon the genosensor impedimetric response. It was observed (Fig. 2b) that the two-hour immobilization exhibited the highest performance of the genosensor, considering both the signal height and reproducibility when compared to the shorter or longer exposure times to the biotinylated capture probe. The binding event between the STR units confined to the electrode surface and the biotinylated capture probe moieties is a dynamic process that also involves the reverse reaction; however, at the

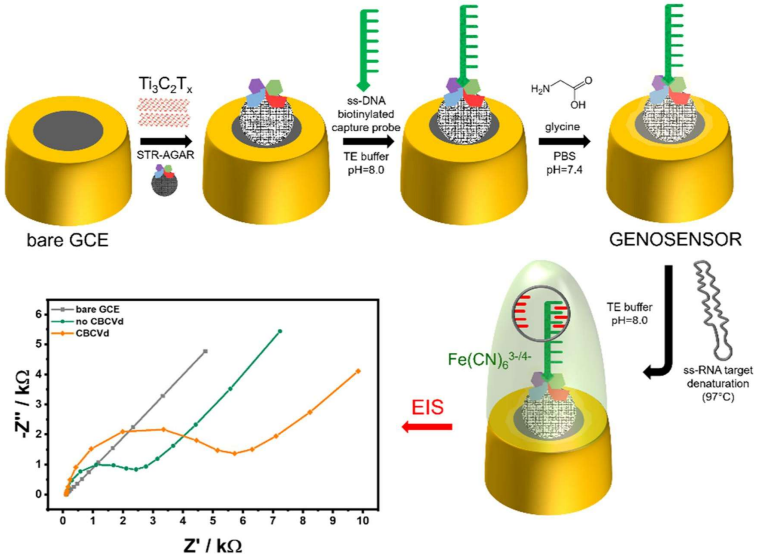


Fig. 1. Fabrication of the CBCVd genosensor and its impedimetric detection.

same time, the steric effects should be taken into consideration [25]. Consequently, a one-hour immobilization might be insufficient to stabilize the sensing surface with the immobilized capture probe; in contrast, longer immobilization times than two hours promote the reverse reaction, i.e., detachment of the capture probe, and/or its improper conformation that leads to poorer performance. Finally, we optimized the time necessary for incubating the total RNA hop sample, and the corresponding results are shown in Fig. 2c. As can be seen, shorter incubation times of 15 and 30 min led to significantly lower signals in comparison with incubation times of 60 and 90 min. Notably, the incubation time of 60 min revealed the highest impedimetric signal along with favorably improved reproducibility. In continuation, all experiments in this study were carried out using the incubation time of one hour.

The next study tackled the effect of capture probe concentration on the genosensor performance, as shown in Fig. S1. Evidently, the impedimetric response was the highest when the biotinylated capture probe concentration was 50 ng μL^{-1}, along with its favorable reproducibility; this concentration was used for all subsequent studies.

3.2. *Electrochemical characterization of the genosensor fabrication*

Using previously optimized parameters, a step-by-step investigation of the genosensor fabrication process was conducted in combination with CV and EIS detection in 5 mM $[Fe(CN)_6]^{3-/4-}$ + 0.1 M KCl, including the final incubation step in total RNA hop samples. By following the electrochemical signals, we gained insights and control into gradual changes occurring at the genosensor surface upon each

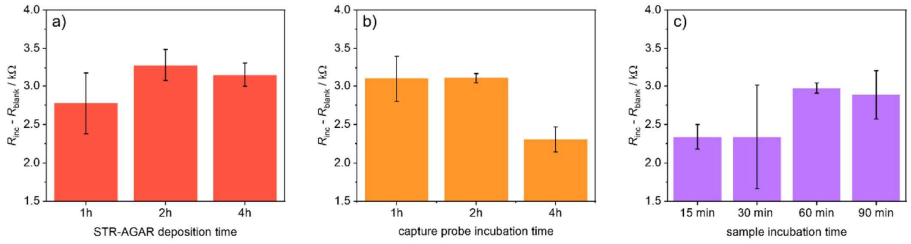


Fig. 2. The effect of (a) STR-AGAR beads deposition time (capture probe incubation time: 2 h, sample incubation time: 60 min), (b) capture probe incubation time (STR-AGAR beads deposition time: 2 h, sample incubation time: 60 min), and (c) sample incubation time (STR-AGAR beads deposition time: 2 h, capture probe incubation time: 2 h) upon the genosensor response. The concentration of CBCVd was 720 fg μL^{-1}, and the concentration of the capture probe was 25 ng μL^{-1}. The error bars represent the relative standard deviation of three independent measurements. Relevant EIS datasets corresponding to the optimization studies are presented in Table S2.

modification step, attaining feedback to successfully fabricate a genosensor with optimized sensitivity and reproducibility. Using a simple Randles circuit $R_S([R_{ct}Z_W]Q_{dl})$, we quantified the impedimetric changes occurring at the genosensor/electrolyte interface. The bare GCE exhibited an impedimetric behavior with a negligible high-frequency semicircle and a diffusion tail typical for conductive carbon surfaces (Fig. 3a). After the introduction of STR-AGAR beads, the impedimetric spectrum altered with the formation of a semicircle, corresponding to a significant increase in the charge-transfer resistance due to the deposition of a less conductive coating. In addition, the incorporation of a biotinylated capture probe further increased the size of the semicircle, reflecting an increased R_{ct}; similarly, the last modification layer, including glycine, contributed to a significantly enlarged R_{ct}, as shown in Fig. 3a. Finally, the dark-green EIS spectrum shows the genosensor response after incubation in a real total RNA hop sample solution of 250 fg μL^{-1} CBCVd, revealing a well-developed impedimetric signal. Similarly, the cyclic voltammograms (Fig. 3b) showed a stepwise decrease of the anodic and cathodic signals of $[Fe(CN)_6]^{3-/4-}$ accompanied by increasing peak-to-peak separation that corresponds to the deposition of genosensor building blocks, reflecting the changes of the interface diffusion pattern. A small signal observed at bare GCE (at ca. −0.4 V) can be attributed to the oxygen reduction reaction. At the same time, Fig. 3 demonstrates a significantly enhanced sensitivity of the EIS vs. CV, particularly considering the detection of the CBCVd viroid in the real sample (dark-green curve).

To test both the potential influence of the supporting buffer and the stability of the sensing layer, 8 µL of the TE buffer was drop-casted onto the fully fabricated genosensor, followed by a one-hour incubation step. As shown in Figure S2, the incubation for one hour in the TE buffer did not affect the EIS response of the genosensor; this was also supported by the fitting parameters, indicating negligible changes, as shown in Table S4.

The incorporation of the Ti_3C_2Tx MXene into the genosensor architecture unveiled a significant improvement in the electrochemical communication between the upper genosensor interface, where hybridization and detection take place, and the lower part, which includes the STR-AGAR beads combined with Ti_3C_2Tx MXene and the supporting GCE. MXenes are state-of-the-art 2D-layered materials composed of transition metal carbides or nitrides, which exhibit remarkable versatility in various application areas, such as catalysis [29,30], ion batteries [31,32], gas sensors [22,33], and biosensors [34,35]. Upon introducing $Ti_3C_2T_x$, MXene, the preliminary measurements revealed a ca. 5-fold increase in the sensitivity of the genosensor for detecting CBCVd in real total RNA hop samples. The step-by-step fabrication of the $Ti_3C_2T_x$ MXene-modified genosensor is shown in Figure S3, with the corresponding fitting parameters listed in Table S5.

3.3. *Structural and surface characterization of $Ti_3C_2T_x$ MXene*

The MXene $Ti_3C_2T_x$ was obtained by selective etching of the Al layer of the precursor Ti_3AlC_2 MAX phase, as described in the Experimental section. The SEM and STEM micrographs of the observed flakes displayed the typical accordion-like morphology of the multilayer $Ti_3C_2T_x$ MXene, as shown in Fig. 4a and S4. The flakes exhibit tightly packed and loosely packed features depending on the extension in which Al atoms are replaced by surface functional groups such as oxygen (-O), hydroxyl (-OH), or fluorine (-F) [36]. Subsequently, the interlayer forces become weaker, making their delamination possible. The EDX mapping of elements of the detailed area of the selected $Ti_3C_2T_x$ flake with loosely packed sheets is shown in Fig. 4b, which shows the abundant distribution of C, O, F, and Ti elements, while Al is scarcely detected. Another example of SEM/EDX mapping for Ti_3AlC_2 and $Ti_3C_2T_x$ is shown in Figure S4. The averaged EDX spectra of Ti_3AlC_2 and $Ti_3C_2T_x$, obtained on multiple flakes at 20 kV, are shown in Fig. 4c, and the respective quantification in Table S6. In both cases, the quantified at% of Ti/C indicates a ratio of 1.3, close to the expected for Ti_3C_2 stoichiometry of 1.5. One of the major differences between the EDX spectra of the materials is the significant decrease of the Al Kα1 line at 1.4 keV, from an initial 17.3 at% to a considerably lower amount of 1.7 at%, also indicating the successful etching of the precursor Ti_3AlC_2 MAX phase. Furthermore, for $Ti_3C_2T_x$, a new peak is quantified at 0.68 keV corresponding to the F Kα line at a level of 26.8 at% for F. The level of quantified O also increased by 20 % for the $Ti_3C_2T_x$ after the etching of the MAX phase. Both levels of F and O elements are related to the surface functional groups mentioned before.

The Raman spectrum of the precursor MAX phase and MXene obtained in the 100–900 cm^{-1} range, are shown in Fig. 4d, providing information related to the bonds present in the structure by assessing lattice vibrations. For the starting Ti_3AlC_2, the peaks at 148, 244, and 434 cm^{-1} correspond to the $E_{2\,g}$, $E_{1\,g}$, and $A_{1\,g}$ vibrational modes, respectively [37]. The peak at 608 cm^{-1} can be assigned to $E_{1\,g}$ vibration modes corresponding to the in-plane vibration of the Ti–C bond [38]. In comparison, for the $Ti_3C_2T_x$ MXene, with the Al layer etching, surface functional groups (=O, -OH, and –F terminations) are adsorbed and intercalated within the interlayer spacing, causing variations in the local environment of the atoms and affecting lattice vibrations of the unit cell.

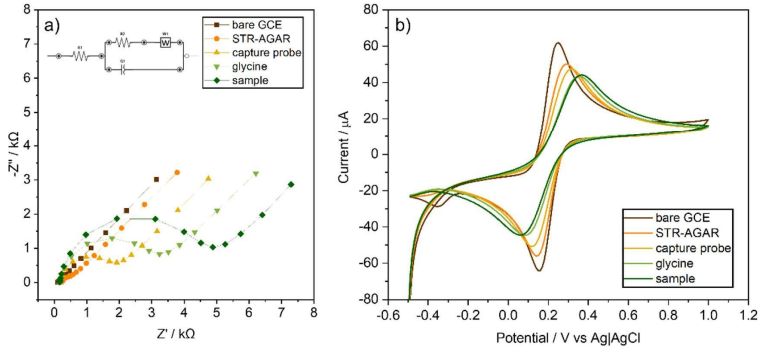


Fig. 3. Characterization of the step-by-step fabrication of the genosensor using (a) EIS and (b) CV measurements in 5 mM $[Fe(CN)_6]^{3-/4-}$ + 0.1 M KCl. The corresponding fitting parameters are listed in Table S3.

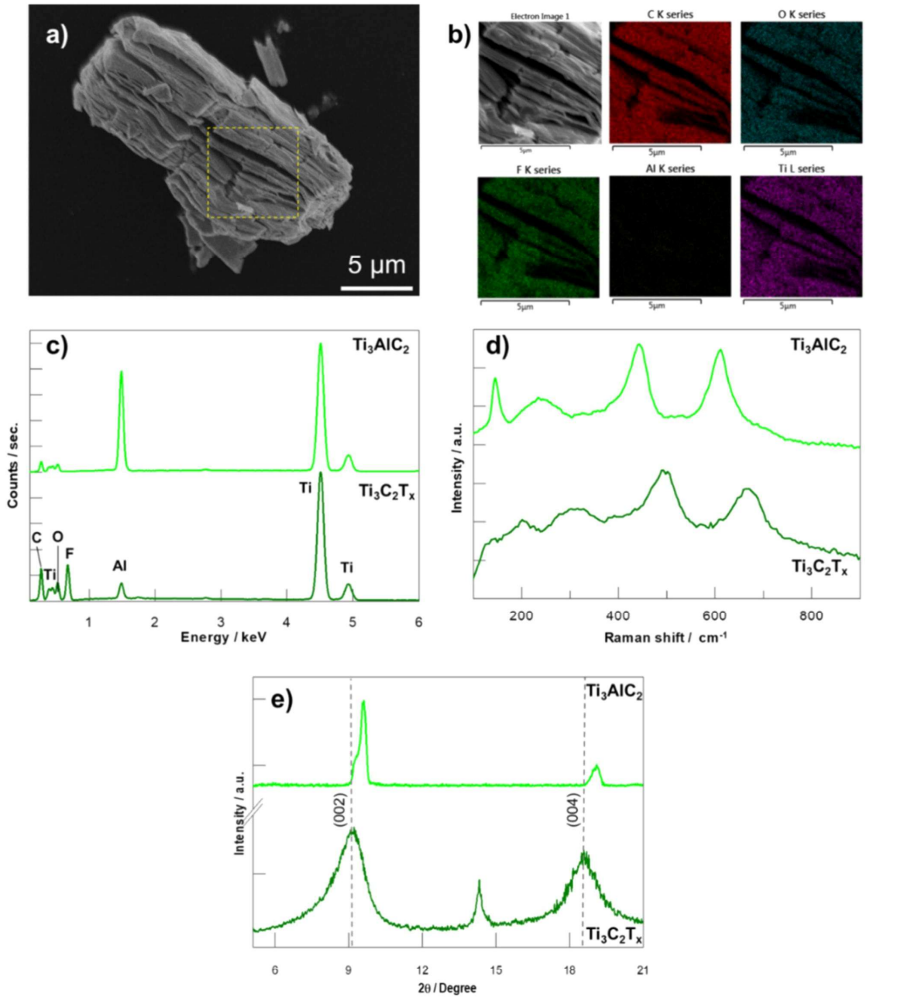


Fig. 4. (a) Overlay of in-beam BSE and SE modes micrograph of a $Ti_3C_2T_x$ MXene multilayer flake after etching with the highlight of the area used for (b) EDX mapping of elements, (c) averaged EDX spectra of Ti_3AlC_2 MAX phase and $Ti_3C_2T_x$ MXene, and (d) comparison of Raman spectrum of Ti_3AlC_2 MAX phase and $Ti_3C_2T_x$ MXene with 532 nm LL. (e) X-ray diffraction (XRD) patterns for low 2θ region with vertical lines marking the position of (002) and (004) peaks of ICDD card no. 04–14–5068.

Thus, the $Ti_3C_2T_x$ spectrum peaks have broadened and a blue shift to higher Raman frequencies. The peak at 148 cm^{-1} was initially intense for Ti_3AlC_2, displaying in-plane vibration Ti atoms, with the major contribution of Ti-Al vibrations, for the case of $Ti_3C_2T_x$ is greatly decreased, broadened, and shifted to 201 cm^{-1}. The remaining peaks of MXene have higher Raman shifts but peak intensities were sustained, with the peak at 314 cm^{-1} having contributions from out-of-plane vibration of the Ti–C bond and H atoms of $Ti_3C_2(OH)_2$ [39]. The peak at 492 cm^{-1} has contributions of in-plane vibration of O atoms of OH MXene terminations [40].

X-ray diffraction (XRD) was used to analyze the crystal structure and phase composition of both materials and further understanding of the successful synthesis of $Ti_3C_2T_x$. As shown in Figure S5a and Fig. 4e, there is a good match of the diffraction pattern of the precursor Ti_3AlC_2 and

the ICDD card no. 04–14–5068 [41], displaying a well-crystallized structure, corresponding to layered ternary 312 MAX phase, with a hexagonal crystal system and $P6_3/mmc$ space group. In Fig. 4e, for the region $5^{\circ}<2\theta<21^{\circ}$, the MAX phase presents the typical diffraction peaks mainly at $2\theta=9.6^{\circ}$ and 19.1° for (002) and (004) planes, respectively. There was a shift to lower 2θ values for peaks (002) and (004), 9.1° and 18.6° respectively for $Ti_3C_2T_x$. This is caused by the etching procedure in the synthesis of $Ti_3C_2T_x$, removing the Al layers in the initial structure of the MAX phase and induction of new surface terminations in $Ti_3C_2T_x$ (T_x =−F, −O, −OH) [37,42].

As shown in Figure S5b, the FTIR spectrum of the materials exhibits two distinct regions: a 4000–1400 cm^{-1} region dominated by peaks associated with H_2O and C bond vibrations, and a 1400–400 cm^{-1} region characterized by chemical fingerprint peaks, related to C-F, Ti-F, Ti-O, and Ti-C vibrations [23]. For both materials, within the 4000–1400 cm^{-1} region, the presence of adsorbed H_2O is evidenced by the O-H stretching at 3600–3200 cm^{-1}. Additionally, the O-H bending at 1500–1300 cm^{-1} indicates the presence of -OH surface terminations. The C- bond, including C-H stretching, C=O stretching, C-O stretching, and C-H bending, are also observed in this region. For $Ti_3C_2T_x$, in the 1400–400 cm^{-1} region, the C-F stretching within 1400–1000 cm^{-1} is indicative of F surface terminations at defect sites and flake edges, and Ti-C stretching at 464 cm^{-1} was also observed in this region. Within the fingerprint region, the Ti-O bending vibrations are the most intense at 560 cm^{-1}, typically at 650–550 cm^{-1} range. The Ti-F bending, with a typical position of 1000–850 cm^{-1}, is prominent at 856 cm^{-1}. Some shifts seemed to occur due to the simultaneous presence of Ti, O, and F on the surface of $Ti_3C_2T_x$, and the presence of confined H_2O influencing the vibration fingerprint. The C-O stretching exhibits a blue shift from its regular position of 1300–1100 cm^{-1} to the 1622 cm^{-1} range [23]. These results are also consistent with previous XPS analysis of $Ti_3C_2T_x$ [22], in which the Ti 2*p* core level was deconvoluted with Ti $2p_{3/2}$ and Ti $2p_{1/2}$ peaks assigned to the presence of Ti(IV), Ti(III), and Ti(II) oxidation states. The peaks for the Ti(IV) oxidation state were more intense compared to the other oxidation states, implying a relatively higher surface atomic concentration of Ti(IV)-containing species.

The as-prepared $Ti_3C_2T_x$ suspension contains inherent polydispersity of the flakes, with a wide range of lateral sizes, as shown in Figures S4g and S4h, which yields an average of 2.05 μm. The Tyndall scattering effect by irradiation of a green laser beam through the vial of diluted 0.5 mg mL^{-1} MXene dispersion in water is clearly visible, as shown in the inset of Figure S4h. The above results confirm the successful etching of the MAX phase and synthesis of $Ti_3C_2T_x$ that was subsequently used in the genosensor application.

3.4. Analytical performance of the genosensor in real samples

Once the genosensor was fully assembled, further studies were carried out to assess its electroanalytical performance for detecting low concentrations of CBCVd in real samples (Table S1). Notably, we selected the concentration range of CBCVd, mirroring the actual expected concentrations of field-infected plants, by diluting a real total RNA hop sample of a known high concentration of CBCVd.

The performance of the genosensor was investigated by following its impedimetric response when increasing the concentration of CBCVd in a very low concentration range of 0.78–100 fg μL^{-1} (Fig. 5). The genosensor exhibited a highly linear operation in the examined concentration range with an r^2 of 0.99; the calibration curve is characterized by small standard errors for lower CBCVd concentrations and a somewhat large error bar at the highest examined concentration. This can be attributed to the saturation of the sensing surface with the analyte. In contrast, at lower concentrations, the genosensor exhibited higher reproducibility that can be attributed to the mitigated matrix effect due to dilutions of total RNA hop samples, as the real samples utilized in this study exhibited a high degree of CBCVd infection, necessitating their dilutions.

A very low limit of detection (3σ criterium) was achieved, i.e., 0.5 fg μL^{-1} (5.5 fmol L^{-1}) CBCVd. Such electroanalytical characteristics can be considered remarkable performance for a label-free sensing approach, obviating the need for an additional and time-consuming amplification step.

3.5. Reproducibility and selectivity studies

The genosensor showed good intra-day repeatability and satisfactory inter-day reproducibility. For the intra-day repeatability (n = 3), a value of 12 % was obtained at a CBCVd concentration of 6.25 fg μL^{-1}. Regarding inter-day reproducibility (n = 5), a value of 14.9 % was observed at a concentration of 1.56 fg μL^{-1}.

Finally, the selectivity study was conducted by performing EIS measurements with the newly developed genosensor incubated with solutions of (i) total RNA hop sample infected with CBCVd, (ii) viroid-free total RNA hop sample, (iii) viroid-free total RNA tomato sample, and (iv) total RNA hop sample infected with *Hop latent viroid* (HLVd). All samples had total RNA concentration of 5 ng μL^{-1}, while the CBCVd concentration in the CBCVd-infected sample was 6.25 fg μL^{-1}. In addition to a very high sensitivity, the genosensor showed a favorable selectivity, as depicted in Fig. 6.

When testing a non-infected total RNA tomato sample and a total RNA hop sample infected with HLVd, both yielded low signals compared to the CBCVd-infected hop sample with the same total RNA concentration. In contrast, a viroid-free total RNA hop sample exhibited even a negative impedimetric response, which could be due to the undefined matrix effect. Such genosensor characteristics hold great promise for its real field application to effectively monitor and control CBCVd infection in hop plants.

4. Conclusions

A sensitive and label-free genosensor for the impedimetric detection of CBCVd with good selectivity was developed. The architecture of the genosensor involves non-covalent immobilization of a biotinylated single-stranded DNA capture probe on the supporting GCE modified with a layer of streptavidin-agarose beads with incorporated 2D $Ti_3C_2T_x$ MXene electrocatalytic material. The 2D-layered $Ti_3C_2T_x$ was obtained by etching the Al layer of Ti_3AlC_2 by the HF method, with EDX spectra indicating a significant reduction of Al at% and high levels of F at%. Furthermore, XRD results indicated shifts in (002) and (004) peaks to lower 2θ values, caused by removing the Al layers in the initial structure of the MAX phase and induction of new surface terminations in $Ti_3C_2T_x$. After optimizing the fabrication and operational parameters, the synergy of the electrocatalytic MXene with other building blocks of the genosensor resulted in a low limit of detection of only 0.5 fg μL^{-1}, positioning this genosensor as a serious candidate for its on-site applications to monitor occurrence and progression of CBCVd directly in hop fields.

CRediT authorship contribution statement

Alnilan Lobato: Writing – original draft, Visualization, Methodology, Investigation, Formal analysis, Data curation, Conceptualization. **Ivan Konjević:** Visualization, Investigation, Formal analysis. **Sebastjan Radišek:** Supervision, Investigation, Funding acquisition, Formal analysis, Data curation. **Jernej Jakše:** Supervision, Investigation, Funding acquisition, Formal analysis. **Helena Volk:** Methodology, Investigation, Formal analysis, Data curation. **Monika Hermanová:** Methodology, Formal analysis. **Miroslav Fojta:** Supervision, Methodology, Funding acquisition, Formal analysis. **Jan Paštika:** Investigation, Formal analysis, Data curation. **Zdeněk Sofer:** Methodology, Investigation, Funding acquisition. **Rui Gusmão:** Writing – review & editing, Methodology, Investigation, Formal analysis, Data curation. **Samo B. Hočevar:** Writing – review & editing, Writing – original draft, Supervision, Funding acquisition. **Nikola Tasić:** Writing – review & editing, Writing

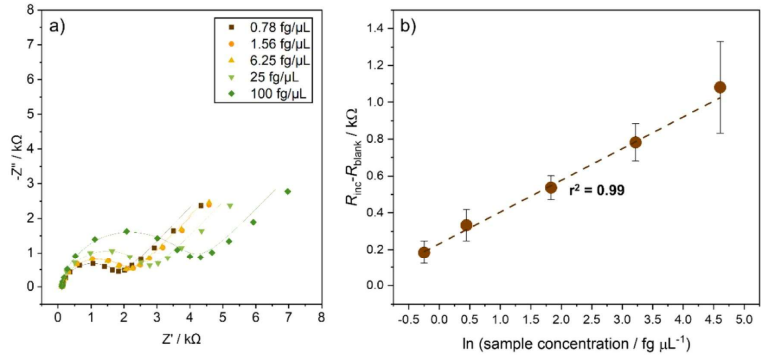


Fig. 5. (a) EIS spectra for increasing concentrations of CBCVd in real total RNA hop samples, and (b) corresponding calibration curve. The error bars represent the relative standard deviation of three independent measurements.

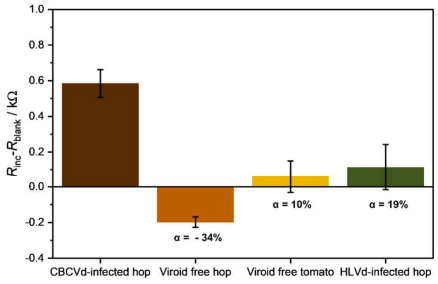


Fig. 6. Response of the genosensor in real total RNA samples containing interferents with corresponding selectivity factor values (α) calculated by dividing the analytical signal of an individual interferent by the analytical signal of the infected total RNA hop sample.

– original draft, Visualization, Supervision, Methodology, Formal analysis, Data curation.

Declaration of Competing Interest

The authors declare that they have no known competing financial interests or personal relationships that could have appeared to influence the work reported in this paper.

Acknowledgments

This research received funding from the Slovenian Research Agency: Research Program P1–0034, Program P4–0077, Research Project J1–3017, the Slovenian Research Agency's Young Researchers Program - grant agreement No. 56119, and the Czech Science Foundation project 21–46325L. The project was co-financed by the Republic of Slovenia, the Ministry of Education, Science and Sport, and the European Union under the European Regional Development Fund. Z.S. was supported by ERC-CZ program (project LL2101) from Ministry of Education Youth and Sports (MEYS) and AMULET project from Programme Johannes Amos Comenius, co-funded by EU (CZ.02.01.01/00/22_008/0004558). This work was in part supported from the grant of UCT Prague specific university research – grant No A2_FCHT_2024_076.

Appendix A. Supporting information

Supplementary data associated with this article can be found in the online version at doi:10.1016/j.snb.2024.136762.

Data Availability

Data will be made available on request. Characterization datasets generated and/or analyzed during the study are accessible via the Zenodo repository: 10.5281/zenodo.13889765.

References

[1] C. Almaguer, C. Schönberger, M. Gastl, E.K. Arendt, T. Becker, Humulus lupulus - a story that begs to be told. A review, J. Inst. Brew. 120 (2014) 289–314, https://doi.org/10.1002/jib.160.
[2] M. Karabín, T. Hudcová, L. Jelínek, P. Dostálek, Biologically active compounds from hops and prospects for their use, Compr. Rev. Food Sci. Food Saf. 15 (2016) 542–567, https://doi.org/10.1111/1541-4337.12201.
[3] J. Kubeš, Geography of world hop production 1990–2019, J. Am. Soc. Brew. Chem. 80 (2022) 84–91, https://doi.org/10.1080/03610470.2021.1880754.
[4] T.O. Diener, Viroids and the nature of viroid diseases*, in: 100 Years of Virology, Springer Vienna, Vienna, 1999, pp. 203–220, https://doi.org/10.1007/978-3-7091-6425-9_15.
[5] R. Flores, S. Minoia, A. Carbonell, A. Gisel, S. Delgado, A. López-Carrasco, B. Navarro, F. Di Serio, Viroids, the simplest RNA replicons: how they manipulate their hosts for being propagated and how their hosts react for containing the infection, Virus Res. 209 (2015) 136–145, https://doi.org/10.1016/J.VIRUSRES.2015.02.027.
[6] A. Hadidi, L. Sun, J.W. Randles, Modes of viroid transmission, Cells 11 (2022), https://doi.org/10.3390/cells11040719.
[7] N. Duran-Vila, C.N. Roistacher, R. Rivera-Bustamante, J.S. Semancik, A definition of citrus viroid groups and their relationship to the exocortis disease, J. Gen. Virol. 69 (1988) 3069–3080, https://doi.org/10.1099/0022-1317-69-12-3069.
[8] H. Puchta, K. Ramm, R. Luckinger, R. Hadas, M. Bar-Joseph, H.L. Saänger, Primary and secondary structure of citrus viroid IV (CVd IV), a new chimeric viroid present in dwarfed grapefruit in Israel, Nucleic Acids Res. 19 (1991), https://doi.org/10.1093/nar/19.23.6640.
[9] J. Jakse, S. Radisek, T. Pokorn, J. Matousek, B. Javornik, Deep-sequencing revealed Citrus bark cracking viroid (CBCVd) as a highly aggressive pathogen on hop, Plant Pathol. 64 (2015) 831–842, https://doi.org/10.1111/PPA.12325.
[10] EPPO, Citrus Bark Cracking Viroid, EPPO datasheets on pests recommended for regulation, ⟨Https://Gd.Eppo.Int/Taxon/CBCVD0/Datasheet⟩ (2024).
[11] M. Eiras, A.M. de Oliveira, A. de Fátima Ramos, R. Harakava, J.-A. Daròs, First report of citrus bark cracking viroid and hop latent viroid infecting hop in commercial yards in Brazil, 603–603, J. Plant Pathol. 105 (2023), https://doi.org/10.1007/s42161-023-01313-4.
[12] P. Baldi, N. La Porta, Molecular approaches for low-cost point-of-care pathogen detection in agriculture and forestry, Front. Plant Sci. 11 (2020) 1603, https://doi.org/10.3389/FPLS.2020.570862/BIBTEX.

[13] F. Martinelli, R. Scalenghe, S. Davino, S. Panno, G. Scuderi, P. Ruisi, P. Villa, D. Stroppiana, M. Boschetti, L.R. Goulart, C.E. Davis, A.M. Dandekar, Advanced methods of plant disease detection. A review, Agron. Sustain Dev. 35 (2015) 1–25, https://doi.org/10.1007/s13593-014-0246-1.
[14] Z. Zhang, S. Li, Detection of Viroids, in: Fundamentals of Viroid Biology, Elsevier, 2024, pp. 297–321, https://doi.org/10.1016/B978-0-323-99688-4.00017-1.
[15] A. Mokhtarzadeh, R. Eivazzadeh-Keihan, P. Pashazadeh, M. Hejazi, N. Gharaatifar, M. Hasanzadeh, B. Baradaran, M. de la Guardia, Nanomaterial-based biosensors for detection of pathogenic virus, TrAC Trends Anal. Chem. 97 (2017) 445–457, https://doi.org/10.1016/J.TRAC.2017.10.005.
[16] E. Cesewski, B.N. Johnson, Electrochemical biosensors for pathogen detection, Biosens. Bioelectron. 159 (2020) 112214, https://doi.org/10.1016/J.BIOS.2020.112214.
[17] S.S. Low, H.S. Loh, J.S. Boey, P.S. Khiew, W.S. Chiu, M.T.T. Tan, Sensitivity enhancement of graphene/zinc oxide nanocomposite-based electrochemical impedance genosensor for single stranded RNA detection, Biosens. Bioelectron. 94 (2017) 365–373, https://doi.org/10.1016/J.BIOS.2017.02.038.
[18] Y. Wang, W. Wang, X. Lu, T. Chen, Y. Wang, Y. Wen, J. Hu, J. Song, X. Wang, Novel RNA genosensor based on highly stable gold nanoparticles decorated phosphorene nanohybrid with graphene for highly sensitive and low-cost electrochemical detection of coconut cadang-cadang viroid, Microchim. Acta 191 (2024), https://doi.org/10.1007/s00604-023-06130-1.
[19] N. Štajner, S. Radišek, A.K. Mishra, V.S. Nath, J. Matoušek, J. Jakše, Evaluation of disease severity and global transcriptome response induced by Citrus bark cracking viroid, Hop latent viroid, and their co-infection in hop (Humulus lupulus L.), Int. J. Mol. Sci. 20 (2019), https://doi.org/10.3390/ijms20133154.
[20] B. Kump, B. Javornik, Evaluation of genetic variability among common buckwheat (Fagopyrum esculentum Moench) populations by RAPD markers, Plant Sci. 114 (1996) 149–158, https://doi.org/10.1016/0168-9452(95)04321-7.
[21] A. Sečnik, S. Radišek, N. Štajner, J. Jakše, Studying strands polarity of different viroids and their combinations in infected hop plants, Acta Agric. Slov. 115 (2020) 193–201, https://doi.org/10.14720/AAS.2020.115.1.1319.
[22] J. Isailović, A. Oberlintner, U. Novak, M. Finšgar, F.M. Oliveira, J. Paštika, Z. Sofer, N. Tasić, R. Gusmão, S.B. Hočevar, Study of chitosan-stabilized $Ti_3C_2T_x$ MXene for ultrasensitive and interference-free detection of gaseous H_2O_2, ACS Appl. Mater. Interfaces 15 (2023) 31643–31651, https://doi.org/10.1021/acsami.3c05314.
[23] T. Parker, D. Zhang, D. Bugallo, K. Shevchuk, M. Downes, G. Valurouthu, A. Inman, B. Chacon, T. Zhang, C.E. Shuck, Y.J. Hu, Y. Gogotsi, Fourier-transform infrared spectral library of MXenes, Chem. Mater. 17 (2024) 8437–8446, https://doi.org/10.1021/acs.chemmater.4c01536.
[24] X. Meng, D. O'Hare, S. Ladame, Surface immobilization strategies for the development of electrochemical nucleic acid sensors, Biosens. Bioelectron. (2023) 115440, https://doi.org/10.1016/j.bios.2023.115440.
[25] A. Holmberg, A. Blomstergren, O. Nord, M. Lukacs, J. Lundeberg, M. Uhlén, The biotin-streptavidin interaction can be reversibly broken using water at elevated temperatures, Electrophoresis 26 (2005) 501–510, https://doi.org/10.1002/elps.200410070.
[26] J. Tse, Y. Wang, T. Zengeya, E. Rozners, A. Tan-Wilson, Peptide nucleic acid probe for protein affinity purification based on biotin–streptavidin interaction and peptide nucleic acid strand hybridization, Anal. Biochem 470 (2015) 34–40, https://doi.org/10.1016/j.ab.2014.10.005.
[27] Q. Guo, J.-J. Han, S. Shan, D.-F. Liu, S.-S. Wu, Y.-H. Xiong, W.-H. Lai, DNA-based hybridization chain reaction and biotin–streptavidin signal amplification for sensitive detection of Escherichia coli O157:H7 through ELISA, Biosens. Bioelectron. 86 (2016) 990–995, https://doi.org/10.1016/j.bios.2016.07.049.
[28] H. Yin, H. Wang, W. Jiang, Y. Zhou, S. Ai, Electrochemical immunosensor for N6-methyladenosine detection in human cell lines based on biotin-streptavidin system and silver-SiO_2 signal amplification, Biosens. Bioelectron. 90 (2017) 494–500, https://doi.org/10.1016/j.bios.2016.10.066.
[29] C. Ling, L. Shi, Y. Ouyang, J. Wang, Searching for highly active catalysts for hydrogen evolution reaction based on O-terminated MXenes through a simple descriptor, Chem. Mater. 28 (2016) 9026–9032, https://doi.org/10.1021/acs.chemmater.6b03972.
[30] X. An, W. Wang, J. Wang, H. Duan, J. Shi, X. Yu, The synergetic effects of Ti_3C_2 MXene and Pt as co-catalysts for highly efficient photocatalytic hydrogen evolution over g-C_3N_4, Phys. Chem. Chem. Phys. 20 (2018) 11405–11411, https://doi.org/10.1039/C8CP01123K.
[31] Y. Xie, Y. Dall'Agnese, M. Naguib, Y. Gogotsi, M.W. Barsoum, H.L. Zhuang, P.R. C. Kent, Prediction and characterization of MXene nanosheet anodes for non-lithium-ion batteries, ACS Nano 8 (2014) 9606–9615, https://doi.org/10.1021/nn503921j.
[32] M. Naguib, J. Halim, J. Lu, K.M. Cook, L. Hultman, Y. Gogotsi, M.W. Barsoum, New two-dimensional Niobium and vanadium carbides as promising materials for Li-Ion batteries, J. Am. Chem. Soc. 135 (2013) 15966–15969, https://doi.org/10.1021/ja405735d.
[33] A. Junkaew, R. Arróyave, Enhancement of the selectivity of MXenes (M_2C, M = Ti, V, Nb, Mo) *via* oxygen-functionalization: promising materials for gas-sensing and -separation, Phys. Chem. Chem. Phys. 20 (2018) 6073–6082, https://doi.org/10.1039/C7CP08622A.
[34] M. Lian, Y. Shi, L. Chen, Y. Qin, W. Zhang, J. Zhao, D. Chen, Cell membrane and V_2C MXene-based electrochemical immunosensor with enhanced antifouling capability for detection of CD44, ACS Sens. (2022), https://doi.org/10.1021/acssensors.2c01215.
[35] H. Wang, J. Sun, L. Lu, X. Yang, J. Xia, F. Zhang, Z. Wang, Competitive electrochemical aptasensor based on a cDNA-ferrocene/MXene probe for detection of breast cancer marker Mucin1, Anal. Chim. Acta 1094 (2020) 18–25, https://doi.org/10.1016/j.aca.2019.10.003.
[36] A. Sinha, Dhanjai, H. Zhao, Y. Huang, X. Lu, J. Chen, R. Jain, MXene: an emerging material for sensing and biosensing, TrAC Trends Anal. Chem. 105 (2018) 424–435, https://doi.org/10.1016/j.trac.2018.05.021.
[37] A.A. Emerenciano, R.M. do Nascimento, A.P.C. Barbosa, K. Ran, W.A. Meulenberg, J. Gonzalez-Julian, Ti_3C_2 MXene membranes for gas separation: influence of heat treatment conditions on D-spacing and surface functionalization, Membrane 12 (2022) 1025, https://doi.org/10.3390/membranes12101025.
[38] T. Hu, M. Hu, B. Gao, W. Li, X. Wang, Screening surface structure of MXenes by high-throughput computation and vibrational spectroscopic confirmation, J. Phys. Chem. C 122 (2018) 18501–18509, https://doi.org/10.1021/acs.jpcc.8b04427.
[39] A. Sarycheva, Y. Gogotsi, Raman spectroscopy analysis of the structure and surface chemistry of $Ti_3C_2T_x$ MXene, Chem. Mater. 32 (2020) 3480–3488, https://doi.org/10.1021/acs.chemmater.0c00359.
[40] J. Azadmanjiri, J. Regner, L. Děkanovský, B. Wu, J. Luxa, Z. Sofer, Powering the future: unleashing the potential of MXene-based dual-functional photoactive cathodes in photo-rechargeable zinc-ion capacitor, Small (2023) 2305972, https://doi.org/10.1002/smll.202305972.
[41] L. Chaput, G. Hug, P. Pecheur, H. Scherrer, Thermopower of the 312 MAX phases Ti_3SiC_2, Ti_3GeC_2, and Ti_3AlC_2, Phys. Rev. B Condens Matter Mater. Phys. 75 (2007) 035107, https://doi.org/10.1103/PhysRevB.75.035107.
[42] M. Alhabeb, K. Maleski, B. Anasori, P. Lelyukh, L. Clark, S. Sin, Y. Gogotsi, Guidelines for synthesis and processing of two-dimensional titanium carbide ($Ti_3C_2T_x$ MXene), Chem. Mater. 29 (2017) 7633–7644, https://doi.org/10.1021/acs.chemmater.7b02847.

Alnilan Lobato is a Ph.D. student of Sensor Technologies at the International Postgraduate School Jožef Stefan and a young researcher at the Department of Analytical Chemistry, National Institute of Chemistry, Ljubljana, Slovenia. She obtained her MSc from the Chemistry Institute of the University of São Paulo (USP) in 2021 and her BSc in Bioprocesses Engineering and Biotechnology from the State University of Rio Grande do Sul (UERGS) in 2019. Her research interests include electrochemical sensors and genosensors, and molecularly imprinted polymers.

Ivan Konjević is a Ph.D. student at the Faculty of Chemistry and Chemical Technology, University of Ljubljana. He obtained his MSc in Chemistry from the University of Maribor, Slovenia, in 2023, and BSc in Quality Control and Environmental Protection from the University of Sarajevo, Bosnia&Herzegovina, in 2019. His research interests include electrochemical sensors and genosensors, and application of electrochemistry for the atmospheric studies.

Sebastjan Radišek received his Ph.D. in 2004 at the University of Ljubljana, Biotechnical Faculty. Currently, he is the Head of the Plant Protection Laboratory, at the Slovenian Institute for Hop Research and Brewing, Žalec, Slovenia. His research interests include molecular markers, plant breeding, plant biotechnology, and phytopathology. He published more than 70 articles, with over 850 citations, with an h-index of 17.

Jernej Jakše received his Ph.D. in 2003 at the University of Ljubljana, Biotechnical Faculty. He is a Full Professor at the same faculty, and his research interests include plant genetics, molecular markers, DNA sequencing, next generation sequencing, and bioinformatics. He published more than 130 articles, with over 3500 citations, with an h-index of 34.

Helena Volk received her Ph.D. in 2019 at the University of Ljubljana, Biotechnical Faculty, Department of Agronomy. She currently works as a Teaching Assistant at the same faculty. Her research interests include genetics, biotechnology, statistics, and plant breeding.

Monika Hermanová received her Ph.D. in 2018 at the Masaryk University, Faculty of Science, Department of Experimental Biology. She currently works at the Department of Biophysical Chemistry and Molecular Oncology, Institute of Biophysics ASCR. Her research encompasses the fields of electrochemistry, biochemistry and analytical chemistry.

Miroslav Fojta studied biochemistry at the Charles University in Prague and earned his PhD (1995) in biophysics at IBP CAS, with Prof. E. Paleček. In 2005, he became the head of the DBCMO and finished his habilitation at the Masaryk University in Brno, where he was a group leader at the Central European Institute of Technology in 2011–2020. His research interests include electrochemistry of nucleic acids, chemical modification of biopolymers, and its application in the analysis of nucleotide sequences, DNA damage, and protein-DNA interactions.

Jan Paštika is a Ph.D. student at the Department of Inorganic Chemistry at the University of Chemistry and Technology in Prague, Czech Republic. He has published nine articles in peer reviewed journals, and his research interests include the synthesis and characterization of 2D layered materials.

Zdeněk Sofer has been a Full Professor at the University of Chemistry and Technology in Prague, Czech Republic, since 2018. He also received his Ph.D. from the University of Chemistry and Technology in Prague in 2008. During his Ph.D., he spent one year at Forschungszentrum Julich (Peter Grünberg Institute, Germany), followed by postdoctoral

experience in Germany. He is an Associated Editor of FlatChem journal. He has published more than 600 articles, which received almost 30,000 citations (h-index 88). His research interests include the synthesis of semiconductors and 2D materials, chemical modifications, and electrochemistry.

Rui Gusmao obtained his Ph.D. in Chemistry from the University of Barcelona, Spain, in 2012. As a postdoctoral researcher, he worked in Portugal at the University of Porto (2012–2013) and the University of Minho (2013–2016), followed by a position at Nanyang Technological University, Singapore (2016–2017). Since 2018, he has been a senior scientist at the Department of Inorganic Chemistry of the University of Chemistry and Technology in Prague, Czech Republic. In 2020 he received financial support under the GACR Jr program. He has published over 50 articles in peer-reviewed journals and has an h-index of 23. His current research interests include the electrochemical applications of 2D layered materials.

Samo B. Hočevar received a Ph.D. in Analytical Chemistry in 2002 from the Faculty of Chemistry and Chemical Technology, University of Ljubljana, Ljubljana, Slovenia. Presently, he is the Head of the Department of Analytical Chemistry at the National Institute of Chemistry. His research interests include the development, study, miniaturization, and application of advanced electrochemical sensors, gas sensors, and biosensors.

Nikola Tasić is a Research Assistant Professor at the Department of Analytical Chemistry, National Institute of Chemistry, Ljubljana, Slovenia. He received both a MSc in Biochemical Engineering and Biotechnology and a Ph.D. in Materials Science and Engineering from the Faculty of Technology and Metallurgy, University of Belgrade, Belgrade, Serbia. He worked as a post-doctoral researcher at the Chemistry Institute, University of São Paulo, São Paulo, Brazil. His current research topics include the design and optimization of new methodologies applicable in point-of-need electrochemical biosensing, genosensing, immunosensing, and gas sensing.

Chapter 4

Conclusions

The aim of this dissertation was to investigate and develop innovative approaches for the electrochemical detection of viruses and viroids, with a particular focus on Severe Acute Respiratory Syndrome Coronavirus 2 and *Citrus bark cracking viroid*. As part of this work, new materials, immobilization strategies, and sensing platforms were investigated to develop sensitive, reproducible, and practical biosensors. The primary goals were successfully achieved, and all five hypotheses proposed were confirmed. Overall, three impedimetric biosensors were developed, each addressing specific challenges in electrochemical biosensing related to reproducibility, sensitivity, and real-sample application.

4.1 Principal Advancements and Scientific Contributions

This study advances the field of electrochemical biosensing by addressing critical challenges related to electrode reproducibility, biocompatibility and detection of real samples. A key contribution was demonstrating that SPCEs can be reproducible for biosensing applications by surface modification with biocompatible materials such as gelatin. The introduction of gelatin membranes stabilized the electrode surface and enabled efficient and oriented immobilization of antibodies, significantly improving the electrochemical performance of SPCE-based biosensors.

Another important achievement was the development of a label-free electrochemical genosensor capable of detecting CBCVd directly from real total RNA samples without the need for nucleic acid amplification. This is the first reported use of an electrochemical sensor for viroid detection in real samples and a significant step forward in plant pathogen diagnostics. The research has also expanded the understanding of 2D MXenes as promising catalytic and signal-amplifying materials for electrochemical biosensing and provided insights into their capabilities and limitations in complex biological environments.

Finally, by integrating strategies for surface modification, signal amplification and analysis of real samples, this dissertation lays the foundation for developing decentralized, rapid and reliable diagnostic tools that address urgent human health and agriculture needs.

4.2 Experimental Insights and Hypothesis Validation

The findings of this dissertation align closely with the hypotheses initially proposed:

- **Hypothesis 1:** Screen-printed electrodes can serve as supporting electrodes for sensitive and reproducible biosensors after appropriate pre-treatment, despite their

innate irreproducibility; the introduction of gelatin can improve the electrochemical reproducibility of screen-printed carbon electrodes; a stable and biocompatible modifying layer of gelatin will allow for the immobilization of biological recognition elements, such as anti-SARS-CoV-2 antibodies.

This hypothesis was confirmed through the application of gelatin on screen-printed carbon electrodes. Gelatin provided a uniform, biocompatible, and stabilizing environment for biomolecule immobilization, significantly improving the electrochemical reproducibility of the electrodes. Through careful pre-treatment and functionalization, SPCEs have proven to be reliable platforms for biosensor construction.

- **Hypothesis 2:** Electrochemical immunosensors based on the stable gelatin membrane can sensitively and selectively detect the SARS-CoV-2 spike protein in artificial nasopharyngeal fluid.

Experimental results confirmed this hypothesis. The gelatin-based electrochemical immunosensor achieved sensitive and selective detection of the SARS-CoV-2 spike protein in ANF. Detection limits were within clinically relevant ranges, and the sensor exhibited high specificity against non-target proteins, with minimal cross-reactivity, highlighting its potential for real-world applications.

- **Hypothesis 3:** The streptavidin-agarose layer can serve as a suitable immobilization layer for the biological recognition element on the glassy carbon electrode. In addition, the streptavidin-biotin interaction can be used as a suitable way to immobilize a single-stranded biotinylated DNA capture probe that is highly specific for the target sequence of *Citrus bark cracking viroid*.

This hypothesis was successfully confirmed. The streptavidin-agarose layer provided a stable and effective immobilization matrix for the biotinylated ssDNA capture probe on the GCE. The high affinity of the streptavidin-biotin interaction enabled robust attachment of the capture probe, facilitating successful hybridization with the complementary target sequence from CBCVd RNA.

- **Hypothesis 4:** 2D-laminated (electro)catalytic MXenes can be used as a transducing surface in biosensing due to their easy functionalization and can enhance and/or stabilize the analytical signal of an electrochemical genosensor for *Citrus bark cracking viroid*.

Integration of $Ti_3C_2T_x$ MXenes into the sensing architecture validated this hypothesis. The MXene-modified sensors showed enhanced electrochemical communication between the electrode and the sensing layer, resulting in improved signal-to-noise ratios and a lower limit of detection for CBCVd RNA targets. The material's high conductivity and surface reactivity significantly contributed to sensor performance.

- **Hypothesis 5:** The proposed electrochemical genosensor containing a streptavidin-agarose layer and (electro)catalytic MXenes can be used for interference-free detection of *Citrus bark cracking viroid* in real total RNA samples.

This hypothesis was also confirmed. Despite the complexity and potential interference associated with total RNA samples, the developed genosensor, through the combined use

of streptavidin-agarose and MXenes, enabled consistent, interference-free detection of CBCVd.

In support of the validation of these hypotheses, several experimental insights were gained throughout the course of this work.

The working electrodes available for sensor fabrication were carefully assessed. Carbon-based electrodes, specifically GCEs and SPCEs, were selected because of their versatile electrochemical properties that are highly compatible with impedimetric measurements using redox probe. For the detection of SARS-CoV-2, SPCEs were ultimately favored. Their low cost, rapid response time, and portability made them particularly well suited for the development of on-site diagnostic tools.

Strategies for immobilizing biological recognition elements were explored extensively. In the development of the first immunosensor, gelatin was successfully employed as a membrane for protein immobilization. Protein A was covalently bound to the gelatin membrane through carbodiimide crosslinking chemistry. This method enabled the oriented and stable immobilization of anti-SARS-CoV-2 antibodies, confirming that properly pre-treated SPCEs could indeed serve as reliable and reproducible biosensor platforms, in accordance with the first hypothesis.

In an alternative immunosensor design, Nafion was used as the immobilization matrix to embed V_2CT_x MXene material. Glutaraldehyde served as the crosslinking agent to stabilize Protein A on the electrode surface. This approach also enabled effective antibody immobilization, further supporting the concept that surface modification strategies can significantly improve biosensor performance.

For the development of the genosensor for detecting *Citrus bark cracking viroid*, a glassy carbon electrode was selected. The GCE offered superior electrochemical stability and reproducibility, making it an excellent choice for pioneering an electrochemical sensor targeting a viroid. A streptavidin-agarose layer was applied onto the electrode, and the strong affinity between streptavidin and biotin was exploited to immobilize a biotinylated single-stranded DNA capture probe. This probe was specifically designed to hybridize with a complementary sequence within the CBCVd genome. The successful immobilization and hybridization process confirmed the third hypothesis regarding the effectiveness of the streptavidin-agarose system.

To further enhance the performance of the genosensor, $Ti_3C_2T_x$ MXene material was incorporated into the sensor design. The excellent electrical conductivity of MXenes facilitated efficient electron transfer between the sensing layer and the electrode surface, improving the sensitivity and signal stability of the device. This validated the fourth hypothesis, demonstrating the advantageous role of MXenes as transducing materials in biosensing applications.

The proposed genosensor configuration, combining streptavidin-agarose layers and MXene nanomaterials, proved capable of detecting CBCVd in complex real samples of total RNA extracts. Despite the inherent challenges associated with biological sample complexity, careful standardization of RNA extraction and denaturation protocols enabled consistent and interference-free detection, thereby confirming the fifth hypothesis.

Throughout all stages of sensor development and testing, quantitative results provided strong support for hypothesis validation. Calibration curves showed excellent linearity, detection limits were within acceptable thresholds for practical applications, and interference assays confirmed the high specificity of the biosensors against interferents. The data consistently demonstrated that the developed sensors were able to achieve the sensitivity, reproducibility, and practical applicability targeted at the onset of this research.

4.3 Study Limitations and Technical Challenges

While this work's results are promising, there are still some limitations and technical challenges, both for this particular study and for the development of biosensors in general.

One major problem is the long-term stability of MXene materials. Although MXenes have shown excellent electrical properties and catalytic behavior, their long-term stability under physiological and environmental conditions remains a concern. Their sensitivity to oxidation, especially under ambient or biological conditions, threatens the sensors' shelf life and operational reliability. Without effective strategies to improve their durability, the performance of MXene-based sensors can degrade over time, limiting their practical usability.

Another significant challenge lies in the complexity of raw biological samples such as human serum or plant RNA extracts. In contrast to purified analytes tested under controlled conditions, these samples are subject to complications such as non-specific adsorption (biofouling), matrix interference and signal suppression. Even if sensors show excellent analytical performance under controlled laboratory conditions, transferring this performance to real samples is far from easy. Biofouling leads to unwanted deposition of proteins or other biomolecules on the sensor surface, which can obscure detection signals and reduce sensitivity and specificity. In addition, interfering substances and the intrinsic properties of analytes (such as their size, structural complexity or conformational instability) can affect the sensor's functionality due to steric hindrances or unfavorable binding interactions.

Another challenge for electrochemical biosensors is their stability, reproducibility and scalability during production. Precise functionalization of electrode surfaces remains a persistent obstacle, as slight variations in surface chemistry or bioreceptor immobilization of bioreceptors can lead to inconsistent performance. To facilitate commercialization, standardized protocols and advanced characterization techniques are essential to ensure the reliability of production batches and research laboratories.

In addition, developing electrochemical immuno- and genosensors often involves using expensive and sensitive biological recognition elements such as antibodies, enzymes or nucleic acids. Maintaining the activity and stability of these biomolecules over a long period of time and under different storage and operating conditions is a constant challenge. In contrast to simpler colorimetric devices, the setup and calibration of electrochemical biosensors can be relatively complex and requires precise control of experimental conditions such as temperature, ionic strength and pH. This added complexity can limit accessibility for end users without specialized training.

Scalability and mass production also present technical obstacles. While many biosensors work great at the prototype level, scaling manufacturing without compromising sensitivity, specificity, and reliability is challenging. Factors such as batch-to-batch variability, cost-effective integration of microfluidics, and miniaturization of supporting electronics must be considered for successful industrial implementation.

Environmental robustness is another critical factor, as these sensors are susceptible to temperature fluctuations, humidity and physical stress, conditions common outside laboratories. Ensuring consistent performance under such variable conditions is critical for use in the field, from point-of-care diagnostics to environmental monitoring. These environmental factors can lead to a deviation in the electrochemical signal or degradation of the biological components, making storing and using these devices outside of controlled laboratory environments difficult.

Finally, regulatory approval and clinical validation pose further difficulty. Developing biosensors that meet stringent medical or agricultural diagnostics standards requires extensive testing and validation, which can be both time-consuming and costly.

4.4 Opportunities for Development and Innovation

The course of this dissertation opens up several promising opportunities for future research, technical refinement, and practical application.

One important area for further development is to improve the oxidative stability and biocompatibility of MXene materials. Future studies could focus on developing protective surface coatings, the development of composites that combine MXenes with more stable polymers or nanomaterials, or doping MXene structures with specific elements to improve their chemical resistance. These measures can significantly extend the functional lifetime of MXene-based biosensors and improve their reliability when exposed to complex biological samples over a long period.

Another promising direction is the integration of simplified, portable RNA extraction protocols into the developed genosensor systems, perhaps even in combination with microfluidic systems. While most current methods for nucleic acid extraction are effective, they often require laboratory infrastructure and skilled personnel, which limits the use of on-site biosensors. By integrating on-chip or cartridge-based RNA extraction solutions, it will be possible to develop stand-alone diagnostic systems that allow users to collect, process and analyze samples outside of laboratories. In parallel, coupling biosensors with portable, wireless, battery-powered electrochemical readers could provide a powerful platform for real-time monitoring of pathogens in various environments, from clinical facilities to agricultural fields.

Another significant opportunity is the development of continuous monitoring platforms. In plant health monitoring, the implantation of biosensors in soil probes, irrigation systems, or plant tissue could allow real-time surveillance of the spread of viruses and viroids in agricultural areas. Developing such systems could help detect disease outbreaks early, improve disease control strategies, and protect food production from new biological threats.

An important goal is further developing biosensor platforms that enable the simultaneous detection of multiple targets, i.e., multiplexed analysis. Rather than focusing on identifying a single pathogen per test, biosensors can be designed to detect many analytes simultaneously by integrating different elements of biological detection into a single sensor platform. Such an approach has already been tested in detecting viruses [109] and has been shown to provide comprehensive diagnostic information with minimal sample volume and processing time. This method increases efficiency and is particularly valuable for monitoring co-infections or conducting large-scale surveillance. Further research to develop robust and user-friendly multiplex electrochemical biosensors is essential for future diagnostic and biosafety requirements.

One promising possibility is to extend the application of the developed strategies to viral and viroid threats other than SARS-CoV-2 and CBCVd. By designing and adapting biorecognition elements tailored to emerging human, animal or plant pathogens, the biosensor platforms developed in this dissertation can be adapted to respond effectively to future outbreaks.

Portable electrochemical biosensor platforms show great commercial potential, and multiple companies are making progress in that field. However, for the technology to be viable, it is essential to understand regulatory requirements, optimize manufacturing and standardization processes, and design user-friendly devices that require minimal training.

The research conducted in this dissertation provides a solid foundation for scientific advances and practical applications that address pressing global needs. The opportunities for development and innovation are rich and diverse, providing clear pathways to enhance diagnostic capabilities in multiple areas and contributing meaningfully to public health, food security, and environmental sustainability. Future work needs to focus not only on improving analytical performance but also on improving robustness, reproducibility, ease of use, and scalability to ensure real-world impact.

4.5 Final Remarks

The findings of this dissertation demonstrate how electrochemical biosensors show great potential for fast and decentralized viral and viroid detection with high sensitivity. The innovations presented here contribute to a broader shift towards accessible, point-of-care diagnostic technologies. The biosensor platforms developed in this dissertation show promise, but their final success depends on solving several complex challenges. Current advancements in materials science, sensor design, and electrochemical detection methods assist in overcoming these impediments.

Future research should balance fundamental advances with practical considerations, focusing on improving analytical performance, durability, and scalability. By systematically addressing these limitations, we can fully realize the potential of electrochemical biosensors and bridge the gap between laboratory research and practical applications.

Ultimately, this work demonstrates that with careful design and appropriate material selection, electrochemical biosensors can indeed be powerful tools for infectious disease and plant health management that benefit public health and agricultural productivity. We hope that the knowledge and methods developed in this work will serve as a foundation for further research and innovation in the field of electrochemical biosensing.

Appendix A

Supporting Information

A.1 Supporting Information for Manuscript 1

SUPPORTING INFORMATION

Development of a simple gelatin-based sensing platform for the sensitive label-free impedimetric detection of SARS-CoV-2

Alnilan Lobato,[1,2] Maja Šubic,[1] Tea Romih,[1] Lea Žibret,[1] Dino Metarapi,[1] Mojca Benčina,[3] Roman Jerala,[3] Kristijan Vidović,[1] Samo B. Hočevar,[1,*] and Nikola Tasić[1,*]

[1]*Department of Analytical Chemistry, National Institute of Chemistry, Ljubljana, Slovenia*
[2]*International Postgraduate School Jožef Štefan, Ljubljana, Slovenia*
[3]*Department of Synthetic Biology and Immunology, National Institute of Chemistry, Ljubljana, Slovenia*

Deposition of the gelatin onto screen-printed carbon electrodes (SPCEs) was performed by drop-casting method, from the solution also containing glycerol in a small percentage, which acts as the rheological agent to ensure complete distribution of the gelatin solution over the electrode and satisfactory thickness homogeneity of the final layer. Apart from the functionality and biocompatibility reasons explained in the manuscript, the modification of the SPCEs by depositing a gelatin layer also positively affected the innate irreproducibility of the SPECs. For the sensing applications, which are usually performed on several replicates, only the supporting electrodes that exhibit comparable and reproducible electrochemical signals obtained by simple heterogeneous electron transfer (HET) tests can be further employed for constructing the biosensors. Unlike the solid-state polishable electrodes, which are easier to maintain via electrochemical and mechanical protocols in order to assure satisfactory repeatability and reproducibility throughout their usage, printed electrodes are mostly limited to a single use in the as-

received state. Conventional voltammetric cycling in acidic or alkaline solutions is limited to just a few cycles, owing to the typical instability of the silver-printed pseudoreference electrode. For this reason, such electrochemical pretreatment is avoided or performed by connecting only the working electrode of the SPCE in combination with conventional counter and reference electrodes. Alternatively, oxygen plasma treatment might be a promising approach for stabilizing screen-printed electrodes, also positively affecting protein molecule adsorption in further applications. Here we show that the introduction of gelatin hydrogel is another viable approach.

Recorded EIS spectra and fitting parameters are presented in **Figure S1** and **Table S1**, respectively. Results obtained using bare SPCEs were fitted with the Randles equivalent circuit ($\chi^2_{average}$=7.45e-4), whereas an additional small high-frequency semicircle in the Nyquist diagrams ($\chi^2_{average}$=6.42e-5), fitted by the resistor-constant phase element pair, has described the introduction of gelatin.

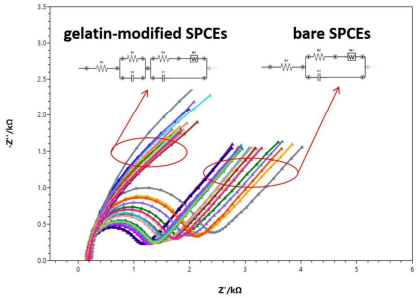


Figure S1. EIS spectra recorded on bare SPCEs and gelatin-modified SPCEs. The inset shows the equivalent electrical circuits used to fit data.

Table S1. Fitting parameters obtained for EIS measurements in 1.0 mM $[Fe(CN)_6]^{3-/4-}$ redox probe in 0.1 M KCl on bare SPCE and gelatin-modified SPCE.

	SPCE	SPCE/gelatine
R 1	170.42 ± 2.81	166.16 ± 3.13
R 2		41.09 ± 2.51
Q 1		539.52 ± 64.18
n 1		0.63 ± 0.01
R 3	1291.64 ± 68.87	1285.61 ± 47.59
W 1	1.34 ± 0.01	1.30 ± 0.04
C 1	794.77 ± 5.77	2.35E+05 ± 5.92E+03

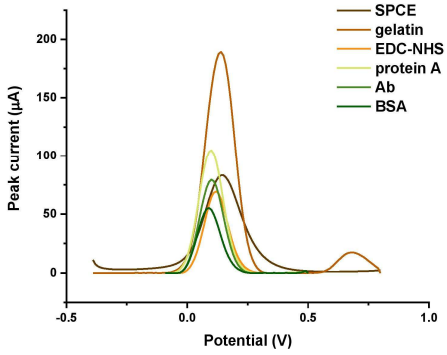


Figure S2. SWVs for each fabrication step of the immunosensor.

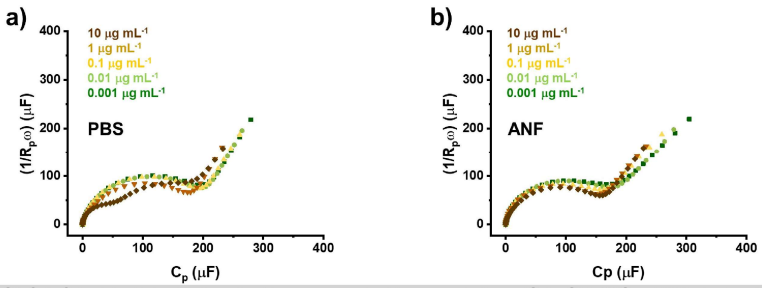


Figure S3. Cole-Cole plots obtained for impedimetric measurements of low concentrations of Spike S1 in PBS and ANF, clearly exhibiting the diffusion contribution.

Table S2. Fitting parameters obtained for the incubation time study. Raw impedance data were fitted using the equivalent circuit: R_s-(R_{gel}||Q_1)-((R_{ct}*W*)||C_1).

Incubation time	Rs, Ω	Rgel, Ω	Q1, µT	n, ϕ	Rct, Ω	W, kσ	C1, nF	χ^2
blanks 15 min	136.90 ± 6.39	128.27 ± 6.53	652.63 ± 158.24	0.57 ± 0.04	4649.33 ± 295.58	2.64 ± 0.25	224300.00 ± 4216.63	8.76E-05
15 min	151.30 ± 6.23	291.80 ± 17.96	179.03 ± 12.48	0.92 ± 0.01	5979.33 ± 531.46	3.51 ± 0.25	202100.00 ± 5359.73	2.67E-04
blanks 30 min	143.57 ± 9.32	97.42 ± 6.49	454.70 ± 21.82	0.69 ± 0.02	4032.67 ± 253.71	2.83 ± 0.10	227800.00 ± 7341.81	2.72E-05
30 min	150.90 ± 5.84	250.80 ± 14.20	204.20 ± 14.21	0.88 ± 0.01	5588.00 ± 91.33	3.40 ± 0.08	216066.67 ± 10837.42	1.07E-04
blanks 45 min	155.13 ± 1.96	102.71 ± 1.67	459.17 ± 27.46	0.69 ± 0.01	3721.67 ± 232.16	2.84 ± 0.15	211366.67 ± 9051.01	1.81E-04
45 min	166.23 ± 7.53	370.43 ± 13.13	184.17 ± 20.65	0.94 ± 0.03	7378.33 ± 785.04	4.03 ± 0.32	207166.67 ± 5477.70	1.67E-04
blanks 60 min	140.37 ± 8.45	109.30 ± 3.72	520.30 ± 32.04	0.65 ± 0.00	4244.00 ± 319.74	2.93 ± 0.25	213500.00 ± 8815.64	6.71E-05
60 min	147.63 ± 8.15	368.13 ± 24.50	171.10 ± 9.99	0.94 ± 0.01	6932.67 ± 44.91	3.72 ± 0.27	207833.33 ± 6750.36	1.89E-04
blanks 120 min	147.77 ± 1.84	104.90 ± 2.00	507.03 ± 23.23	0.66 ± 0.01	4265.33 ± 130.80	3.09 ± 0.14	219133.33 ± 4454.79	5.74E-05
120 min	166.23 ± 7.53	370.43 ± 13.13	184.17 ± 20.65	0.94 ± 0.03	7378.33 ± 785.04	4.03 ± 0.32	207166.67 ± 5477.70	1.67E-04

Table S3. Fitting parameters obtained for the BSA blocking time study. Raw impedance data were fitted using the equivalent circuit: R_s-(R_{gel}||Q_1)-(($R_{ct}$$W$)||$C_1$).

BSA time	Rs, Ω	Rgel, Ω	Q1, μT	n, ϕ	Rct, Ω	W, kσ	C1, nF	χ^2
0 min blanks	138.70 ± 4.72	105.38 ± 9.55	481.20 ± 86.02	0.65 ± 0.03	4191.67 ± 273.63	2.89 ± 0.16	213933.33 ± 11579.42	6.50E-05
0 min	150.40 ± 3.54	410.53 ± 14.77	168.73 ± 8.03	0.93 ± 0.01	7495.67 ± 913.58	3.64 ± 0.07	204500.00 ± 9292.41	2.00E-04
10 min blanks	146.80 ± 8.33	118.63 ± 11.06	430.17 ± 96.46	0.71 ± 0.06	3859.67 ± 148.37	2.85 ± 0.17	226100.00 ± 12823.50	8.01E-05
10 min	172.27 ± 10.50	436.57 ± 31.48	169.03 ± 11.13	0.96 ± 0.02	7104.67 ± 36.40	3.58 ± 0.04	212066.67 ± 13461.16	8.27E-05
15 min blanks	135.67 ± 5.36	114.50 ± 4.30	477.33 ± 73.81	0.70 ± 0.02	4308.00 ± 223.02	3.14 ± 0.19	211766.67 ± 13380.44	9.56E-05
15 min	148.87 ± 5.96	402.23 ± 7.58	177.53 ± 5.60	0.93 ± 0.01	7022.67 ± 324.57	3.51 ± 0.17	212100.00 ± 11081.82	1.19E-04
30 min blanks	140.37 ± 8.45	109.30 ± 3.72	520.30 ± 32.04	0.65 ± 0.00	4244.00 ± 319.74	2.93 ± 0.25	213500.00 ± 8815.64	6.71E-05
30 min	137.13 ± 2.42	121.10 ± 9.91	530.17 ± 58.08	0.67 ± 0.04	4142.33 ± 30.91	3.25 ± 0.16	199833.33 ± 2424.11	1.33E-04
45 min blanks	142.07 ± 1.49	105.74 ± 3.47	505.30 ± 14.62	0.67 ± 0.01	4318.33 ± 66.93	2.86 ± 0.29	202533.33 ± 6805.61	6.11E-05
45 min	147.63 ± 8.15	368.13 ± 24.50	171.10 ± 9.99	0.94 ± 0.01	6932.67 ± 44.91	3.72 ± 0.27	207833.33 ± 6750.36	1.89E-04

Table S4. Fitting parameters obtained for the anti-SARS-CoV-2 spike glycoprotein S1 antibodies concentration study. Raw impedance data were fitted using the equivalent circuit: R_s-(R_{gel}||Q_1)-(($R_{ct}$$W$)||$C_1$).

Ab, μg/mL	Rs, Ω	Rgel, Ω	Q1, μT	n, ϕ	Rct, Ω	W, kσ	C1, nF	χ^2
5 blanks	120.13 ± 2.30	98.42 ± 5.22	660.83 ± 12.58	0.58 ± 0.01	4438.00 ± 8.38	3.12 ± 0.08	209333.33 ± 3810.32	5.67E-05
5	143.53 ± 6.75	289.90 ± 9.09	209.77 ± 29.10	0.92 ± 0.03	6733.33 ± 286.43	3.29 ± 0.09	213233.33 ± 1771.59	1.58E-04
10 blanks	143.73 ± 2.00	109.45 ± 8.62	517.90 ± 69.16	0.69 ± 0.05	4216.00 ± 244.90	2.92 ± 0.25	205233.33 ± 10102.73	6.50E-05
10	159.57 ± 4.98	373.90 ± 12.12	153.67 ± 3.59	0.99 ± 0.01	6596.00 ± 393.57	3.55 ± 0.15	199300.00 ± 6332.11	1.16E-04
25 blanks	156.3 ± 3.77	106.0633 ± 3.21	496.6 ± 56.62	0.681333 ± 0.03	3806.333 ± 160.18	2.685 ± 0.04	205166.6667 ± 6143.17	1.04E-04
25	173.23 ± 1.81	342.17 ± 53.36	170.97 ± 8.33	0.94 ± 0.01	6486.33 ± 424.51	3.50 ± 0.27	189066.67 ± 4894.52	1.24-e4
50 blanks	154.87 ± 7.90	110.13 ± 5.16	530.07 ± 125.23	0.65 ± 0.07	3743.67 ± 112.45	2.50 ± 0.09	210033.33 ± 5236.06	6.72E-05
50	157.37 ± 12.05	326.33 ± 4.99	165.60 ± 7.71	0.93 ± 0.01	5797.00 ± 183.63	3.56 ± 0.09	199866.67 ± 5612.95	4.20E-05

Table S5. Fitting parameters obtained for the Protein A concentration study. Raw impedance data were fitted using the equivalent circuit: R_s-(R_{gel}||Q_1)-((R_{ct}-W)||C_1).

Protein A, µg/mL	Rs, Ω	Rgel, Ω	Q1, µT	n, ϕ	Rct, Ω	W, kσ	C1, nF	χ^2
20 blanks	124.00 ± 4.77	101.26 ± 4.15	637.23 ± 30.67	0.59 ± 0.01	4332.67 ± 90.68	3.13 ± 0.08	208266.67 ± 3491.68	6.21E-05
20	143.53 ± 6.75	289.90 ± 9.09	209.77 ± 29.10	0.92 ± 0.03	6733.33 ± 286.43	3.29 ± 0.09	213233.33 ± 1771.59	1.60E-04
50 blanks	132.07 ± 5.56	108.40 ± 7.28	477.10 ± 6.98	0.68 ± 0.03	3962.33 ± 428.05	2.67 ± 0.20	212733.33 ± 3663.74	8.38E-05
50	146.97 ± 6.28	312.20 ± 31.77	185.33 ± 16.01	0.94 ± 0.01	6812.00 ± 690.21	3.50 ± 0.40	193066.67 ± 5034.62	1.60E-04
100 blanks	148.33 ± 3.79	103.57 ± 0.50	493.53 ± 28.98	0.69 ± 0.02	3697.67 ± 77.33	2.59 ± 0.19	212066.67 ± 2396.91	6.23E-05
100	158.13 ± 4.81	345.47 ± 28.37	159.33 ± 5.92	0.96 ± 0.02	6121.33 ± 77.50	3.18 ± 0.16	198766.67 ± 3389.64	9.20E-05

Table S6. Calibration curve parameters for the spiked ANF samples.

S1, µg/mL	Rs, Ω	Rgel, Ω	Q1, µT	n, ϕ	Rct, Ω	W, kσ	C1, nF	χ^2
0.001	150.83 ± 6.12	40.40 ± 5.03	632.67 ± 129.57	0.69 ± 0.02	2184.67 ± 65.41	2.82 ± 0.18	207033.33 ± 11418.93	1.21E-04
0.01	142.97 ± 2.13	46.31 ± 4.11	618.17 ± 156.43	0.66 ± 0.03	2552.00 ± 110.53	2.83 ± 0.02	194766.67 ± 3241.86	3.19E-04
0.1	155.17 ± 3.58	60.45 ± 3.75	581.17 ± 142.98	0.63 ± 0.02	2942.33 ± 85.87	2.44 ± 0.18	184566.67 ± 9946.78	5.40E-05
1	155.77 ± 4.43	52.59 ± 4.27	523.87 ± 164.24	0.61 ± 0.01	3369.00 ± 101.27	3.48 ± 0.29	156700.00 ± 5603.17	5.74E-05
10	160.97 ± 5.99	84.76 ± 3.98	381.83 ± 27.46	0.75 ± 0.01	4073.00 ± 254.34	2.88 ± 0.14	175100.00 ± 5619.21	6.45E-05
blanks	143.53 ± 5.06	40.83 ± 2.87	473.67 ± 80.53	0.67 ± 0.04	2138.00 ± 72.17	2.66 ± 0.07	179100.00 ± 4741.54	1.13E-04

Table S7. Calibration curve parameters for the spiked PBS samples.

S1, µg/mL	Rs, Ω	Rgel, Ω	Q1, µT	n, ϕ	Rct, Ω	W, kσ	C1, nF	χ^2
0.001	142.97 ± 10.37	81.21 ± 3.60	422.87 ± 88.15	0.74 ± 0.05	4230.33 ± 136.81	2.32 ± 0.19	195266.67 ± 11406.17	6.73E-05
0.01	126.13 ± 1.70	79.95 ± 2.85	443.87 ± 63.48	0.70 ± 0.03	4766.00 ± 95.26	2.43 ± 0.12	213933.33 ± 1753.94	6.87E-05
0.1	140.80 ± 4.90	92.50 ± 3.51	485.33 ± 9.78	0.66 ± 0.01	5177.00 ± 116.42	2.27 ± 0.03	198600.00 ± 4873.28	3.62E-05
1	144.43 ± 5.92	115.97 ± 5.52	271.00 ± 24.16	0.80 ± 0.01	5740.00 ± 122.61	2.60 ± 0.13	188733.33 ± 966.48	4.73E-05
10	157.93 ± 4.79	346.63 ± 27.36	160.10 ± 5.94	0.96 ± 0.01	6153.33 ± 91.67	3.17 ± 0.13	198966.67 ± 3458.43	8.64E-05
blanks	127.97 ± 0.59	77.47 ± 5.23	536.40 ± 71.39	0.65 ± 0.04	4099.00 ± 13.10	2.28 ± 0.07	207366.67 ± 3184.80	4.53E-05

A.2 Supporting Information for Manuscript 2

Supporting Information

Study of V_2CT_X-MXene Based Immunosensor for Sensitive Label-Free Impedimetric Detection of SARS-CoV-2 Spike Protein

Nikola Tasić,[1] Ivan Konjević,[1,2] Alnilan Lobato,[1,3] Dino Metarapi,[1] Matjaž Finšgar,[4] Filipa M. Oliveira,[5] Zděnek Sofer,[5] Rui Gusmão,[5,*] Xueji Zhang,[6] Samo B. Hočevar[1,*]

[1]*Department of Analytical Chemistry, National Institute of Chemistry, Hajdrihova ulica 19, 1000 Ljubljana, Slovenia*

[2]*Faculty of Chemistry and Chemical Technology, University of Ljubljana, Večna pot 113, 1000 Ljubljana, Slovenia*

[3]*International Postgraduate School Jožef Štefan, Jamova 39, 1000 Ljubljana, Slovenia*

[4]*Faculty of Chemistry and Chemical Engineering, University of Maribor, Smetanova ulica 17, 2000 Maribor, Slovenia*

[5]*Department of Inorganic Chemistry, University of Chemistry and Technology Prague, Technická 5, 166 28 Praha 6-Dejvice, Czech Republic*

[6]*School of Biomedical Engineering, Shenzhen University Health Science Center, 3688 Nanhai Road, Nanshan District, Shenzhen 518054, Guangdong, P.R. China*

Corresponding Authors:

[*]Samo B. Hočevar (samo.hocevar@ki.si)

[*]Rui Gusmão (rui.gusmao@vscht.cz)

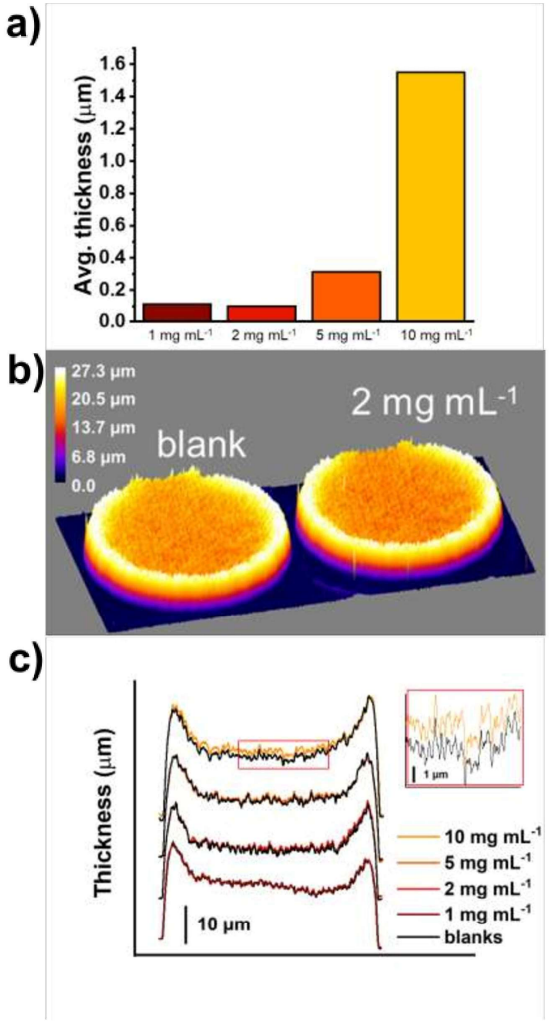


Figure S1. (a) Average thickness of the coatings using different concentrations of V_2CT_x MXene for SPCE modification, (b) 3D profiles of bare SPCE and SPCE modified with 2 mg mL^{-1} V_2CT_x MXene + 0.0025% Nafion, and (c) line sections of bare SPCE and SPCEs modified with different concentrations of V_2CT_x MXene.

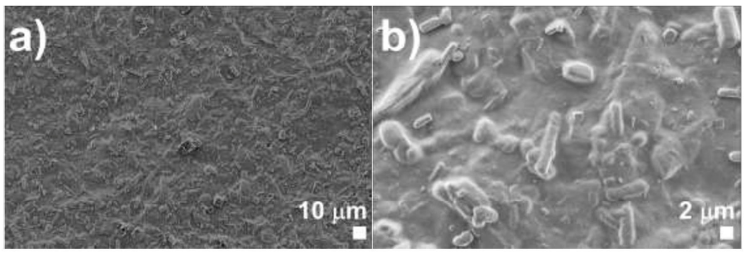


Figure S2. (a), (b) FE-SEM images of V_2CT_x MXene on SPCE after sonication of the drop-casting solution for 15 minutes at 22-30 °C. Both images correspond to the same sample recorded using different magnifications.

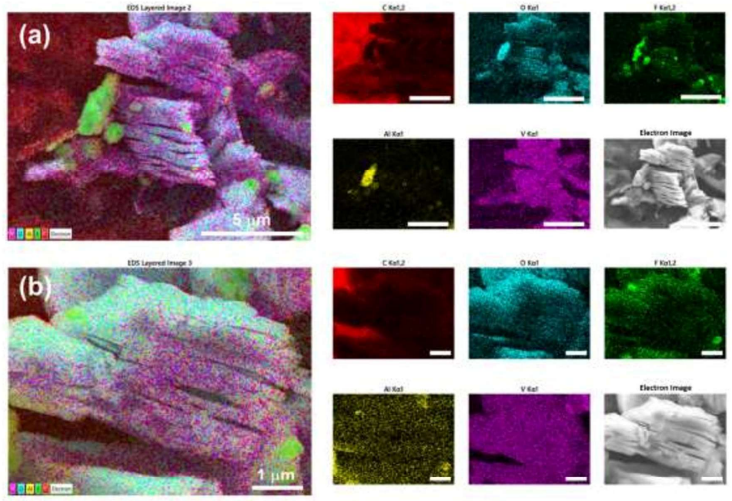


Figure S3. FE-SEM/EDX analysis of the as-synthesized V_2CT_x MXene drop-casted on SPCE (a, b). Scale bars in the images on the right are identical to those on the left.

Table S1. The elemental composition (wt.%) of samples presented in **Figure S3**.

Element	C	V	O	F	Al	Cl	S
Upper site on SPCE (a)	52.2	31.8	8.3	5.6	1.4	0.6	0.2
Magnified site on SPCE (b)	56.7	24.6	10.8	6.6	0.7	0.5	/

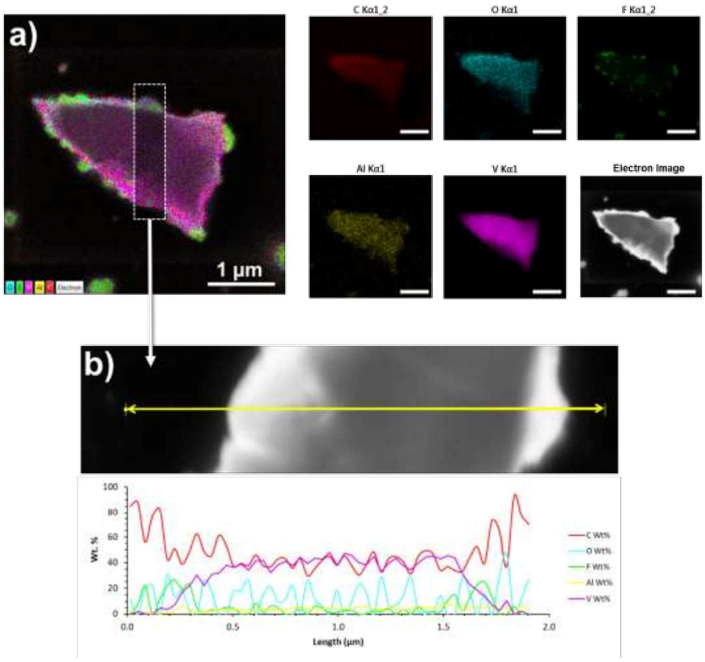


Figure S4. (a) Bright-field mode STEM/EDX analysis of the V_2CT_x MXene flake with EDX layered image, respective map of elements and electron micrograph, (b) detail of the area used for EDX 1D line scan analysis of the V_2CT_x MXene flake and respective profile of detected elements (wt. %). The scale bar represents 1 µm, and the length of the line scan is ca. 1.9 µm.

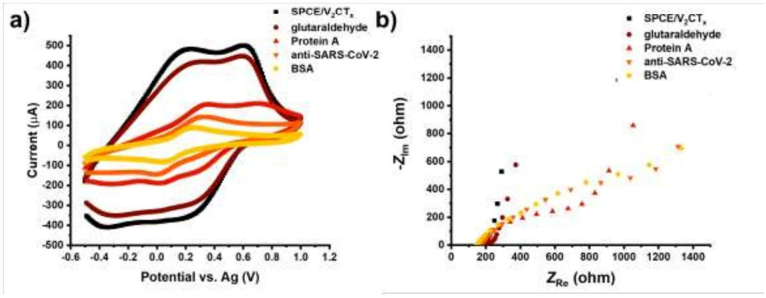


Figure S5. Step-by-step fabrication of the immunosensor followed by (a) cyclic voltammetry and (b) EIS (Nyquist spectra) in the presence of 1.0 mmol L^{-1} $[Fe(CN)_6]^{3-/4-}$ in 0.1 mol L^{-1} KCl.

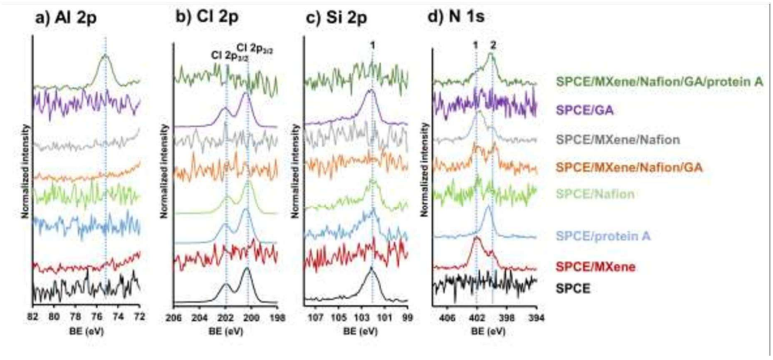


Figure S6. High-resolution XPS spectra of (a) Al 2p, (b) Cl 2p, (c) Si 2p, and (d) N 1s for different samples.

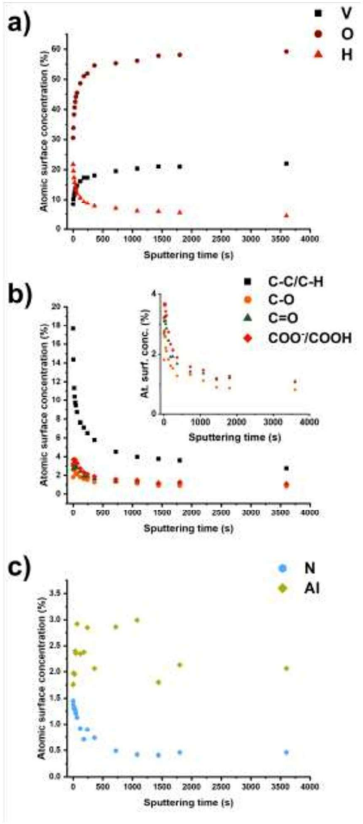


Figure S7. XPS depth profiles showing (a) V, O, F, (b) C-based compounds, and (c) N and Al.

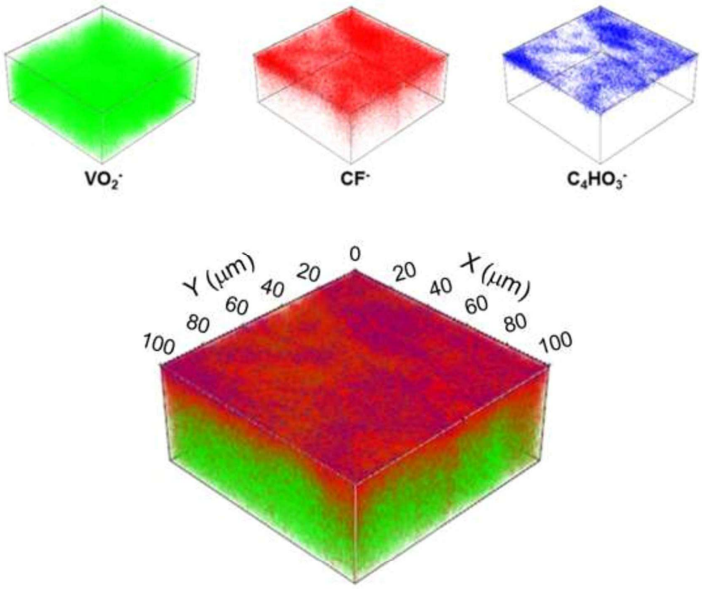


Figure S8. 3D negative ion ToF-SIMS images depicting the distribution of main constituents of our sensing architecture.

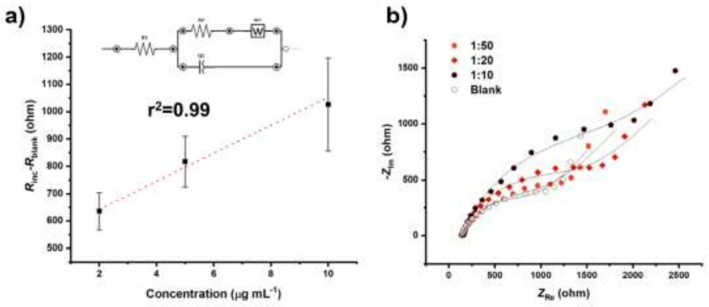


Figure S9. (a) Calibration curve of the fully optimized sensor, obtained in the diluted SARS-CoV-2 Spike protein sample in artificial nasopharyngeal fluid. The concentration of the sample was 100 μg mL^{-1}, and the tested dilutions of 1:10, 1:20, and 1:50 correspond to concentrations of 10, 5, and 2 μg mL^{-1}, respectively. The obtained spectra were fitted using the equivalent circuit shown in the inset of **Figure S9a,** (b) Corresponding Nyquist spectra for different sample dilutions.

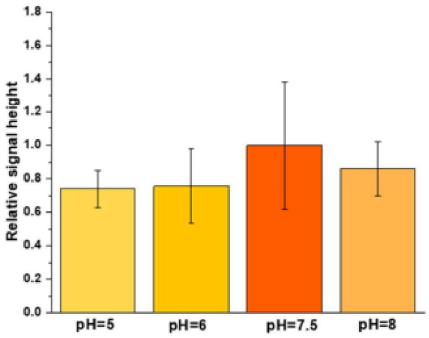


Figure S10. The effect of pH of the ANF on the signal of immunosensor.

Table S2. Comparison of the existing impedimetric immunosensors for the detection of SARS-CoV-2 Spike protein.

Sensing base	Range	LOD	Ref.
SPCE/ SiO_2 UiO-66 (MOF)	100 fg mL^{-1} to 10 ng mL^{-1}	100 fg mL^{-1} (1.27 fM)*	53
Au electrode	0.05 to 10 µg mL^{-1}	as low as 0.1 µg mL^{-1} (1.28 nM)*	54
SPE/MWCNT	0.05 to 1 µg mL^{-1}	20±1.8 ng mL^{-1} (0.255 nM)*	55
SPCE/gelatin	0.001 to 10 µg mL^{-1}	90 pg mL^{-1} (1.15 pM)*	56
AuSPE	700 ng mL^{-1} to 7 µg mL^{-1}	as low as 38.99 ng mL^{-1} (0.498 nM)*	57
SPCE/Cu_2O nanocubes	0.25 fg mL^{-1} to 1 µg mL^{-1}	0.04 fg mL^{-1} (0.51 zM)*	58
SPCE/electrodeposited Au NPs	10^{-7} to 10^{-11} mol L^{-1}	3.16 pM	59
AuSPE	11.56 to 740 ng mL^{-1}	5.65 pg mL^{-1} (72.2 fM)*	60
AuIDE	250 to 8000 fM	189 fM	61
SPCE/ V_2CT_x	10^{-5} to 10^{-1} µg mL^{-1}	45 fM	this study

SPCE – screen printed carbon electrode, MOF – metal organic framework, SPE – screen printed electrode, AuIDE – gold interdigitated electrode. *Molar concentrations were calculated from the reported mass concentrations, by using the molecular weight for Spike S1 protein of 78.3 kDa.

A.3 Supporting Information for Manuscript 3

Supporting Information

Label-free and Sensitive Detection of *Citrus Bark Cracking Viroid* in Hop Using $Ti_3C_2T_x$ MXene-modified Genosensor

Alnilan Lobato[1,2], Ivan Konjević[1,3], Sebastjan Radišek[4], Jernej Jakše[5], Helena Volk[5], Monika Hermanová[6], Miroslav Fojta[6], Jan Paštika[7], Zdeněk Sofer[7], Rui Gusmão[7,b], Samo B. Hočevar[1], and Nikola Tasić[1,a]

[1]*Department of Analytical Chemistry, National Institute of Chemistry, Ljubljana, Slovenia*
[2]*International Postgraduate School Jožef Stefan, Ljubljana, Slovenia*
[3]*Faculty of Chemistry and Chemical Technology, University of Ljubljana, Ljubljana, Slovenia*
[4]*Slovenian Institute of Hop Research and Brewing, Žalec, Slovenia*
[5]*Biotechnical Faculty, University of Ljubljana, Ljubljana, Slovenia*
[6]*Institute of Biophysics, Academy of Science of the Czech Republic, Brno, Czech Republic*
[7]*Department of Inorganic Chemistry, University of Chemistry and Technology Prague, Czech Republic*

[a]nikola.tasic@ki.si
[b]rui.gusmao@vscht.cz

Table S1. Samples from viroid-infected plants

Sample no.	Total RNA concentration (ng μL^{-1})	CBCVd concentration (pg μL^{-1})	Sample origin
CBCVd_1	595.9	1.35	Hop plant infected with CBCVd
CBCVd_2	275.5	0.81	Hop plant infected with CBCVd
CBCVd_3	112.5	0.52	Hop plant infected with CBCVd
CBCVd_4	398.0	0.50	Hop plant infected with CBCVd
CBCVd_5	326.0	0.54	Hop plant infected with CBCVd
CBCVd_6	215.5	0.18	Hop plant infected with CBCVd
HLVd_1	267.5	-	Hop plant infected with HLVd*
VF_1	530.0	-	Viroid-free hop Plant
VF_2	252.0	-	Viroid-free hop plant
VF_3	304.0	-	Viroid-free hop plant
TOM_1	480.5	-	Viroid-free tomato
TOM_2	425.0	-	Viroid-free tomato

*HLVd content was not quantified

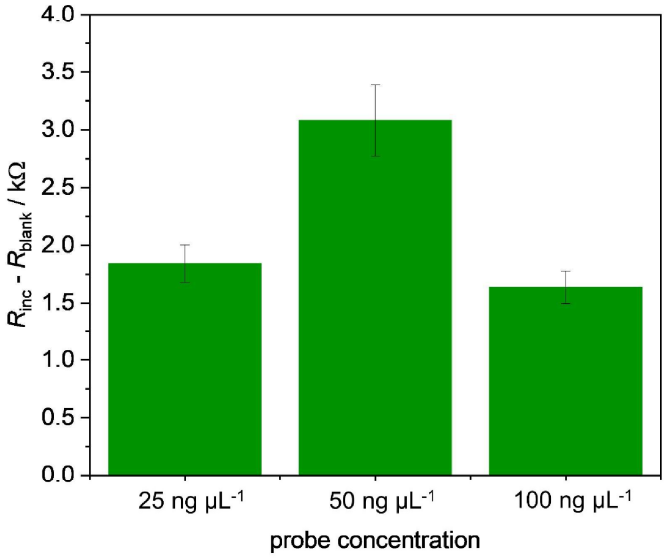


Figure S1. The effect of the capture probe concentration upon the genosensor's response (capture probe incubation time: 2h, sample incubation time: 60 min, CBCVd concentration: 250 fg μL^{-1}).

Table S2. Fitting parameters obtained by EIS measurements in 5.0 mM $[Fe(CN)_6]^{3-/4-}$ + 0.1 M KCl for the optimization steps of the genosensor build-up. CBCVd_1 sample was diluted to a concentration of 250 fg μL^{-1}.

STR-AGAR deposition time	Analytical signal ($R_{inc} - R_{blank}$)
1 h	2780.7 ± 328.0
2 h	3279.3 ± 169.9
4 h	3153.0 ± 128.8

Capture probe incubation time	Analytical signal ($R_{inc} - R_{blank}$)
1 h	3100.7 ± 243.8
2 h	3279.3 ± 115.3
4 h	2305.0 ± 115.3

Sample incubation time	Analytical signal ($R_{inc} - R_{blank}$)
15 min	2409.3 ± 212.3
30 min	2322.5 ± 909.3
60 min	3279.3 ± 169.9
90 min	3271 ± 261.5

Capture probe concentration	Analytical signal ($R_{inc} - R_{blank}$)
25 ng μL^{-1}	1840.3 ± 162.9
50 ng μL^{-1}	3079.7 ± 307.8
100 ng μL^{-1}	1635.7 ± 141.4

Table S3. Fitting parameters obtained by EIS measurements in 5.0 mM $[Fe(CN)_6]^{3-/4-}$+ 0.1 M KCl for fabrication steps of the genosensor build-up. CBCVd_1 sample was diluted to a concentration of 250 fg μL^{-1}.

Step	R_s, Ω	R_{ct}, Ω	Q_1, μT	n, ϕ	W_1, kσ
Bare GCE	111.3	14.62	0.75	1.00	2.39
STR-AGAR beads	221.3	319.30	9.15	0.79	2.67
Capture probe	169.9	1597.00	2.49	0.90	2.39
Glycine	171.6	2816.00	2.36	0.90	2.40
Sample (CBCVd_1)	167.1	4323.00	2.25	0.90	2.20

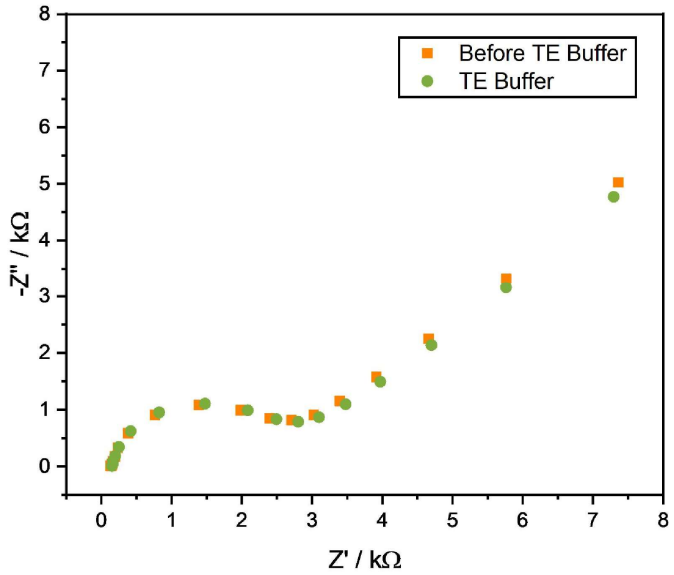


Figure S2. EIS spectra of the fully fabricated genosensor and after its incubation in TE buffer (pH 8.0). The corresponding fitting parameters are listed in **Table S4**.

Table S4. Fitting parameters obtained by EIS measurements in 5.0 mM $[Fe(CN)_6]^{3-/4-}$+ 0.1 M KCl using the fully fabricated genosensor and after its incubation in TE buffer (pH 8.0).

Step	R_s, Ω	R_{ct}, Ω	Q_1, μT	n, ϕ	W_1, kσ
Before TE buffer	142.9	2279	1.49	0.91	3.78
TE Buffer	149.8	2362	1.37	0.91	3.62

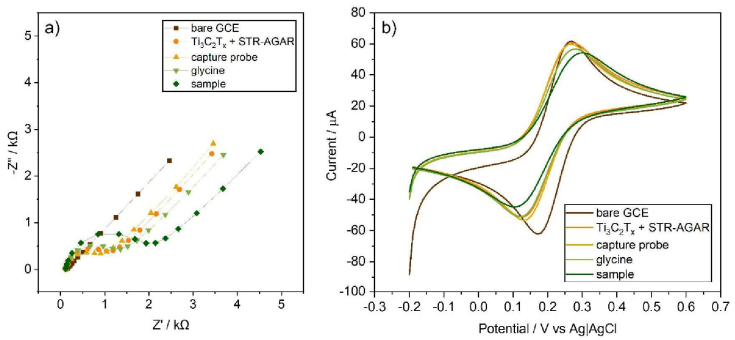


Figure S3. Characterization of the step-by-step fabrication of the $Ti_3C_2T_x$ MXene-based genosensor using (a) EIS and (b) CV measurements in 5 mM $[Fe(CN)_6)]^{3-/4-}$ + 0.1 M KCl. The corresponding fitting parameters are listed in **Table S3**.

Table S5. Fitting parameters obtained by EIS measurements in 5.0 mM $[Fe(CN)_6]^{3-/4-}$+ 0.1 M KCl for all steps of the $Ti_3C_2T_x$ MXene-based genosensor build-up. CBCVd_2 sample was diluted to a concentration of 25 fg μL^{-1}.

Step	R_s, Ω	R_{ct}, Ω	Q_1, μT	n, ϕ	W_1, kσ
Bare GCE	132.1	17.6	0.88	1.00	2.30
STR-AGAR beads	122.2	921.1	4.10	0.89	1.93
Capture probe	120.2	742.7	4.26	0.89	2.02
Glycine	117.1	1124.0	3.97	0.89	1.91
Sample (CBCVd_2)	116.1	1782.0	3.22	0.88	1.99

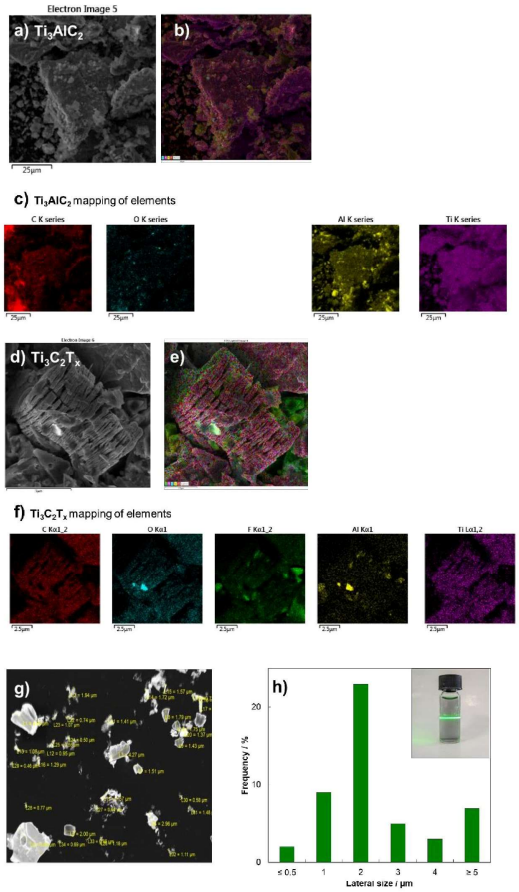


Figure S4. SEM micrograph of a (a) Ti_3AlC_2 multilayer flake and (b) respective EDX mapping of detected elements, (c) individual EDX map of each element. SEM micrograph of a (d) $Ti_3C_2T_x$ multilayer flake and (e) respective EDX mapping of detected elements, (f) individual EDX map of each element. (g) Dark mode STEM micrograph with selection of flakes used in the lateral size distribution of Ti_3AlC_2 and (h) size distribution of $Ti_3C_2T_x$ flakes. Inset: Tyndall scattering effect of the diluted colloidal solution.

Table S6. Quantification of elements detected from EDX acquisition at 20 kV acceleration voltage for Ti_3AlC_2 and $Ti_3C_2T_x$.

	Ti_3AlC_2		$Ti_3C_2T_x$	
Element	**at%**	**σ**	**at%**	**σ**
C	29.9	7.93	24.8	5.8
O	12.4	3.39	15.1	2.0
F	0	0	26.8	6.2
Al	17.3	4.19	1.7	0.7
Ti	40.3	8.75	31.6	6.9

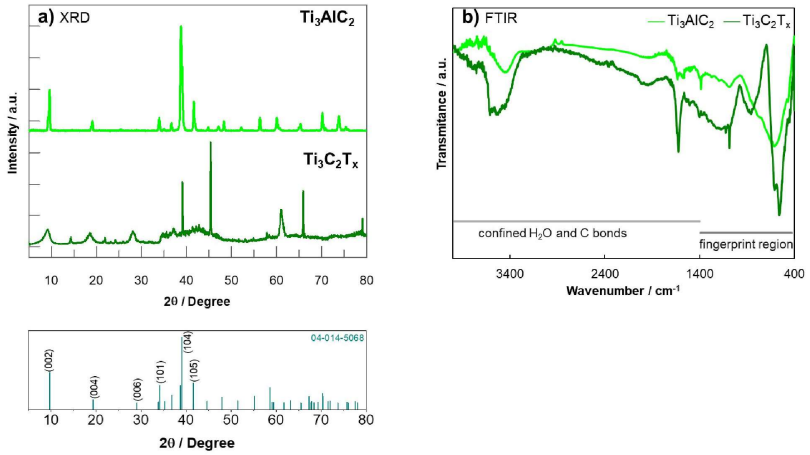


Figure S5. (a) Wide spectra XRD patterns of Ti_3AlC_2 and $Ti_3C_2T_x$, and comparison with ICDD 04-14-5068 spectra lines, and (b) FTIR spectrum in the 4000-400 cm^{-1} of Ti_3AlC_2 and $Ti_3C_2T_x$ with assigned region of bond vibrations.

References

[1] B. S. Guttman, "Virus," in *Encyclopedia of Genetics*, Elsevier, 2001, pp. 2108–2114. doi: 10.1006/rwgn.2001.1371.

[2] A. E. Gorbalenya, C. Lauber, and S. Siddell, "Taxonomy of Viruses," in *Reference Module in Biomedical Sciences*, Elsevier, 2019. doi: 10.1016/b978-0-12-801238-3.99237-7.

[3] P. Mehta, D. F. McAuley, M. Brown, E. Sanchez, R. S. Tattersall, and J. J. Manson, "COVID-19: consider cytokine storm syndromes and immunosuppression," *The Lancet*, vol. 395, no. 10229, pp. 1033–1034, Mar. 2020, doi: 10.1016/S0140-6736(20)30628-0.

[4] T. Yamamoto, M. Ozaki, D. Kasugai, and G. Burnham, "Insufficient Critical Care Preparedness for the COVID-19 Pandemic in Japan: Estimates Based on Demographic Data," *SSRN Electronic Journal*, 2020, doi: 10.2139/ssrn.3594653.

[5] E. M. Tsagris, Á. E. M. de Alba, M. Gozmanova, and K. Kalantidis, "Viroids," *Cell Microbiol*, vol. 10, no. 11, pp. 2168–2179, Nov. 2008, doi: 10.1111/J.1462-5822.2008.01231.X.

[6] R. Flores, C. Hernández, A. E. Martínez De Alba, J. A. Daròs, and F. Di Serio, "Viroids and viroid-host interactions," 2005. doi: 10.1146/annurev.phyto.43.040204.140243.

[7] R. Flores *et al.*, "Viroids, the simplest RNA replicons: How they manipulate their hosts for being propagated and how their hosts react for containing the infection," *Virus Res*, vol. 209, pp. 136–145, Nov. 2015, doi: 10.1016/J.VIRUSRES.2015.02.027.

[8] N. Duran-Vila, C. N. Roistacher, R. Rivera-Bustamante, and J. S. Semancik, "A Definition of Citrus Viroid Groups and Their Relationship to the Exocortis Disease," *Journal of General Virology*, vol. 69, no. 12, pp. 3069–3080, Dec. 1988, doi: 10.1099/0022-1317-69-12-3069.

[9] J. Jakse, S. Radisek, T. Pokorn, J. Matousek, and B. Javornik, "Deep-sequencing revealed Citrus bark cracking viroid (CBCVd) as a highly aggressive pathogen on hop," *Plant Pathol*, vol. 64, no. 4, pp. 831–842, Aug. 2015, doi: 10.1111/PPA.12325.

[10] EPPO, "*Citrus bark cracking viroid.* EPPO datasheets on pests recommended for regulation," https://gd.eppo.int/taxon/CBCVD0/datasheet.

[11] G. Park *et al.*, "Recent Developments in DNA-Nanotechnology-Powered Biosensors for Zika/Dengue Virus Molecular Diagnostics," *Nanomaterials*, vol. 13, no. 2, p. 361, Jan. 2023, doi: 10.3390/nano13020361.

[12] L. C. Brazaca *et al.*, "Biosensing strategies for the electrochemical detection of viruses and viral diseases – A review," *Anal Chim Acta*, vol. 1159, May 2021, doi: 10.1016/J.ACA.2021.338384.

[13] F. S. Felix and L. Angnes, "Electrochemical immunosensors – A powerful tool for analytical applications," *Biosens Bioelectron*, vol. 102, no. August 2017, pp. 470–478, Apr. 2018, doi: 10.1016/j.bios.2017.11.029.

[14] A. J. Bard, L. R. Faulkner, and H. S. White, *Electrochemical Methods*, Second edition. Wiley, 2002.

[15] E. Cesewski and B. N. Johnson, "Electrochemical biosensors for pathogen detection," *Biosens Bioelectron*, vol. 159, p. 112214, Jul. 2020, doi: 10.1016/J.BIOS.2020.112214.

[16] J. Wang, *Analytical Electrochemistry*, Second edition. Weinheim: Wiley, 2000.

[17] A. Ch. Lazanas and M. I. Prodromidis, "Electrochemical Impedance Spectroscopy—A Tutorial," *ACS Measurement Science Au*, vol. 3, no. 3, pp. 162–193, Jun. 2023, doi: 10.1021/acsmeasuresciau.2c00070.

[18] W.-W. Zhao, J.-J. Xu, and H.-Y. Chen, "Photoelectrochemical DNA Biosensors," *Chem Rev*, vol. 114, no. 15, pp. 7421–7441, Aug. 2014, doi: 10.1021/cr500100j.

[19] M. M. Shanbhag, G. Manasa, R. J. Mascarenhas, K. Mondal, and N. P. Shetti, "Fundamentals of bio-electrochemical sensing," *Chemical Engineering Journal Advances*, vol. 16, Nov. 2023, doi: 10.1016/j.ceja.2023.100516.

[20] R. Patel *et al.*, "Part I: Non-faradaic electrochemical impedance-based DNA biosensor for detecting phytopathogen – Ralstonia solanacearum," *Bioelectrochemistry*, vol. 150, Apr. 2023, doi: 10.1016/j.bioelechem.2023.108370.

[21] E. P. Randviir and C. E. Banks, "A review of electrochemical impedance spectroscopy for bioanalytical sensors," *Analytical Methods*, vol. 14, no. 45, pp. 4602–4624, 2022, doi: 10.1039/D2AY00970F.

[22] H. S. Magar, R. Y. A. Hassan, and A. Mulchandani, "Electrochemical Impedance Spectroscopy (EIS): Principles, Construction, and Biosensing Applications," *Sensors 2021, Vol. 21, Page 6578*, vol. 21, no. 19, p. 6578, Oct. 2021, doi: 10.3390/S21196578.

[23] "PSTrace 5.9 (PalmSens B.V., Netherlands)."

[24] F. Scholz, *Electroanalytical Methods*. Berlin, Heidelberg: Springer Berlin Heidelberg, 2010. doi: 10.1007/978-3-642-02915-8.

[25] D. Grieshaber, R. MacKenzie, J. Vörös, and E. Reimhult, "Electrochemical Biosensors - Sensor Principles and Architectures," *Sensors*, vol. 8, no. 3, pp. 1400–1458, Mar. 2008, doi: 10.3390/s80314000.

[26] N. Jaffrezic-Renault and S. V Dzyadevych, "Conductometric Microbiosensors for Environmental Monitoring," *Sensors*, vol. 8, pp. 2569–2588, 2008, [Online]. Available: www.mdpi.org/sensors

[27] S. Menon, M. R. Mathew, S. Sam, K. Keerthi, and K. G. Kumar, "Recent advances and challenges in electrochemical biosensors for emerging and re-emerging infectious diseases," *Journal of Electroanalytical Chemistry*, vol. 878, p. 114596, Dec. 2020, doi: 10.1016/J.JELECHEM.2020.114596.

[28] N. Elgrishi, K. J. Rountree, B. D. McCarthy, E. S. Rountree, T. T. Eisenhart, and J. L. Dempsey, "A Practical Beginner's Guide to Cyclic Voltammetry," *J Chem Educ*, vol. 95, no. 2, pp. 197–206, Feb. 2018, doi: 10.1021/acs.jchemed.7b00361.

[29] K. Kerman, Y. Morita, Y. Takamura, and E. Tamiya, "Label-free electrochemical detection of DNA hybridization on gold electrode," *Electrochem commun*, vol. 5, no. 10, pp. 887–891, Oct. 2003, doi: 10.1016/J.ELECOM.2003.08.013.

[30] M. Frasconi, F. Mazzei, and T. Ferri, "Protein immobilization at gold–thiol surfaces and potential for biosensing," *Anal Bioanal Chem*, vol. 398, no. 4, pp. 1545–1564, Oct. 2010, doi: 10.1007/s00216-010-3708-6.

[31] W. E. Van der Linden and J. W. Dieker, "Glassy carbon as electrode material in electro- analytical chemistry," *Anal Chim Acta*, vol. 119, no. 1, pp. 1–24, Sep. 1980, doi: 10.1016/S0003-2670(00)00025-8.

[32] I. Švancara, K. Vytřas, J. Barek, and J. Zima, "Carbon Paste Electrodes in Modern Electroanalysis," *Crit Rev Anal Chem*, vol. 31, no. 4, pp. 311–345, Oct. 2001, doi: 10.1080/20014091076785.

[33] C. Q. Zhao, J. Zhou, K. W. Wu, S. N. Ding, J. J. Xu, and H. Y. Chen, "Plasmonic Enhanced Gold Nanoclusters-Based Photoelectrochemical Biosensor for Sensitive Alkaline Phosphatase Activity Analysis," *Anal Chem*, vol. 92, no. 10, pp. 6886–6892, May 2020, doi: 10.1021/acs.analchem.9b05432.

[34] J. Kwon, Y. Lee, T. Lee, and J. H. Ahn, "Aptamer-Based Field-Effect Transistor for Detection of Avian Influenza Virus in Chicken Serum," *Anal Chem*, vol. 92, no. 7, pp. 5524–5531, Apr. 2020, doi: 10.1021/acs.analchem.0c00348.

[35] A. N. Kawde, N. Baig, and M. Sajid, "Graphite pencil electrodes as electrochemical sensors for environmental analysis: A review of features, developments, and applications," 2016, *Royal Society of Chemistry*. doi: 10.1039/c6ra17466c.

[36] V. N. Ataide *et al.*, "Paper-based electrochemical biosensors for the diagnosis of viral diseases," *Microchimica Acta*, vol. 190, no. 7, Jul. 2023, doi: 10.1007/s00604-023-05856-2.

[37] A. García-Miranda Ferrari, S. J. Rowley-Neale, and C. E. Banks, "Screen-printed electrodes: Transitioning the laboratory in-to-the field," Aug. 01, 2021, *Elsevier B.V.* doi: 10.1016/j.talo.2021.100032.

[38] E. Farjami, L. Clima, K. V. Gothelf, and E. E. Ferapontova, "DNA interactions with a Methylene Blue redox indicator depend on the DNA length and are sequence specific," *Analyst*, vol. 135, no. 6, pp. 1443–1448, 2010, doi: 10.1039/c0an00049c.

[39] K. Lacina, J. Věžník, J. Sopoušek, Z. Farka, V. Lacinová, and P. Skládal, "Concentration and diffusion of the redox probe as key parameters for label-free impedimetric immunosensing," *Bioelectrochemistry*, vol. 149, Feb. 2023, doi: 10.1016/j.bioelechem.2022.108308.

[40] J. D. Schrattenecker, R. Heer, E. Melnik, T. Maier, G. Fafilek, and R. Hainberger, "Hexaammineruthenium (II)/(III) as alternative redox-probe to Hexacyanoferrat (II)/(III) for stable impedimetric biosensing with gold electrodes," *Biosens Bioelectron*, vol. 127, pp. 25–30, Feb. 2019, doi: 10.1016/j.bios.2018.12.007.

[41] J. Isailović *et al.*, "Study of a Sensitive and Selective Electrochemical Biosensor for Glucose Based on Bi2Ru2O7 Pyrochlore Clusters Combined with MWCNTs," *Chemosensors*, vol. 13, no. 3, Mar. 2025, doi: 10.3390/chemosensors13030109.

[42] D. R. Thevenot, K. Tóth, R. A. Durst, and G. S. Wilson, "Electrochemical Biosensors: Recommended Definitions and Classification," *Pure and Applied Chemistry*, vol. 71, no. 12, pp. 2333–2348, Jan. 1999, doi: 10.1351/pac199971122333.

[43] N. J. Ronkainen, H. B. Halsall, and W. R. Heineman, "Electrochemical biosensors," *Chem Soc Rev*, vol. 39, no. 5, pp. 1747–1763, Apr. 2010, doi: 10.1039/B714449K.

[44] D. L. Nelson and M. M. Cox, *Lehninger: Principles of Biochemistry*. Berlin, Heidelberg: Springer Berlin Heidelberg, 2001. doi: 10.1007/978-3-662-08289-8.

[45] I. Sela-Culang, V. Kunik, and Y. Ofran, "The Structural Basis of Antibody-Antigen Recognition," *Front Immunol*, vol. 4, p. 302, 2013, doi: 10.3389/fimmu.2013.00302.

[46] A. V. Lakhin, V. Z. Tarantul, and L. V. Gening, "Aptamers: Problems, Solutions and Prospects," *Acta Naturae*, vol. 5, no. 4, p. 34, 2013, doi: 10.32607/20758251-2013-5-4-34-43.

[47] T. H. Ku *et al.*, "Nucleic Acid Aptamers: An Emerging Tool for Biotechnology and Biomedical Sensing," *Sensors (Basel)*, vol. 15, no. 7, p. 16281, Jul. 2015, doi: 10.3390/S150716281.

[48] P. B. Luppa, L. J. Sokoll, and D. W. Chan, "Immunosensors—principles and applications to clinical chemistry," *Clinica Chimica Acta*, vol. 314, no. 1–2, pp. 1–26, Dec. 2001, doi: 10.1016/S0009-8981(01)00629-5.

[49] Q. Palomar, X. Xu, C. Gondran, M. Holzinger, S. Cosnier, and Z. Zhang, "Voltammetric sensing of recombinant viral dengue virus 2 NS1 based on Au nanoparticle–decorated multiwalled carbon nanotube composites," *Microchimica Acta*, vol. 187, no. 6, p. 363, Jun. 2020, doi: 10.1007/s00604-020-04339-y.

[50] M. Awan *et al.*, "A sandwich electrochemical immunosensor based on antibody functionalized-silver nanoparticles (Ab-Ag NPs) for the detection of dengue biomarker protein NS1," *J Mol Liq*, vol. 317, p. 114014, Nov. 2020, doi: 10.1016/J.MOLLIQ.2020.114014.

[51] A. Kaushik *et al.*, "A sensitive electrochemical immunosensor for label-free detection of Zika-virus protein," *Scientific Reports 2018 8:1*, vol. 8, no. 1, pp. 1–5, Jun. 2018, doi: 10.1038/s41598-018-28035-3.

[52] A. M. Faria and T. Mazon, "Early diagnosis of Zika infection using a ZnO nanostructures-based rapid electrochemical biosensor," *Talanta*, vol. 203, pp. 153–160, Oct. 2019, doi: 10.1016/J.TALANTA.2019.04.080.

[53] E. K. G. Trindade and R. F. Dutra, "A label-free and reagentless immunoelectrode for antibodies against hepatitis B core antigen (anti-HBc) detection," *Colloids Surf B Biointerfaces*, vol. 172, pp. 272–279, Dec. 2018, doi: 10.1016/J.COLSURFB.2018.08.050.

[54] J. P. De Campos Da Costa, W. B. Bastos, P. I. Da Costa, M. A. Zaghete, E. Longo, and J. P. Carmo, "Portable Laboratory Platform with Electrochemical Biosensors for Immunodiagnostic of Hepatitis C Virus," *IEEE Sens J*, vol. 19, no. 22, pp. 10701–10709, Nov. 2019, doi: 10.1109/JSEN.2019.2930957.

[55] P. Ranjan *et al.*, "Rapid diagnosis of SARS-CoV-2 using potential point-of-care electrochemical immunosensor: Toward the future prospects," *Int Rev Immunol*, vol. 40, no. 1–2, pp. 126–142, Mar. 2021, doi: 10.1080/08830185.2021.1872566.

[56] L. Liv, "Electrochemical immunosensor platform based on gold-clusters, cysteamine and glutaraldehyde modified electrode for diagnosing COVID-19," *Microchemical Journal*, vol. 168, p. 106445, Sep. 2021, doi: 10.1016/J.MICROC.2021.106445.

[57] B. Liu, P.-J. J. Huang, E. Y. Kelly, and J. Liu, "Graphene oxide surface blocking agents can increase the DNA biosensor sensitivity," *Biotechnol J*, vol. 11, no. 6, pp. 780–787, Jun. 2016, doi: 10.1002/biot.201500540.

[58] M. I. Pividori, A. Merkoçi, and S. Alegret, "Electrochemical genosensor design: immobilisation of oligonucleotides onto transducer surfaces and detection methods," *Biosens Bioelectron*, vol. 15, no. 5–6, pp. 291–303, Aug. 2000, doi: 10.1016/S0956-5663(00)00071-3.

[59] S. Carinelli, M. Kühnemund, M. Nilsson, and M. I. Pividori, "Yoctomole electrochemical genosensing of Ebola virus cDNA by rolling circle and circle to circle amplification," *Biosens Bioelectron*, vol. 93, pp. 65–71, Jul. 2017, doi: 10.1016/J.BIOS.2016.09.099.

[60] H. Ilkhani and S. Farhad, "A novel electrochemical DNA biosensor for Ebola virus detection," *Anal Biochem*, vol. 557, pp. 151–155, Sep. 2018, doi: 10.1016/J.AB.2018.06.010.

[61] C. Singhal, C. S. Pundir, and J. Narang, "A genosensor for detection of consensus DNA sequence of Dengue virus using ZnO/Pt-Pd nanocomposites," *Biosens Bioelectron*, vol. 97, pp. 75–82, Nov. 2017, doi: 10.1016/J.BIOS.2017.05.047.

[62] R. da Fonseca Alves, D. L. Franco, M. T. Cordeiro, E. M. de Oliveira, R. A. Fireman Dutra, and M. del Pilar Taboada Sotomayor, "Novel electrochemical genosensor for Zika virus based on a poly-(3-amino-4-hydroxybenzoic acid)-modified pencil carbon graphite electrode," *Sens Actuators B Chem*, vol. 296, p. 126681, Oct. 2019, doi: 10.1016/j.snb.2019.126681.

[63] K. Malecka *et al.*, "Ultrasensitive electrochemical genosensor for direct detection of specific RNA sequences derived from avian influenza viruses present in biological samples," *Acta Biochim Pol*, vol. 66, no. 3, pp. 299–304, 2019, doi: 10.18388/abp.2019_2774.

[64] K. Malecka *et al.*, "Electrochemical genosensor based on disc and screen printed gold electrodes for detection of specific DNA and RNA sequences derived from Avian Influenza Virus H5N1," *Sens Actuators B Chem*, vol. 224, pp. 290–297, Mar. 2016, doi: 10.1016/J.SNB.2015.10.044.

[65] S. S. Low, H. S. Loh, J. S. Boey, P. S. Khiew, W. S. Chiu, and M. T. T. Tan, "Sensitivity enhancement of graphene/zinc oxide nanocomposite-based electrochemical impedance genosensor for single stranded RNA detection," *Biosens Bioelectron*, vol. 94, pp. 365–373, Aug. 2017, doi: 10.1016/J.BIOS.2017.02.038.

[66] K. Thapa, W. Liu, and R. Wang, "Nucleic acid-based electrochemical biosensor: Recent advances in probe immobilization and signal amplification strategies," *Wiley Interdiscip Rev Nanomed Nanobiotechnol*, vol. 14, no. 1, Jan. 2022, doi: 10.1002/WNAN.1765.

[67] M. Santhanam, I. Algov, and L. Alfonta, "DNA/RNA Electrochemical Biosensing Devices a Future Replacement of PCR Methods for a Fast Epidemic Containment," *Sensors*, vol. 20, no. 16, p. 4648, Aug. 2020, doi: 10.3390/s20164648.

[68] E. Paleček and M. Bartošík, "Electrochemistry of Nucleic Acids," *Chem Rev*, vol. 112, no. 6, pp. 3427–3481, Jun. 2012, doi: 10.1021/cr200303p.

[69] N. Paniel, J. Baudart, A. Hayat, and L. Barthelmebs, "Aptasensor and genosensor methods for detection of microbes in real world samples," *Methods*, vol. 64, no. 3, pp. 229–240, Dec. 2013, doi: 10.1016/J.YMETH.2013.07.001.

[70] K. Thapa, W. Liu, R. Wang, and C. Risheng Wang, "Nucleic acid-based electrochemical biosensor: Recent advances in probe immobilization and signal amplification strategies," *Wiley Interdiscip Rev Nanomed Nanobiotechnol*, p. e1765, Nov. 2021, doi: 10.1002/WNAN.1765.

[71] H.-P. Peng, K. H. Lee, J.-W. Jian, and A.-S. Yang, "Origins of specificity and affinity in antibody–protein interactions," *Proceedings of the National Academy of Sciences*, vol. 111, no. 26, Jul. 2014, doi: 10.1073/pnas.1401131111.

[72] M. J. McGrath and C. N. Scanaill, "Sensing and Sensor Fundamentals," in *Sensor Technologies*, Berkeley, CA: Apress, 2013, pp. 15–50. doi: 10.1007/978-1-4302-6014-1_2.

[73] V. C. Diculescu, A. M. Chiorcea-Paquim, and A. M. Oliveira-Brett, "Applications of a DNA-electrochemical biosensor," *TrAC Trends in Analytical Chemistry*, vol. 79, pp. 23–36, May 2016, doi: 10.1016/J.TRAC.2016.01.019.

[74] P. Dauphin-Ducharme and K. W. Plaxco, "Maximizing the Signal Gain of Electrochemical-DNA Sensors," *Anal Chem*, vol. 88, no. 23, pp. 11654–11662, Dec. 2016, doi: 10.1021/acs.analchem.6b03227.

[75] A. Kaliyaraj Selva Kumar, Y. Zhang, D. Li, and R. G. Compton, "A mini-review: How reliable is the drop casting technique?," *Electrochem commun*, vol. 121, p. 106867, Dec. 2020, doi: 10.1016/J.ELECOM.2020.106867.

[76] J. I. A. Rashid and N. A. Yusof, "The strategies of DNA immobilization and hybridization detection mechanism in the construction of electrochemical DNA sensor: A review," *Sens Biosensing Res*, vol. 16, pp. 19–31, Nov. 2017, doi: 10.1016/J.SBSR.2017.09.001.

[77] W. Zheng and Y. F. Zheng, "Gelatin-functionalized carbon nanotubes for the bioelectrochemistry of hemoglobin," *Electrochem commun*, vol. 9, no. 7, pp. 1619–1623, Jul. 2007, doi: 10.1016/J.ELECOM.2007.03.007.

[78] D. Bal Altuntaş and F. Kuralay, "MoS2/Chitosan/GOx-Gelatin modified graphite surface: Preparation, characterization and its use for glucose determination," *Materials Science and Engineering: B*, vol. 270, p. 115215, Aug. 2021, doi: 10.1016/J.MSEB.2021.115215.

[79] S. Cosnier, "Electropolymerization of amphiphilic monomers for designing amperometric biosensors," *Electroanalysis*, vol. 9, no. 12, pp. 894–902, Aug. 1997, doi: 10.1002/elan.1140091206.

[80] J. C. Vidal, E. Garcia-Ruiz, and J. R. Castillo, "Recent Advances in Electropolymerized Conducting Polymers in Amperometric Biosensors,"

Microchimica Acta 2003 143:2, vol. 143, no. 2, pp. 93–111, Dec. 2003, doi: 10.1007/S00604-003-0067-4.

[81] M. Chahma and C. Carruthers, "Electrochemical detection of oligonucleotides using polypyrroles," *Sensors and Actuators Reports*, vol. 3, p. 100039, Nov. 2021, doi: 10.1016/J.SNR.2021.100039.

[82] P. Yáñez-Sedeño, S. Campuzano, and J. M. Pingarrón, "Integrated Affinity Biosensing Platforms on Screen-Printed Electrodes Electrografted with Diazonium Salts," *Sensors 2018, Vol. 18, Page 675*, vol. 18, no. 2, p. 675, Feb. 2018, doi: 10.3390/S18020675.

[83] A. Sanati *et al.*, "A review on recent advancements in electrochemical biosensing using carbonaceous nanomaterials," Dec. 01, 2019, *Springer-Verlag Wien*. doi: 10.1007/s00604-019-3854-2.

[84] W. Hong, B. C. Wyatt, S. K. Nemani, and B. Anasori, "Double transition-metal MXenes: Atomistic design of two-dimensional carbides and nitrides," *MRS Bull*, vol. 45, no. 10, pp. 850–861, Oct. 2020, doi: 10.1557/mrs.2020.251.

[85] C. B. Jacobs, M. J. Peairs, and B. J. Venton, "Review: Carbon nanotube based electrochemical sensors for biomolecules," *Anal Chim Acta*, vol. 662, no. 2, pp. 105–127, Mar. 2010, doi: 10.1016/j.aca.2010.01.009.

[86] S. Alim, J. Vejayan, M. M. Yusoff, and A. K. M. Kafi, "Recent uses of carbon nanotubes & gold nanoparticles in electrochemistry with application in biosensing: A review," *Biosens Bioelectron*, vol. 121, pp. 125–136, Dec. 2018, doi: 10.1016/J.BIOS.2018.08.051.

[87] M. Pourmadadi, F. Yazdian, S. Hojjati, and K. Khosravi-Darani, "Detection of Microorganisms Using Graphene-Based Nanobiosensors," Oct. 01, 2021, *University of Zagreb*. doi: 10.17113/ftb.59.04.21.7223.

[88] E. B. Bahadir and M. K. Sezgintürk, "Applications of graphene in electrochemical sensing and biosensing," *TrAC Trends in Analytical Chemistry*, vol. 76, pp. 1–14, Feb. 2016, doi: 10.1016/J.TRAC.2015.07.008.

[89] J. D. Gouveia, G. Novell-Leruth, F. Viñes, F. Illas, and J. R. B. Gomes, "The Ti2CO2 MXene as a nucleobase 2D sensor: A first-principles study," *Appl Surf Sci*, vol. 544, p. 148946, Apr. 2021, doi: 10.1016/J.APSUSC.2021.148946.

[90] M. Mathew and C. S. Rout, "Electrochemical biosensors based on Ti3C2Tx MXene: future perspectives for on-site analysis," *Curr Opin Electrochem*, vol. 30, p. 100782, Dec. 2021, doi: 10.1016/J.COELEC.2021.100782.

[91] M. Khan *et al.*, "Unveiling the future: Breakthroughs and innovations in MXene-based electrochemical sensors," Mar. 01, 2025, *Elsevier B.V.* doi: 10.1016/j.cej.2025.160392.

[92] I. H. Cho, D. H. Kim, and S. Park, "Electrochemical biosensors: perspective on functional nanomaterials for on-site analysis," *Biomaterials Research 2020 24:1*, vol. 24, no. 1, pp. 1–12, Feb. 2020, doi: 10.1186/S40824-019-0181-Y.

[93] Z. Hua, T. Yu, D. Liu, and Y. Xianyu, "Recent advances in gold nanoparticles-based biosensors for food safety detection," *Biosens Bioelectron*, vol. 179, p. 113076, Feb. 2021, doi: 10.1016/j.bios.2021.113076.

[94] K. Malecka *et al.*, "Silver or gold? A comparison of nanoparticle modified electrochemical genosensors based on cobalt porphyrin-DNA," *Bioelectrochemistry*, vol. 138, p. 107723, Apr. 2021, doi: 10.1016/J.BIOELECHEM.2020.107723.

[95] H. Peng, L. Zhang, C. Soeller, and J. Travas-Sejdic, "Conducting polymers for electrochemical DNA sensing," *Biomaterials*, vol. 30, no. 11, pp. 2132–2148, Apr. 2009, doi: 10.1016/J.BIOMATERIALS.2008.12.065.

[96] M. Ates and A. S. Sarac, "Conducting polymer coated carbon surfaces and biosensor applications," Dec. 01, 2009, *Elsevier*. doi: 10.1016/j.porgcoat.2009.08.014.

[97] N. Y. Jayanath, L. T. Nguyen, T. T. Vu, and L. D. Tran, "Development of a portable electrochemical loop mediated isothermal amplification (LAMP) device for detection of hepatitis B virus," *RSC Adv*, vol. 8, no. 61, pp. 34954–34959, 2018, doi: 10.1039/c8ra07235c.

[98] A. Rivas-Macho *et al.*, "Development of an Electrochemical Sensor for SARS-CoV-2 Detection Based on Loop-Mediated Isothermal Amplification," *Biosensors (Basel)*, vol. 13, no. 10, Oct. 2023, doi: 10.3390/bios13100924.

[99] P. Saharan, P. Khatri, S. Dingolia, J. S. Duhan, and S. K. Gahlawat, "Rapid Detection of Viruses Using Loop-Mediated Isothermal Amplification (LAMP): A Review," *Biotechnology: Prospects and Applications*, vol. 9788132216834, pp. 287–306, Nov. 2013, doi: 10.1007/978-81-322-1683-4_21.

[100] M. Khater, A. de la Escosura-Muñiz, L. Altet, and A. Merkoçi, "In Situ Plant Virus Nucleic Acid Isothermal Amplification Detection on Gold Nanoparticle-Modified Electrodes," *Anal Chem*, vol. 91, no. 7, pp. 4790–4796, Apr. 2019, doi: 10.1021/acs.analchem.9b00340.

[101] S. Ciftci *et al.*, "The sweet detection of rolling circle amplification: Glucose-based electrochemical genosensor for the detection of viral nucleic acid," *Biosens Bioelectron*, vol. 151, p. 112002, Mar. 2020, doi: 10.1016/J.BIOS.2019.112002.

[102] D. Bizzotto, I. J. Burgess, T. Doneux, T. Sagara, and H. Z. Yu, "Beyond Simple Cartoons: Challenges in Characterizing Electrochemical Biosensor Interfaces," *ACS Sens*, vol. 3, no. 1, pp. 5–12, Jan. 2018, doi: 10.1021/acssensors.7b00840.

[103] T. G. Drummond, M. G. Hill, and J. K. Barton, "Electrochemical DNA sensors," Oct. 01, 2003. doi: 10.1038/nbt873.

[104] D. Futra, L. L. Tan, S. Y. Lee, B. Lertanantawong, and L. Y. Heng, "An Ultrasensitive Voltammetric Genosensor for the Detection of Bacteria Vibrio cholerae in Vegetable and Environmental Water Samples," *Biosensors (Basel)*, vol. 13, no. 6, Jun. 2023, doi: 10.3390/bios13060616.

[105] A. Lobato *et al.*, "Label-free and sensitive detection of Citrus Bark Cracking Viroid in hop using Ti3C2Tx MXene-modified genosensor," *Sens Actuators B Chem*, vol. 423, p. 136762, Jan. 2025, doi: 10.1016/j.snb.2024.136762.

[106] D. Voccia *et al.*, "Direct determination of small RNAs using a biotinylated polythiophene impedimetric genosensor," *Biosens Bioelectron*, vol. 87, pp. 1012–1019, Jan. 2017, doi: 10.1016/J.BIOS.2016.09.058.

[107] M. Ortiz, M. Torréns, N. Canela, A. Fragoso, and C. K. O'Sullivan, "Supramolecular confinement of polymeric electron transfer mediator on gold surface for picomolar

detection of DNA," *Soft Matter*, vol. 7, no. 22, pp. 10925–10930, Nov. 2011, doi: 10.1039/c1sm06300f.

[108] H. Pei *et al.*, "A DNA Nanostructure-based Biomolecular Probe Carrier Platform for Electrochemical Biosensing," *Advanced Materials*, vol. 22, no. 42, pp. 4754–4758, Nov. 2010, doi: 10.1002/ADMA.201002767.

[109] P. Sharma *et al.*, "Next-Generation Point-of-Care Diagnostics: Silver Nanoparticle-Enhanced 3D-Printed Multiplex Electrochemical Biosensor for Detecting Dengue and Chikungunya Viruses," *ACS Appl Bio Mater*, Feb. 2025, doi: 10.1021/acsabm.4c01530.

Bibliography

Publications Related to the Dissertation

Journal Articles

A. Lobato, I. Konjević, S. Radišek, J. Jakše, H. Volk, M. Hermanová, M. Fojta, J. Paštika, Z. Sofer, R. Gusmão, S. B. Hočevar, N. Tasić, "Label-free and sensitive detection of *Citrus Bark Cracking Viroid* in hop using $Ti_3C_2T_x$ MXene-modified genosensor," *Sensors and Actuators B: Chemical*, vol. 423, pp. 136762, 2025. doi: 10.1016/j.snb.2024.136762

N. Tasić, I. Konjević, A. Lobato, D. Metarapi, M. Finšgar, F.M. Oliveira, Z. Sofer, R. Gusmão, X. Zhang, S.B. Hočevar, "Study of V_2CT_x-MXene Based Immunosensor for Sensitive Label-Free Impedimetric Detection of SARS-CoV-2 Spike Protein," *ACS Applied Materials & Interfaces*, vol. 16, no. 23, pp. 30196, 2024. doi: 10.1021/acsami.4c04567

A. Lobato, M. Šubic, T. Romih, L. Žibret, D. Metarapi, M. Benčina, R. Jerala, K. Vidović, S.B. Hočevar, N. Tasić, "Development of a simple gelatin-based sensing platform for the sensitive label-free impedimetric detection of SARS-CoV-2," *Electrochimica Acta*, vol. 463, pp. 142823, 2023. doi: 10.1016/j.electacta.2023.142823

Conference Papers

A. Lobato, I. Konjević, S.B. Hočevar, N. Tasić, "Affinity-based Strategies for Electrochemical Detection of Viruses and Viroids," in *YISAC 2025: 30th Young Investigators' Seminar on Analytical Chemistry: book of abstracts*, Ljubljana, Slovenia, 2025.

A. Lobato, S.B. Hočevar, N. Tasić, "MXene-Modified Impedimetric Genosensor for Sensitive Detection of Hop Pathogen," in *17th Jožef Stefan International Postgraduate School Students' Conference: book of abstracts*, Kamnik, Slovenia, 2025.

A. Lobato, S. Radišek, J. Jakše, H. Volk, Z. Sofer, R. Gusmão, S.B. Hočevar, N. Tasić, "Development of a $Ti_3C_2T_x$ MXene-modified genosensor for the electrochemical detection of *Citrus bark cracking viroid*," in *35th Anniversary World Congress on Biosensors*, Lisbon, Portugal, 2025.

A. Lobato, H. Volk, J. Jakše, S. Radišek, S.B. Hočevar, N. Tasić, "Development of a label-free electrochemical genosensor for the detection of *Citrus bark cracking viroid* in hop extract," in *YISAC 2024: 29th Young Investigators' Seminar on Analytical Chemistry: book of abstracts*, Split, Croatia, 2024.

A. Lobato, M. Šubic, I. Konjević, T. Romih, L. Žibret, R. Jerala, M. Benčina, S.B. Hočevar, N. Tasić, "Comparison of gelatin- and polyaniline-based sensors for impedimetric detection of SARS-CoV-2 infection on screen-printed carbon electrodes," in *YISAC 2023: 28th Young Investigators' Seminar on Analytical Chemistry: book of abstracts*, Belgrade, Serbia, 2023.

A. Lobato, I. Konjević, H. Volk, J. Jakše, S. Radišek, S.B. Hočevar, N. Tasić, "Development of an electrochemical genosensor for the detection of hop disease," in *15th Jožef Stefan International Postgraduate School Students' Conference: book of abstracts*, Kamnik, Slovenia, 2023

A. Lobato, M. Šubic, T. Romih, L. Žibret, R. Jerala, M. Benčina, S.B. Hočevar, N. Tasić, "Development of a gelatin-based sensor for the impedimetric detection of SARS-CoV-2 on screen-printed carbon electrodes," in *Program of the 34th Topical Meeting of the International Society of Electrochemistry: Electrochemistry: Reaching out to society*, Mar del Plata, Argentina, 2023

A. Lobato, M. Šubic, T. Romih, L. Žibret, S.B. Hočevar, N. Tasić, "Development of impedimetric SARS-CoV-2 sensor on screen-printed carbon electrodes modified with gelatin," in *Mátrafüred 2022: International Conference on Chemical Sensors*, Visegrád, Hungary, 2022.

A. Lobato, S.B. Hočevar, N. Tasić, "Strategies for electrochemical genosensing of viruses and viroids," in *14th Jožef Stefan International Postgraduate School Students' Conference: book of abstracts*, Kamnik, Slovenia: Jožef Stefan International Postgraduate School, 2022.

Other Publications

R.A.S. Couto, A. Lobato, M.B. Quinaz, L.M. Gonçalves, "Electropolymerized molecularly imprinted polymers in sensing applications," in *Encyclopedia of Sensors and Biosensors*, vol. 2, pp. 401, 2023. Doi: 10.1016/B978-0-12-822548-6.00018-2

H.G.M. Sposito, A. Lobato, N. Tasić, A.O. Maldaner, T.R.L.C. Paixão, L.M. Gonçalves, "Swift electrochemical sensing of diltiazem employing highly-selective molecularly-imprinted 3-amino-4-hydroxybenzoic acid," *Journal of Electroanalytical Chemistry*, vol. 911, pp. 116207, 2022. doi: 10.1016/j.jelechem.2022.116207

B. Bossard, R.A. Grothe, A.B. Martins, A. Lobato, N. Tasić, T.R.L.C. Paixão, L.M. Gonçalves, "Nanographene laser-pyrolyzed paper electrodes for the impedimetric detection of D-glucose via a molecularly imprinted polymer," *Monatshefte für Chemie*, vol. 153, pp. 1129, 2022. doi: 10.1007/s00706-022-02997-7

K.C.A. Francisco, A. Lobato, N. Tasić, A.A. Cardoso, L.M. Gonçalves, "Determination of 5-hydroxymethylfurfural using an electropolymerized molecularly imprinted polymer in combination with Salle," *Talanta*, vol. 250, pp. 123723, 2022. doi: 10.1016/j.talanta.2022.123723

R. A. Grothe, A. Lobato, B. Mounssef, N. Tasić, A.A.C. Braga, A.O. Maldaner, L. Aldous, T.R.L.C. Paixão, L.M. Gonçalves, "Electroanalytical profiling of cocaine samples by means of an electropolymerized molecularly imprinted polymer using benzocaine as the template molecule," *Analyst*, vol. 146, pp. 1747, 2021. doi: 10.1039/D0AN02274H

A. Lobato, V.C. Fernandes, J.G. Pacheco, C. Delerue-Matos, L.M. Gonçalves, "Organochlorine pesticide analysis in milk by gas-diffusion microextraction with gas chromatography-electron capture detection and confirmation by mass spectrometry," *Journal of Chromatography A*, vol. 1636, pp. 461797, 2021. doi: 10.1016/j.chroma.2020.461797

T.A. Donegatti, A. Lobato, E.A.R. Duek, L.M. Gonçalves, E.A. Pereira, "Derivatization-free determination of aminoglycosides by CZE–UV in pharmaceutical formulations," *Electrophoresis*, vol. 41, no.18-19, pp. 1576, 2020. doi: 10.1002/elps.202000160.

A. Lobato, E.A. Pereira, L.M. Gonçalves, "Combining capillary electromigration with molecular imprinting techniques towards an optimal separation and determination," *Talanta*, vol. 221, pp. 121546, 2021. doi: 10.1016/j.talanta.2020.121546

A. Lobato, F.R. Cavalcanti, "Padrões de restrição de DNA para detecção molecular de Lasiodiplodia theobromae em videira e estudos filogenéticos em sequências concatenadas," in *Boletim de pesquisa e desenvolvimento*, vol. 19, pp. 6, 2021. https://www.embrapa.br/en/busca-de-publicacoes/-/publicacao/1130397/padroes-de-restricao-de-dna-para-deteccao-molecular-de-lasiodiplodia-theobromae-em-videira-e-estudos-filogeneticos-em-sequencias-concatenadas

I. Benachio, A. Lobato, L.M. Gonçalves, "Employing molecularly imprinted polymers in the development of electroanalytical methodologies for antibiotic determination," *Journal of Molecular Recognition*, vol. 34, no. 3, pp. e2878, 2020. doi: 10.1002/jmr.2878

A.B. Martins, A. Lobato, N. Tasić, F.J. Perez-Sanz, P. Vidinha, T.R.L.C. Paixão, L.M. Gonçalves, "Laser-pyrolyzed electrochemical paper-based analytical sensor for sulphite analysis," *Electrochemistry Communications*, vol. 107, pp. 106541, 2019. doi: 10.1016/j.elecom.2019.106541.

T.A. Donegatti, A. Lobato, L.M. Gonçalves, E.A. Pereira, "Cyclohexane-1,3-dione as a derivatizing agent for the analysis of aldehydes by micelar electrokinetic chromatography with diode array detection," *Electrophoresis*, vol. 40, no. 22, pp. 2929, 2019. doi: 10.1002/elps.201900171

Biography



Doctoral candidate Alnilan Cristina Barros Lobato was born on August 14, 1997, in Belém, Pará, Brazil. She received her Bachelor's degree in Bioprocess Engineering and Biotechnology at the Rio Grande do Sul State University (UERGS) in Bento Gonçalves, Rio Grande do Sul, Brazil. During her undergraduate studies, she completed a one-year internship at the Brazilian Agricultural Research Corporation (Embrapa) in the Grape and Wine Research Unit. During this time, she applied molecular biology methods to detect pathogens that cause grapevine trunk diseases and also studied grapevine's enzyme profiles and defense mechanisms. In December 2018, she successfully defended her Bachelor's thesis entitled "Affinity studies for phenolic substrates in grapevine peroxidases and polyphenol oxidases". In 2019, she enrolled in the Master's program in Chemistry at the Institute of Chemistry of the University of São Paulo (USP). In the same year, she participated in a two-month exchange at the Polytechnic of Porto – School of Engineering (ISEP), where she worked with gas diffusion microextraction to detect pesticides in milk. In June 2021, she successfully defended her Master's thesis in Analytical Chemistry entitled "A new synergetic path for gas diffusion microextraction (GDME) making use of molecularly imprinted polymers (MIPs)".

In September 2021, she enrolled in the doctoral program in Sensor Technologies at the Jožef Stefan International Postgraduate School in Ljubljana, Slovenia. Since November 2021, she has been employed as a Young Researcher at the National Institute of Chemistry in Ljubljana, Slovenia, under the supervision and scientific guidance of Dr. Nikola Tasić.

Her main research interests include the development of electrochemical sensors and biosensors for detecting important molecules for the environment and public health. She has published twelve original scientific articles, two review articles, and one book chapter, all in peer-reviewed international journals. Furthermore, she has participated in ten scientific conferences as a participant and in five as an organizer.